Astronomy Letters, Vol. 31, No. 9, 2005, pp. 575–578. Translated from Pis'ma v Astronomicheskiĭ Zhurnal, Vol. 31, No. 9, 2005, pp. 643–647.

On the Very-High-Energy Gamma-Ray Flux from the Galaxy Mrk 421 in 2004

V. V. Fidelis*, A. A. Stepanian, V. S. Eliseev, N. A. Zhogolev, E. M. Nekhai, Yu. I. Neshpor, and Z. N. Skiruta

Crimean Astrophysical Observatory, Ukrainian Academy of Sciences, p/o Nauchnyĭ, Crimea, 98409 Ukraine

Received December 22, 2004

Abstract—The galaxy Mrk 421 was observed with the GT-48 Cherenkov telescope in 2004. The observations revealed a very-high-energy gamma-ray flux at a confidence level of 4.8 σ. Comparison with the constant gamma-ray flux from the Crab Nebula yielded an estimate of the total flux from Mrk 421, 1.7 ± 0.7 Crab ($E \geq 1$ TeV). © *2005 Pleiades Publishing, Inc.*

Key words: *gamma-ray sources, active galactic nuclei, Mrk 421.*

INTRODUCTION

Among the various objects in the Universe that emit very-high-energy (VHE, $E > 10^{11}$ eV) gamma rays, active galactic nuclei (AGNs) are of considerable interest. The VHE gamma-ray emission from these objects presumably originates from the relativistic jets ejected from their central regions and directed toward the observer. VHE gamma rays can be detected on the Earth's surface by the Cherenkov radiation of extensive air showers (EASs) generated by them in the atmosphere, which consist of charged particles (electrons and positrons). The Cherenkov radiation of an EAS propagates in a narrow cone with an angular aperture of $\sim 1^\circ$ and with the axis coincident with the arrival direction of the primary gamma-ray photon; it covers a circle on the order of several hundred meters in diameter on the Earth's surface, which makes it possible to detect low VHE gamma-ray fluxes.

The possibility of studying AGNs in the VHE gamma-ray range using ground-based detectors opens new prospects for understanding the physics of radiation processes in these objects. Data on the VHE gamma-ray fluxes from these extragalactic objects and their variations can be used to construct new models of radiation processes in AGNs and to improve existing models (Katarzynski *et al.* 2003).

VHE gamma-ray emission from the galaxy Mrk 421 ($z = 0.031$) was detected for the first time at Whipple Observatory at a level of 0.3 Crab (units of the flux from the Crab Nebula) in the energy range above 0.5 TeV at a confidence level of 6σ (Punch *et al.* 1992). Interest in the observations of this galaxy was aroused by the variability of its TeV emission on various time scales with the flux exceeding its quiescent level by dozens of times (Gaidos *et al.* 1996; Kerrick *et al.* 1995) and by the correlation with the X-ray emission (Macomb *et al.* 1995). Thus, for example, the almost tenfold increase in the brightness of Mrk 421 observed for a day in 1994 at TeV energies was accompanied by a rise in its X-ray flux (Inoue and Takahara 1996).

Variability on a yearly scale is also characteristic of the galaxy Mrk 421. Thus, long-term observations of this object with the CAT Cherenkov telescope in the French Pyrenees at an altitude of 1650 m showed that the total gamma-ray flux with an energy above 0.25 TeV changed from the minimum mean value recorded in 1996–1997 ($\sim$0.18 Crab) to the maximum value ($\sim$0.64 Crab) recorded in 1999–2000 (Piron *et al.* 2001).

In contrast to other AGNs observed by the EGRET detector onboard the *Compton Gamma Ray Observatory*, the gamma-ray ($E > 100$ MeV) brightness of Mrk 421 is not dominant (Thompson *et al.* 1995), and its optical luminosity, $\sim 10^{44}$ erg s^{-1}, is also relatively low compared to other gamma-ray sources (Inoue and Takahara 1996).

The galaxy Mrk 421 has been observed at the Crimean Astrophysical Observatory (CrAO) since 2002. From December 2 through December 6, 2002, we detected a VHE gamma-ray burst from this object with a duration of no longer than a day, which coincided with the X-ray burst in the 3–25 keV energy range. From April 4 through May 5, 2003, we detected a flux from Mrk 421 at a confidence level of 4.2σ (Fidelis *et al.* 2004).

*E-mail: fedelis@crao.crimea.ua

1063-7737/05/3109-0575$26.00

Main parameters of the GT-48 telescope

Parameter	Value
Field of view of one cell	0.°4
Field of view of each camera	2.°6
Total area	
of compound mirrors	36 m^2
Section tracking accuracy	$\pm$0.°05
Threshold energy	1 TeV

In 2004, the CrAO observations of the galaxy Mrk 421 continued; the results are presented below.

THE CHERENKOV TELESCOPE AND OBSERVATIONS

The galaxy Mrk 421 (the coordinates for 2004 are $\alpha = 11^h04^m37^s$ and $\delta = 38°11'38''$) was observed at CrAO with the GT-48 Cherenkov telescope (Vladimirsky *et al.* 1994).

The telescope consists of two identical mountings (sections), northern (N) and southern (S), spaced 20 m apart. Each section of the telescope is equipped with four cameras (light detectors) operating in the visible range and consisting of 37 photomultipliers, which together with their conical optical fibers form 37 cells (channels) (Andreeva *et al.* 2000). The main parameters of the telescope are listed in the table.

The observations were performed in the source tracking mode (ON mode) with a duration of 35 min followed by a background measurement (OFF mode) of the same duration with a shift in right ascension α by 40 min. The observations in these modes were performed at the same zenith angles. A total of 13 pair observing sessions were conducted from April 15 through May 21, 2004. The observing sessions under bad weather conditions were excluded from the data processing. After excluding two pair sessions due to a low count rate and its great nonuniformity on the source or the background, 11 pair observing sessions from April 15 through April 22, 2004, were included in the data processing. The total source exposure time was 385 min, with the time of background observation being the same.

After the primary data processing, which was reduced to determining the parameters of flashes, eliminating the events with poor tracking, introducing the calibration coefficients, eliminating the flashes with the maximum amplitude in the outer ring of the light detectors, 5234 and 4988 Cherenkov flashes in the source and background observations, respectively, were left for the subsequent analysis.

ANALYSIS OF THE OBSERVATIONAL DATA

EASs produced by VHE gamma rays can be separated from background EASs produced by cosmic rays (mainly protons) by selecting the images of Cherenkov flashes by their shape, sizes, and orientation with respect to the position of the source in the field of view of the multielement camera. The flashes from EASs generated by VHE gamma rays have smaller angular sizes and relatively compact images elongated toward the source in the field of view of the camera. The flashes from proton showers have an isotropic distribution in the field of view of the camera with respect to the position of the source, much larger angular sizes, and more fragmented images.

The flashes were selected by position-independent parameters characterizing the size, amplitude, and shape of the flash projection and by position-dependent parameters related to the flash image orientation with respect to the position of the source in the field of view of the camera (Hillas 1985). The boundary values of the selection parameters were chosen to obtain an optimal signal-to-noise ratio $Q = (Ns - Nb)/\sqrt{Ns + Nb}$, where Ns and Nb are the numbers of gamma-ray-like flashes in the source and background observations, respectively. The difference $(Ns - Nb) = N_\gamma$ is interpreted as the number of gamma-ray photons, and $\sqrt{Ns + Nb}$ is the statistical error of this number. The events with selection parameters outside the specified range were excluded from our analysis.

Since the parameters of low-energy flashes are strongly distorted, we imposed a limit on the total flash energy expressed in terms of the amplitude of the detected signal. The flashes with a total amplitude below 125 quantization steps (which is equivalent to $\approx$90 photoelectrons) for both sections of the telescope were excluded from our analysis. We selected the flashes by the shapes of their images using the IPR parameter, which characterizes the degree of image fragmentation. We assigned zero values to the IPR parameter for the most compact flashes (no flash image fragmentation) and 1 to 7 for more fragmented flashes. For the given selection, this parameter was IPR = 0 for both sections of the telescope.

The limits on the position-independent parameters characterizing the flash sizes were set for the two sections of the telescope as follows: $0.°22 < \mathrm{A(N)} < 0.°32$ and $0.°18 < \mathrm{A(S)} < 0.°33$ for the effective length; $0.°05 < \mathrm{B(N)} < 0.°18$ and $0.°05 < \mathrm{B(S)} < 0.°19$ for the effective width of their images.

The selection by the position-dependent parameters was specified as follows: $0.°2 < \mathrm{DIST(N)} < 0.°95$ and $0.°25 < \mathrm{DIST(S)} < 0.°95$, $\mathrm{ALPHA(N, S)} < 31°$. Here, DIST is the angular distance between the source and the centroid of the flash image, ALPHA

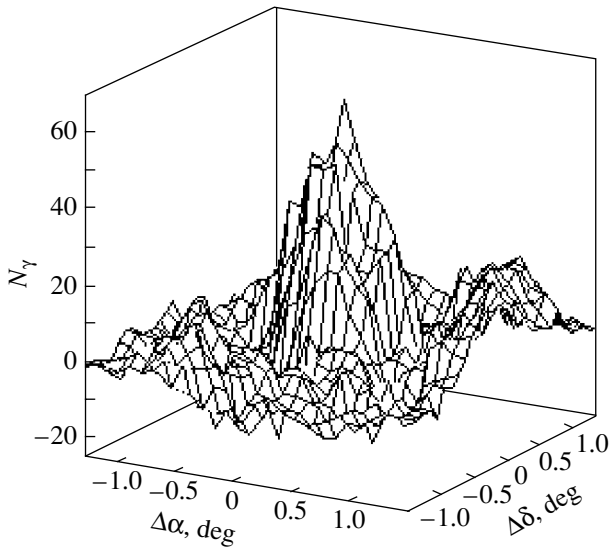

Fig. 1. Stereo image of the distribution of VHE gamma-ray arrival directions: $\Delta\alpha$ and $\Delta\delta$ are the deviations from the source position in right ascension and declination (in degrees), respectively; the center of the map coincides with the position of Mrk 421; N_γ is the number of gamma-ray photons.

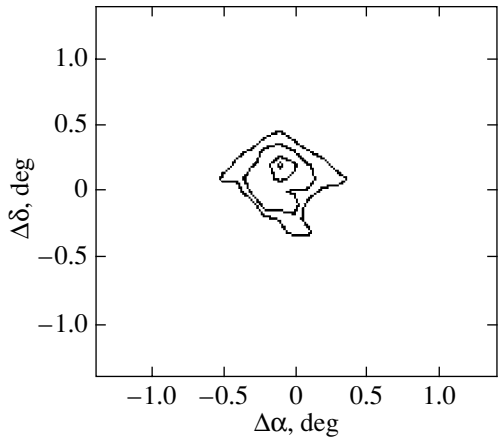

Fig. 2. Isophotes of the distribution of gamma-ray arrival directions. The notation is the same as that in Fig. 1. The outer isophote corresponds to 32 events; the isophote step is 9 events.

is the angle between the direction of the source from the centroid of the flash image and the major axis of the flash image.

After applying the above selection parameters with the specified boundary values to the preprocessed observational data set, $Ns = 118$ and $Nb = 55$ gamma-ray-like events remained in the source and background observations, respectively. Accordingly, the number of detected gamma-ray photons was $N_\gamma = 63$ at a confidence level of $Q = 4.8\sigma$. The resulting gamma-ray photon count rate was 0.164 ± 0.034 photons min $^{-1}$ (the statistical error).

A three-dimensional histogram of selected gamma-ray flashes in the field of view of the light detector (see Fig. 1) was constructed by using the trial source method (Akerlof *et al.* 1991; Neshpor *et al.* 1994). During the observations, the camera was directed toward the galaxy Mrk 421. The maximum of the projected distribution has deviations from the source position ($\Delta\alpha = -0.^\circ1$, $\Delta\delta = 0.^\circ2$) (see Fig. 2). We also see from Fig. 2 that the gamma-ray source virtually coincides in position with the galaxy Mrk 421, within the error limits of the trial source method ($\approx 0.^\circ1$).

To estimate the flux from the observed object, we processed the observations of the Crab Nebula in 2002–2004 with a source exposure time of 15 h. We used the same selection parameters as those for the observed gamma-ray source. The resulting gamma-ray photon count rate, corresponding to a unit of the flux from the Crab Nebula (Crab, $E \geq 1$ TeV), is 0.099 ± 0.019 photons min^{-1} (the deviations from the source position were chosen to be the same as those for Mrk 421). Accordingly, the flux from the galaxy Mrk 421, in units of the flux from the Crab Nebula, was estimated to be 1.66 ± 0.67 Crab. The relative error of the estimated flux ($\delta \approx 0.4$) was estimated as the sum of the relative errors in the count rates for the two objects $\delta = \delta_{\text{Crab}} + \delta_{\text{Mrk 421}}$ (Rumshinskiĭ 1971).

Figure 3 shows the time dependence of the mean fluxes from Mrk 421 in the observational periods of different years as measured on the GT-48 telescope and on other facilities with similar gamma-ray detection thresholds. The Whipple and HEGRA measurements were carried out at the threshold energy $E = 0.5$ TeV. The threshold energy of the HEGRA CT2 telescope is 1 TeV.

Based on our estimate of the detected VHE flux, we can assert that the galaxy Mrk 421 was in an active state in the observational period of 2004. This is also suggested by the enhanced X-ray activity of Mrk 421. Thus, for example, the mean flux from the object in the 2–10 keV energy range in the observational period was ≈61 mCrab (quick-look results provided by the ASM/RXTE team). On the last day of the object's gamma-ray observations, April 22 (MJD52117.5), the ASM detector onboard the orbiting X-ray observatory *Rossi X-ray Timing Explorer Project* (RXTE) recorded a burst from it with an amplitude of ≈103 mCrab and a confidence level of $\approx 27\sigma$. It should be noted that Mrk 421 is considered weak in the 2–10 keV range at a flux of 3 mCrab and strong at 50 mCrab (quick-look results provided by the ASM/RXTE team).

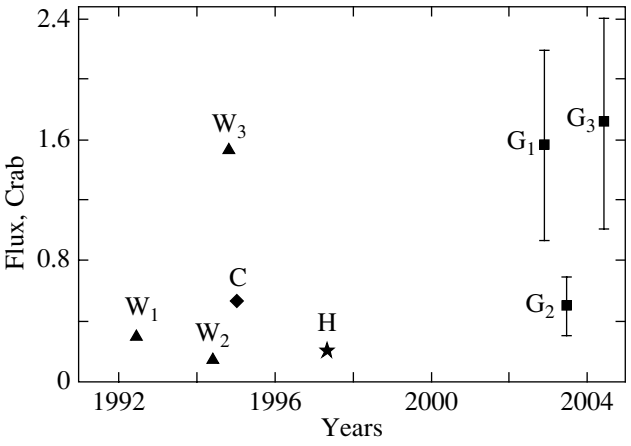

Fig. 3. Mean VHE gamma-ray fluxes from the galaxy Mrk 421 recorded in the observational periods of different years: W, Cherenkov telescope of the Whipple Observatory; H, HEGRA system of Cherenkov telescopes; C, ST2 Cherenkov telescope of the HEGRA system; G, GT-48 Cherenkov telescope. The data were taken from the following papers: W_1 (Punch *et al.* 1992); W_2 and W_3 (Kerrick *et al.* 1995); C (Petry 1997); H (Hermann *et al.* 1997); G_1 (Fidelis 2005); G_2 (Fidelis *et al.* 2004); G_3 (this paper).

CONCLUSIONS

We can assert with a confidence of 4.8σ that the VHE gamma-ray flux we detected arrives from the galaxy Mrk 421. By comparing the flux from this object with the VHE gamma-ray flux from the Crab Nebula, we were able to estimate the flux from the observed object as (1.7 ± 0.7) Crab ($E \geq 1$ TeV).

The mean flux from Mrk 421 in the observational period of 2004 was comparable to its flux in 2002, when X-ray and VHE gamma-ray outburst activity was observed in the object. It is also close to the flux from the object during the outburst of May 14–15, 1994, when it was by a factor of 10 higher than the mean value in the previous observational period from December 23, 1993, through May 10, 1994, detected with the Cherenkov telescope at Whipple Observatory (Kerrick *et al.* 1995).

REFERENCES

1. C. W. Akerlof, M. F. Cawley, M. Chantell, *et al.*, Astrophys. J. **377**, L97 (1991).
2. N. A. Andreeva, Yu. L. Zyskin, O. R. Kalekin, *et al.*, Pis'ma Astron. Zh. **26**, 243 (2000) [Astron. Lett. **26**, 199 (2000)].
3. V. V. Fidelis, Astron. Zh. **82**, 1 (2005) [Astron. Rep. **49**, 1 (2005)].
4. V. V. Fidelis, V. S. Eliseev, N. A. Zhogolev, *et al.*, in *Proseedings of the 28th All-Russia Conference on Cosmic Rays, CD-ROM* (MIFI, Moscow, 2004), p. 105.
5. J. A. Gaidos, C. W. Akerlof, S. Biller, *et al.*, Nature **383**, 319 (1996).
6. G. Hermann (for the HEGRA-Collab.), in *Proceedings of Kruger National Park Workshop on TeV Gamma Ray Astrophysics, Towards a Major Atmospheric Cerenkov Detector—V. Space Research Unit*, Ed. by O. C. de Jager (WESTPRINT—Potchefstroom, South Africa, 1997), p. 208.
7. A. M. Hillas, in *Proceedings of the 19th International Cosmic Ray Conference* **3**, 445 (1985).
8. S. Inoue and F. Takahara, Astrophys. J. **463**, 555 (1996).
9. K. Katarzynski, H. Sol, and A. Kus, Astron. Astrophys. **410**, 101 (2003).
10. A. D. Kerrick, C. W. Akerlof, S. D. Biller, *et al.*, Astrophys. J. Lett. **438**, L59 (1995).
11. D. J. Macomb, C. W. Akerlof, H. D. Aller, *et al.*, Astrophys. J. **449**, L99 (1995).
12. Yu. I. Neshpor, A. P. Kornienko, A. A. Stepanian, and Yu. L. Zyskin, Exp. Astron. **5**, 405 (1994).
13. D. Petry, in *Proceedings of Kruger National Park Workshop on TeV Gamma Ray Astrophysics, Towards a Major Atmospheric Cerenkov Detector—V. Space Research Unit*, Ed. by O. C. de Jager (WESTPRINT—Potchefstroom, South Africa, 1997), p. 2.
14. F. Piron, D. Djannati–Ataï, M. Punch, *et al.*, Astron. Astrophys. **374**, 895 (2001).
15. M. Punch, C. W. Akerlof, M. F. Cawley, *et al.*, Nature **358**, 477 (1992).
16. L. Z. Rumshinskiĭ, *Mathematical Processing of Experimental Results* (Nauka, Moscow, 1971), p. 164 [in Russian].
17. D. J. Thompson, D. L. Bertsch, B. L. Dingus, *et al.*, Astrophys. J., Suppl. Ser. **101**, 259 (1995).
18. B. M. Vladimirsky, Yu. L. Zyskin, A. P. Kornienko, *et al.*, Izv. Krym. Astrofiz. Obs. **91**, 74 (1994).

Translated by G. Rudnitskiĭ

Astronomy Letters, Vol. 31, No. 9, 2005, pp. 579–585. Translated from Pis'ma v Astronomicheskiĭ Zhurnal, Vol. 31, No. 9, 2005, pp. 648–655.

Statistics of Neutron Stars at the Stage of a Supersonic Propeller

V. S. Beskin[1]* and S. A. Eliseeva[2]

[1] *Lebedev Physical Institute, Russian Academy of Sciences, Leninskiĭ pr. 53, Moscow, 117924 Russia*

[2] *Moscow Institute of Physics and Technology, Institutskiĭ per. 9, Dolgoprudnyĭ, Moscow oblast, 141700 Russia*

Received April 5, 2005

Abstract—We analyze the statistical distribution of neutron stars at the stage of a supersonic propeller. An important point of our analysis is allowance for the evolution of the angle of inclination of the magnetic axis to the spin axis of the neutron star for the boundary of the transition to the supersonic propeller stage. We have determined the spin period distributions of pulsars at the propeller stage for two models: the model with hindered particle escape from the stellar surface and the model with free particle escape. As a result, we have shown that consistent allowance for the evolution of the inclination angle in the region of extinct radio pulsars for the two models leads to an increase in the total number of neutron stars at the supersonic propeller stage. This increase stems from the fact that when allowing for the evolution of the inclination angle χ for neutron stars in the region of extinct radio pulsars and, hence, for the boundary of the transition to the propeller stage, this transition is possible at shorter spin periods ($P \sim 5-10$ s) than assumed in the standard model. © *2005 Pleiades Publishing, Inc.*

Key words: *neutron stars, radio pulsars.*

INTRODUCTION

Previously, we showed (Beskin and Eliseeva 2005) that the transition to the propeller stage could occur at much shorter periods than assumed in the standard model when allowance is made for the evolution of the angle of inclination of the magnetic axis to the spin axis of the neutron star. Consequently, allowance for the evolution of the inclination angle at the stage of extinct radio pulsars would affect significantly the statistics of neutron stars at the propeller stage.

As Davies *et al.* (1979) and Davies and Pringle (1981) showed, the following two so-called substages that a neutron star undergoes as its spin period decreases must be distinguished: supersonic and subsonic propellers. In both cases, the neutron star spins down due to the interaction of the stellar magnetosphere with the surrounding matter.

As a neutron star spins down, the electrodynamic processes cease to play a significant role in the pulsar's magnetosphere. When the radius at which the pressure of the ambient medium is balanced by the magnetodipole radiation pressure (the Schwarzman radius) becomes equal to the Alfvén radius, the star passes to the stage of a supersonic propeller. As the spin period increases further, the barrier produced by the rotation of the neutron star's strong magnetic field ceases to be efficient and the plasma begins to penetrate into the pulsar's magnetosphere. Thus, the pulsar passes to the stage of a subsonic propeller.

Subsequently, due to an even larger spindown, the accretion rate increases and can reach its maximum at a certain period P—the neutron star passes to the stage of a steady accretor. The evolution of a neutron star at the "supersonic propeller–subsonic propeller–stable accretor" stages was considered in more detail in the paper by Ikhsanov (2003), whose results we used here.

In this paper, we consider the stationary distribution of isolated neutron stars at the supersonic propeller stage. As previously (Beskin and Eliseeva 2005), all our calculations were performed for two basic models: the model with hindered particle escape from the neutron-star surface (Ruderman and Sutherland 1975; Beskin *et al.* 1993) and the model with free particle escape (Arons 1979; Mestel 1999). We disregard the possibility of magnetic-field evolution and assume that no neutron stars are born at the supersonic propeller stage. An important point of our study is that the boundary of the transition of a neutron star from the ejector stage to the propeller stage is presented with allowance made for the evolution of the inclination angle.

As a result, we obtained the distribution of neutron stars at the supersonic propeller stage in spin period P. We show that the number of neutron stars at this stage is larger when the evolution of the inclination angle is taken into account for the transition

*E-mail: beskin@lpi.ru

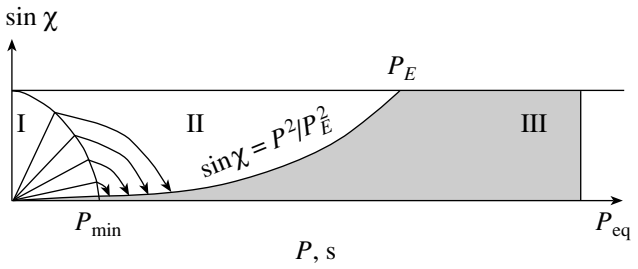

Fig. 1. Evolution of neutron stars under the assumption of hindered particle escape: I, active radio pulsars; II, extinct radio pulsars; and III, pulsars at the supersonic propeller stage.

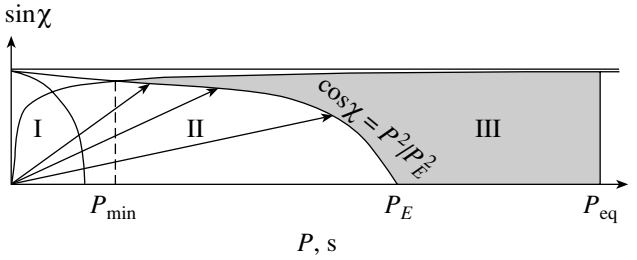

Fig. 2. Evolution of neutron stars under the assumption of free particle escape. The notation is the same as that in Fig. 1.

boundary than that in the case where the standard model is considered. We also show once again that when the evolution of the inclination angle χ is taken into account, neutron stars can pass to the propeller stage even at fairly short periods: $P \sim 5{-}10$ s.

BASIC EQUATIONS

Lipunov and Popov (1995) formulated an important assertion: for a constant magnetic field, the ejector stage at reasonable parameters is always longer than the propeller stage. Our objective in this part of the paper is to determine the number of neutron stars at the propeller stage by disregarding both the magnetic-field decay and the evolution of the angle of inclination of the magnetic axis to the spin axis of the star at this stage.

A neutron star at the propeller stage is known to spin down due to the transfer of angular momentum to the surrounding matter (Schwarzman 1970; Illarionov and Syunyaev 1975). There are many formulas that describe this spindown (see Lipunov 1987; Lipunov and Popov 1995). Nevertheless, virtually all of them can be reduced to the form (Popov and Prokhorov 2002)

$$\frac{dI\omega}{dt} = -k_t\frac{\mu^2}{R_{\rm A}^3}.$$

Here, $I \sim 2/5MR^2$ is the moment of inertia of the star, μ is the magnetic dipole moment, $k_t \approx 1$ is a dimensionless constant, and $R_{\rm A}$ is the Alfvén radius:

$$R_{\rm A} = \left(\frac{\mu^2}{\dot{M}\sqrt{2GM}}\right)^{2/7},$$

where M is the mass of the neutron star. The accretion rate can be estimated as

$$\dot{M} \simeq \pi R_\alpha^2 \rho V_\infty,$$

where V_∞ is the space velocity of the neutron star relative to the surrounding interstellar medium, ρ is the density of the interstellar medium, and R_α is the gravitational capture radius, which for spherically symmetric accretion is

$$R_\alpha = \frac{2GM}{V_\infty^2}.$$

The maximum possible accretion rate onto a isolated neutron star (for spherically symmetric accretion) was determined by Ikhsanov (2003) and can be specified by the following expression:

$$\dot{M} \le M_{\max} \simeq 2.3\times10^{11}\rho_{-24}m^2V_6^{-3}\ {\rm g\ s^{-1}},$$

where m is the mass of the star expressed in terms of solar masses, $\rho_{-24} = \rho/10^{-24}$ g cm^{-3}, and $V_6 = V_\infty/10^6$ cm s^{-1}. Given all of the factors listed above, the transfer of angular momentum to the surrounding interstellar medium is found to cause the neutron star to spin down at the rate

$$\frac{dP}{dt} = 2.5\times10^{-11}B_{12}^{2/7}P^2. \qquad (1)$$

Further, it should be noted that for the model with hindered particle escape from the pulsar's surface, the transition to the supersonic propeller stage for most neutron stars can occur only at fairly small angles χ between the magnetic axis and the spin axis (Fig. 1). Consequently, in the case of hindered particle escape, the neutron stars passing to the propeller stage are almost aligned rotators, and the subsequent evolution of the inclination angle is unimportant. As a result, it can be assumed with sufficient accuracy for the Ruderman–Sutherland model that the inclination angle does not evolve at the supersonic propeller stage.

As regards the model with free particle escape from the neutron-star surface, the characteristic period at which the transition to the propeller stage occurs is much longer than the death period. Consequently, most neutron stars will enter the region of angles close to 90° before the transition of the star to the supersonic propeller stage (see Fig. 2).

Thus, we are interested in the statistics of pulsars at the supersonic propeller stage without considering the angle of axial inclination. Accordingly, to determine the stationary distribution function of neutron stars, let us introduce their distribution $N_3(P,B)$ in period P and magnetic field B. Next, as in the case of extinct radio pulsars, we assume that the function $N_3(P,B)$ depends on the magnetic field B of the neutron star only as a parameter; i.e., we disregard the magnetic-field evolution over the lifetime of the neutron star. As a result, the kinetic equation for neutron stars at the supersonic propeller stage can be written as

$$\frac{\partial}{\partial P}\left(N_3\frac{dP}{dt}\right)=F(P,B), \qquad (2)$$

where the source function $F(P,B)$ is determined by the neutron star flux from the region of extinct radio pulsars.

Finally, we must specify the boundary periods for the supersonic propeller stage, i.e., the period at which the transition from the ejector stage to the propeller stage occurs and the period at which the accretion of matter from the interstellar medium onto the neutron star begins. As we found previously (Beskin and Eliseeva 2005), the transition from the ejector stage to the propeller stage occurs for the model with hindered particle escape from the neutron-star surface at the spin period

$$P_{\rm pr}=P_E\sin^{1/2}\chi. \qquad (3)$$

At the same time, the following expression holds for the model with free particle escape:

$$P_{\rm pr}=P_E\cos^{1/2}\chi. \qquad (4)$$

Below, the expression for the limiting period P_E has the standard form (Lipunov *et al.* 1996)

$$P_E\approx\frac{R}{c}\left(\frac{Rc^2}{GM}\right)^{1/2}\frac{v_\infty}{c}\left(\frac{B_0^2}{4\pi\rho_\infty v_\infty^2}\right)^{1/4}\times\left(\frac{c_\infty}{v_\infty}\right)^{1/2}\approx 10^2\frac{\mu_{30}^{1/2}c_7^{1/2}v_7^{1/2}}{(B_{\rm ext})_{-6}^{1/2}}\ {\rm s}.$$

Here, ρ_∞ and c_∞ are, respectively, the density and the speed of sound in the interstellar medium (c_7 and v_7 are in units of 10^7 cm s^{-1}); $B_{\rm ext}^2=8\pi\rho_\infty c_\infty^2$ is the corresponding magnetic energy density ($(B_{\rm ext})_{-6}$ is in units of 10^{-6} G); and μ_{30} is the magnetic moment of the neutron star in units of 10^{30} G cm^2. In addition, we assumed that the velocity of neutron stars v_∞ is much larger than the speed of sound in the interstellar medium.

Next, it is necessary to determine the spin period at which the star passes to the subsonic propeller stage. For this purpose, we recall that a pulsar can be at the supersonic propeller stage as long as its angular velocity is large enough, and, accordingly, the centrifugal acceleration exceeds the free-fall acceleration. Consequently, the condition under which the accretion of matter from the interstellar medium onto a isolated neutron star begins can be specified as follows:

$$\omega^2 R_{\rm A}=\frac{GM}{R_{\rm A}^2},$$

where $\omega=2\pi/P$ is the angular velocity of the neutron star.

As a result, for the boundary period corresponding to the transition of a isolated neutron star to the subsonic propeller stage, we obtain an expression that is similar to that derived by Ikhsanov (2003):

$$P_{\rm eq}\simeq 24\mu_{30}^{6/7}\dot{M}_{15}^{-3/7}m^{-5/7}\ {\rm s},$$

where $\dot{M}_{15}$ is the accretion rate in units of 10^{15} g s^{-1}, and $m=M/M_\odot$.

Substituting the parameters into the above formula, we can estimate the period at which the neutron star leaves the supersonic propeller stage:

$$P_{\rm eq}\simeq 670B_{12}^{6/7}\ {\rm s}. \qquad (5)$$

Let us now consider the spin period distribution of neutron stars passed to the supersonic propeller stage for the standard model, i.e., for the model in which the evolution of the inclination angle in the region of extinct radio pulsars is disregarded. In this case, the kinetic equation can be written as

$$\frac{d}{dP}\left(N_3\frac{dP}{dt}\right)=0.$$

It should also be recalled that $N_2(P)=N_{\rm f}P$ for the region of extinct radio pulsars in the standard model, while the derivative of the spin period at the supersonic propeller stage can be represented by Eq. (1). As a result, we obtain the following distribution of neutron stars in spin period P for the model where the evolution of the angle of inclination of the magnetic axis to the spin axis is disregarded:

$$N_3(P)=4\times10^{-5}N_{\rm f}P^{-2},\quad \text{if}\quad P>P_E,$$
$$N_3(P)=0,\quad \text{if}\quad P<P_E.$$

In this case, the total number of neutron stars at the supersonic propeller stage for the model in which the inclination angle is disregarded can be estimated as $N_3=4\times10^{-5}N_{\rm f}/P_E$.

THE MODEL WITH HINDERED PARTICLE ESCAPE FROM THE NEUTRON-STAR SURFACE

Let us consider the statistics of pulsars at the supersonic propeller stage in more detail assuming that the model with hindered particle escape from the neutron-star surface is valid. In this case, the boundary of the transition from the region of extinct radio pulsars (the ejector stage) to the supersonic propeller region is defined by Eq. (3).

Thus, the source function $F(P,B)$ in the kinetic equation (2) can be written as

$$F(P,B) = F(P,B,\chi)|_{\sin\chi=P^2P_E^{-2}},$$

where

$$F(P,B,\chi) = \dot{\chi}N_2.$$

The distribution function $N_2(P,B,\chi)$ in the latter expression refers to the region of extinct radio pulsars, and we found it previously (Beskin and Eliseeva 2005). Recall that this function for the model with hindered particle escape from the neutron-star surface can be specified as

$$N_2(P,B,\chi) = 0.7k_{\rm N}N_{\rm f}B_{12}^{8/7} \times (1+B_{12})^{-3.7}\frac{G(\cos\chi/P)}{\sin\chi},$$

where

$$G(\xi) = \frac{1-c(\xi)}{s^3(\xi)}(3.5+\frac{s^2(\xi)}{c^2(\xi)})c^{1.7}(\xi).$$

In this case, we used two auxiliary functions:

$$c(\xi) = B_{12}^{0.75}\xi^{1.4} = \cos\chi,$$
$$s(\xi) = (1-c^2(\xi))^{1/2} = \sin\chi.$$

To determine the derivative of the angle of inclination of the magnetic axis to the spin axis of the neutron star, we use the integral of motion in explicit form. If the Ruderman–Sutherland model is valid, then the plasma in neutron stars at the stage of an extinct radio pulsar will fill only the inner regions of the magnetosphere. Consequently, the energy losses for such pulsars can be assumed to be identical to the magnetodipole losses. Thus, the quantity $I = \cos\chi/P$ is conserved during the evolution. As a result, we obtain the derivative of the angle of axial inclination in the region of extinct radio pulsars

$$\dot{\chi} = -\frac{\dot{P}}{P}\cot\chi.$$

The differential equation for the distribution function $N_3(P,B)$ of pulsars at the supersonic propeller stage then takes the form

$$\frac{d}{dP}\left(N_3P^{-2}\right) = 3\times10^{-5}k_{\rm N}N_{\rm f}B_{12}^{20/7} \times (1+B_{12})^{-3.7}\frac{y}{P^2}G\left(\frac{y}{P}\right).$$

Here, we denoted $y = (1-P^4P_E^{-4})^{1/2}$.

The sought-for distribution function can then be represented as

$$N_3(P,B) = 3\times10^{-5}k_{\rm N}N_{\rm f}B_{12}^{20/7} \times (1+B_{12})^{-3.7}P^{-2}\int\limits_{P_{\rm min}}^{P}\frac{y}{P^2}G\left(\frac{y}{P}\right)dP,$$

where $k_{\rm N}\approx4.4$ is the normalization factor and $N_{\rm f}$ is the number of normal radio pulsars far from the death line (for more detail, see Beskin and Eliseeva (2005)).

Since the death line of normal radio pulsars

$$P_{\rm d}(\chi) = B_{12}^{8/15}(\cos\chi)^{0.29}\ {\rm s} \qquad (6)$$

crosses the boundary of the transition to the supersonic propeller stage at a fairly small angle χ ($\sin\chi = P_E^{-2}P^{0.125}$), the point of intersection of the death line for normal radio pulsars (6) with the $\sin\chi = 0$ axis can be taken with a good accuracy as the point with the minimum period $P_{\rm min}$ (see Fig. 1). It thus follows that

$$P_{\rm min} = B_{12}^{8/15}\ {\rm s}.$$

Since the period at which a pulsar passes from the ejector stage to the propeller stage is defined by Eq. (3) and the period at which a pulsar leaves the supersonic propeller stage is defined by Eq. (5), we derive the following expression for the period distribution function of neutron stars at the supersonic propeller stage:

$$N_3(P,B) = 3\times10^{-5}k_{\rm N}N_{\rm f}P^{-2} \times\int\limits_{5\times10^{-4}P^{7/6}}^{P^{15/8}}B_{12}^{20/7}(1+B_{12})^{-3.7} \times\int\limits_{B_{12}^{8/15}}^{P}\frac{y}{P^2}G\left(\frac{y}{P}\right)dP.$$

Figure 3 shows the distribution of pulsars at the supersonic propeller stage in period P for a value of $P_E = 100$ s. This distribution was constructed by assuming that the model with hindered particle escape from the neutron-star surface was valid. In addition, we assumed that no neutron stars are born at the supersonic propeller stage and did not consider the possibility of magnetic-field evolution over the lifetime of the pulsar at this stage. As we see from this figure, the number of such neutron stars is much

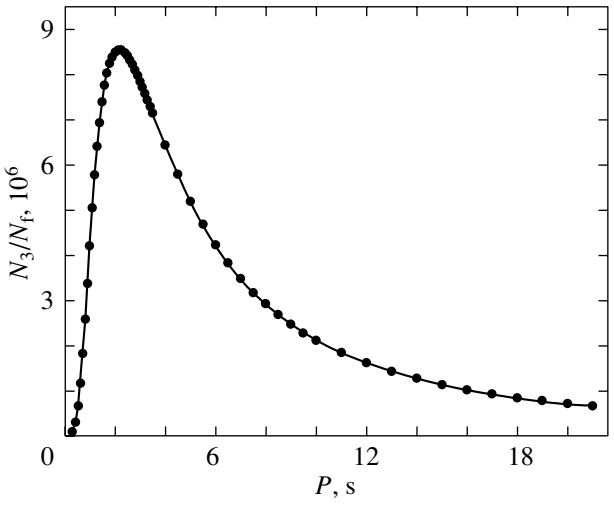

Fig. 3. Distribution of neutron stars at the supersonic propeller stage $N_3(P)$ for the model with hindered particle escape.

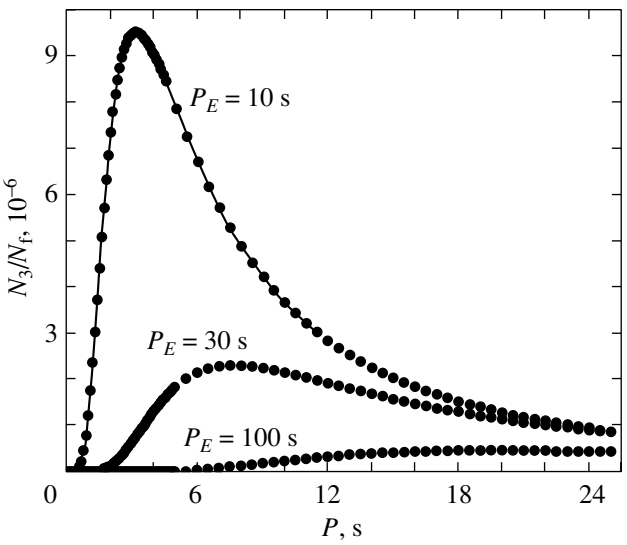

Fig. 4. Distribution of neutron stars at the supersonic propeller stage $N_3(P)$ for the model with free particle escape.

smaller than the number of both active and extinct radio pulsars.

As was noted above, when allowance is made for the evolution of the angle of inclination of the magnetic axis to the spin axis in the region of extinct radio pulsars (and, accordingly, for the boundary of the transition to the supersonic propeller stage), the transition to the propeller stage can occur even at fairly short spin periods of the neutron star. The numerically computed distribution of pulsars at the supersonic propeller stage shown in the figure confirms this conclusion. We also see from Fig. 3 that the total number of neutron stars increases compared to the standard model when allowance is made for the evolution of the inclination angle in the region of extinct radio pulsars and, accordingly, for the boundary of the transition to the propeller stage.

It should also be noted that if the model with hindered particle escape is valid, the limiting period P_E only slightly affects the distribution of neutron stars at the supersonic propeller stage. This situation arises from the fact that most of the neutron stars crossing the boundary of the region of extinct radio pulsars $\sin\chi = P^2/P_E^2$ have short spin periods, $P \ll 100$ s (Fig. 1).

THE MODEL WITH FREE PARTICLE ESCAPE FROM THE NEUTRON-STAR SURFACE

Recall that the boundary of the transition from the region of extinct radio pulsars to the supersonic propeller stage for the model with free particle escape from the neutron-star surface is specified by Eq. (4) (see Fig. 2). Consequently, the following relation is valid for the source function $F(P, B)$ determined by the neutron star flux from the region of extinct radio pulsars:

$$F(P,B) = F(P,B,\chi)|_{\cos\chi = P^2 P_E^{-2}}. \qquad (7)$$

Therefore, as for the Ruderman–Sutherland model, the source function $F(P, B, \chi)$ can be written as

$$F(P,B,\chi) = \dot{\chi} N_2. \qquad (8)$$

If the model by Arons (1979) is valid for the existing neutron stars, then, as was mentioned above, the neutron-star magnetosphere for extinct radio pulsars in the case of free particle escape still remains completely filled with plasma, which screens the magnetic field. As a result, all of the energy losses are attributable to longitudinal currents, while the magnetodipole losses are completely screened. In this case, the quantity $I_d = \sin\chi/P$ is conserved during the evolution at the ejector stage (including the region of extinct radio pulsars). It thus follows that the derivative of the angle of inclination of the magnetic axis to the spin axis of the neutron star is

$$\dot{\chi} = -\frac{\dot{P}}{P}\tan\chi. \qquad (9)$$

Based on our previous results, we use the following expression for the distribution function of extinct radio pulsars

$$N_2(P,B,\chi) \qquad (10)$$
$$= 0.3 k_N N_f \frac{B_{12}^{1.1}(1+B_{12})^{-3.7}}{\cos\chi[1+0.1B_{12}^{1.7}(\sin\chi/P)^{3.1}]^{0.9}}.$$

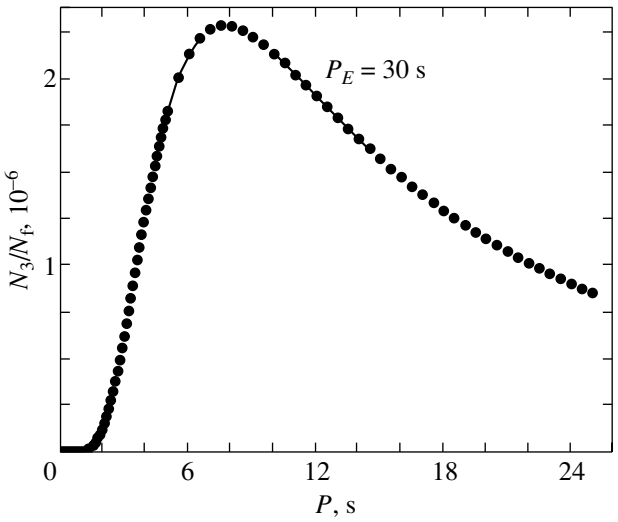

Fig. 5. Distribution of neutron stars at the supersonic propeller stage $N_3(P)$ for the model with free particle escape for the limiting period $P_E = 30$ s.

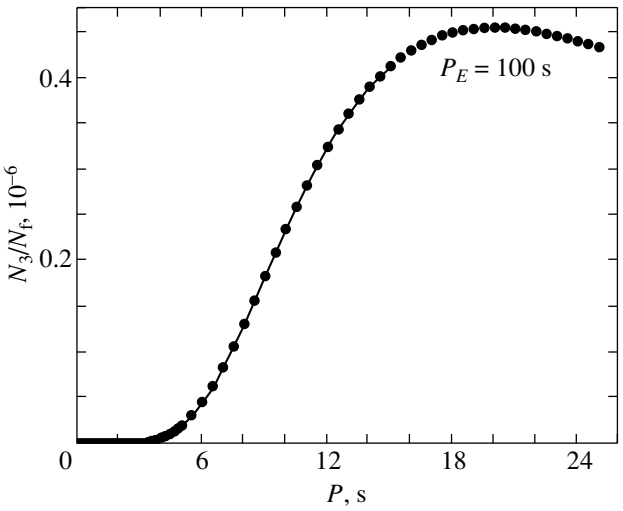

Fig. 6. Same as Fig. 5 for $P_E = 100$ s.

Let us change the variable

$$y = \sin\chi = 1 - \frac{P^4}{10^8 B_{12}^{1/2}}.$$

Substituting (7), (8), (9), and (10) into the kinetic equation (2) yields the differential equation for $N_3(P, B)$

$$\frac{d}{dp}(N_3 P^2) = 1.2 k_\mathrm{N} N_\mathrm{i} B_{12}^{2.74}(1 + B_{12})^{-3.7} \times P^{-27/14} \frac{y}{\left[1 + 0.1 B_{12}^{1.7}\,(y/P)^{3.1}\right]^{0.9}}.$$

The solution of this equation is the sought-for distribution function

$$N_3(P, B) = 1.2 \times 10^{-5} P_E k_\mathrm{N} N_\mathrm{i} B_{12}^{2.74}(1 + B_{12})^{-3.7} P^{-2} \times \int_{P_\mathrm{min}}^{P} \frac{y}{P^{27/14}} \frac{dP}{[1 + 0.1 B_{12}^{1.7}(y/P)^{3.1}]^{0.9}}. \quad (11)$$

To find the minimum spin period of a neutron star that passed to the supersonic propeller stage, let us turn to Fig. 2. We see from this figure that the point of intersection between the line of transition of pulsars to the region for which the angle of inclination of the magnetic axis to the spin axis is close to 90° ($\cos\chi = (\Omega R/c)^{1/2}$) and the line of transition from the region of extinct radio pulsars to the propeller stage (4), where $\Omega = 2\pi/P$ is the angular velocity of the neutron star, corresponds to this period. Thus, the minimum spin period of a neutron star at the supersonic propeller stage is

$$P_\mathrm{min} = 0.184 A^{4/5} B_{12}^{2/5}.$$

Here, we represented the limiting period P_E as $P_E = A B_{12}^{1/2}$.

As a result, we obtain the spin period distribution of neutron stars at the supersonic propeller stage for the model with free particle escape from the pulsar's surface by taking into account the boundaries of the transition of the neutron star to the supersonic propeller stage (4) and the subsonic propeller stage (5) and using the distribution function (11):

$$N_3(P) = 1.2 \times 10^{-5} P_E k_\mathrm{N} N_\mathrm{i} P^{-2} \times \int_{5\times10^{-4}P^{7/6}}^{69A^{-2}P^{5/2}} B_{12}^{2.74}(1 + B_{12})^{-3.7} \times \int_{0.185 P_E^{0.8}}^{P} \frac{y}{P^{27/14}} \frac{dP}{[1 + 0.1 B_{12}^{1.7}(y/P)^{3.1}]^{0.9}}.$$

Recall that in this expression, the normalization factor is $k_\mathrm{N} \approx 4.4$ and N_i is the number of normal radio pulsars far from the death line.

Figure 4 shows the distribution of neutron stars at the supersonic propeller stage in spin period P under the assumption that the model by Arons is valid for three limiting periods P_E: 10, 30, and 100 s. In addition, Figs. 5 and 6 separately show the distributions for $P_E = 30$ s and $P_E = 100$ s, respectively. As can be seen from these figures, when allowance is made for the evolution of the inclination angle χ at the ejector stage and, accordingly, for the boundary

of the transition to the propeller stage, the number of neutron stars at the supersonic propeller stage is indeed found to be significant at fairly short spin periods ($P \sim 5$–10 s). Thus, a consistent allowance for the angle of inclination of the magnetic axis to the spin axis of the neutron star at the ejector stage leads to an increase in the number of pulsars that passed to the supersonic propeller stage.

It should also be noted that, in contrast to the model with hindered particle escape from the neutron-star surface, the limiting period P_E plays a significant role in the distribution of neutron stars at the supersonic propeller stage for the model by Arons. This is because the distribution of neutron stars at the boundary of the transition from the region of extinct radio pulsars to the propeller stage is virtually uniform for this model.

CONCLUSIONS

We have determined the distributions of neutron stars at the supersonic propeller stage in spin period P and took into account the fact that a consistent allowance for the evolution of the angle of inclination of the magnetic axis to the spin axis for the region of extinct radio pulsars directly affects the statistics of neutron stars at the supersonic propeller stage. All our calculations were performed for two models of the particle acceleration region: the model with hindered particle escape from the neutron-star surface (Ruderman and Sutherland 1975) and the model with free particle escape (Arons 1979).

As a result, we have made sure once again that a consistent allowance for the evolution of the inclination angle χ in the region of extinct radio pulsars both for the model with hindered particle escape and for the model with free particle escape leads to an increase in the total number of neutron stars at the supersonic propeller stage. This increase stems from the fact that when the inclination angle χ for the evolution of neutron stars in the region of extinct radio pulsars and, hence, for the boundary of the transition to the supersonic propeller stage is included, this transition is possible at shorter spin periods of the neutron star ($P \sim 5$–10 s) than assumed in the standard model.

ACKNOWLEDGMENTS

We would like to thank S.B. Popov and M.E. Prokhorov for fruitful discussions and plentiful advice. This work was supported by the Russian Foundation for Basic Research (project no. 05-02-17700).

REFERENCES

1. J. Arons, Space Sci. Rev. **24**, 437 (1979).
2. V. S. Beskin and S. A. Eliseeva, Pis'ma Astron. Zh. **31**, 290 (2005) [Astron. Lett. **31**, 263 (2005)].
3. V. S. Beskin, A. V. Gurevich, and Ya. N. Istomin, *Physics of the Pulsar Magnetosphere* (Cambridge Univ. Press, Cambridge, 1993).
4. R. E. Davies and J. E. Pringle, Mon. Not. R. Astron. Soc. **196**, 209 (1981).
5. R. E. Davies, A. C. Fabian, and J. E. Pringle, Mon. Not. R. Astron. Soc. **186**, 779 (1979).
6. N. R. Ikhsanov, Astron. Astrophys. **399**, 1147 (2003).
7. A. F. Illarionov and R. A. Syunyaev, Astron. Astrophys. **39**, 185 (1975).
8. V. M. Lipunov, *Astrophysics of Neutron Stars* (Nauka, Moscow, 1987) [in Russian].
9. V. M. Lipunov and S. B. Popov, Astron. Zh. **71**, 711 (1995) [Astron. Rep. **39**, 632 (1995)].
10. V. M. Lipunov, K. A. Postnov, and M. E. Prokhorov, Astrophys. Space Phys. **9**, 1 (1996).
11. L. Mestel, *Stellar Magnetism* (Oxford Univ. Press, Oxford, 1999).
12. S. B. Popov and M. E. Prokhorov, astro-ph/0205298 (2002).
13. M. A. Ruderman and P. G. Sutherland, Astrophys. J. **196**, 51 (1975).
14. V. F. Schwarzman, Izv. Vyssh. Uchebn. Zaved. Radiofiz. **13**, 1852 (1970).

Translated by V. Astakhov

Astronomy Letters, Vol. 31, No. 9, 2005, pp. 586–590. Translated from Pis'ma v Astronomicheskiĭ Zhurnal, Vol. 31, No. 9, 2005, pp. 656–660.

Criteria for Identification of Subsonic Propellers

N. R. Ikhsanov[1, 2*]

[1] *Pulkovo Astronomical Observatory, Russian Academy of Sciences, Pulkovskoe sh. 65, St. Petersburg, 196140 Russia*

[2] *Korea Astronomy and Space Science Institute, Taejon, South Korea*

Received November 17, 2004

Abstract—The state of a subsonic propeller in the evolutionary tracks of magnetized compact stars is intermediate between the states of a supersonic propeller and an accretor. We show that neutron stars in this state would manifest themselves as accretion-powered pulsars of low (or moderate) luminosity. The criteria that allow subsonic propellers to be distinguished from accretors include a soft X-ray spectrum, a limited range of admissible spin periods, and a rapid spindown. © *2005 Pleiades Publishing, Inc.*

Key words: *pulsars, neutron stars, high-mass binaries.*

INTRODUCTION

Neutron stars in high-mass binaries can be in one of the following four states: an ejector, a supersonic propeller, a subsonic propeller, and an accretor (Davies *et al.* 1979; Lipunov 1987). Ejectors and accretors have been identified with radio (ejection) and accretion-powered pulsars, respectively. Analysis of the X-ray spectra for a number of Be/X-ray transients allows the state of the neutron star during the quiescent phase of the source to be identified with the state of a supersonic propeller (Campana *et al.* 2002; Menou and McClintock 2001). Whether subsonic propellers can be identified observationally is still an open question.

A SUBSONIC PROPELLER

The stage of a subsonic propeller in the evolutionary tracks of neutron stars is intermediate between the stages of a supersonic propeller and an accretor. The spin period of subsonic propellers is limited below by the condition

$$P_{\rm s} > P_{\rm cd} = 23\mu_{30}^{6/7} m^{-5/7} \left[\frac{\dot{M}_{\rm c}}{10^{15}\ {\rm g\ s^{-1}}}\right]^{-3/7}\ {\rm s}, \quad (1)$$

under which the corotation radius of the star, $R_{\rm cor} = (GMP_{\rm s}^2/4\pi^2)^{1/3}$, exceeds the radius of its magnetosphere,

$$R_{\rm m} = \left(\frac{\mu^2}{\dot{M}_{\rm c}\sqrt{2GM_{\rm ns}}}\right)^{2/7}. \quad (2)$$

Here, μ_{30} and m denote the magnetic moment and the mass of the neutron star in units of 10^{30} G cm^3 and $M_\odot$, respectively; $\dot{M}_{\rm c}$ is the mass of the matter with which the neutron star moving through the stellar wind from its massive companion interacts per unit time:

$$\dot{M}_{\rm c} = \pi R_{\rm G}^2 \rho_\infty V_{\rm rel}; \quad (3)$$

ρ_∞ is the mean density of the matter surrounding the neutron star at the distance of its gravitational radius $R_{\rm G} = 2GM_{\rm ns}/V_{\rm rel}$; and $V_{\rm rel}$ is the velocity of the neutron star relative to the stellar wind from its massive companion.

At $P_{\rm s} > P_{\rm cd}$, the shape of the surface of the stellar magnetosphere is described by the solution obtained by Arons and Lea (1976). The stability condition for the boundary of this magnetosphere is given by the inequality

$$T(R_{\rm m}) > 0.3T_{\rm ff} = 0.3\frac{GMm_{\rm p}}{kR_{\rm m}}, \quad (4)$$

where $T(R_{\rm m})$ is the temperature of the plasma surrounding the stellar magnetosphere, $T_{\rm ff}$ is the free-fall temperature, and $m_{\rm p}$ and k are the proton mass and the Boltzmann constant, respectively. This implies that the interchange instabilities of the magnetospheric boundary are suppressed as long as the heating of the plasma surrounding the star dominates over its cooling. The satisfaction of this condition defines the upper limit for the spin period of subsonic propellers (Ikhsanov 2001a)

$$P_{\rm s} < P_{\rm br} \simeq 450\mu_{30}^{16/21} \left[\frac{\dot{M}_{\rm c}}{10^{15}\ {\rm g\ s^{-1}}}\right]^{-5/7} m^{-4/21}\ {\rm s}. \quad (5)$$

*E-mail: ikhsanov@kasi.re.kr

1063-7737/05/3109-0586$26.00

As was first shown by Davies and Pringle (1981), a neutron star at the subsonic propeller stage is surrounded by a hot ($T \simeq T_{\rm ff}$) quasi-static envelope that extends from the magnetospheric boundary to its gravitational radius. According to numerical simulations (Romanova *et al.* 2003), this approximation is valid if the star has a fairly strong magnetic field. The envelope formation prevents the stellar wind from penetrating under the gravitational capture radius. During the motion of the star together with the envelope surrounding its magnetosphere, the stellar wind from its normal companion flows around the outer boundary of the envelope. The mass of the gas flowing around the envelope per unit time (the flow rate) is $\dot{M}_{\rm c}$. The interaction between the envelope and the matter flowing around it removes the excess angular momentum transferred by the neutron star to the surrounding plasma at its magnetospheric boundary and transported by turbulent motions to the outer boundary of the envelope (see Fig. 1).

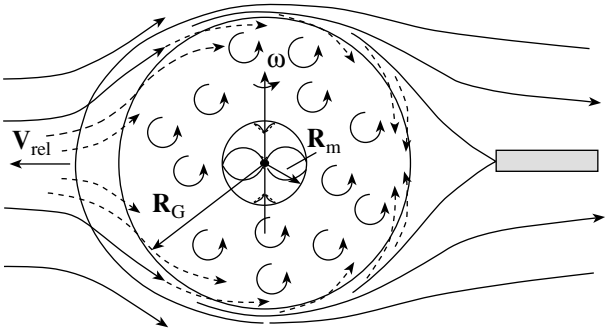

Fig. 1. A neutron star in the propeller state. The stellar magnetosphere is surrounded by a hot quasi-static envelope. During the motion of the star, the surrounding matter flows around the outer boundary of the envelope at the rate $\dot{M}_{\rm c}$.

ACCRETION ONTO A SUBSONIC PROPELLER

The interchange instabilities of the magnetospheric boundary are not the only mechanism of plasma penetration into the magnetic field of neutron stars. Diffusion is an alternative mechanism. Since the envelope plasma conductivity is finite, a diffusion layer of plasma and magnetic field interpenetration (the magnetopause) is formed at the magnetospheric boundary. The thickness of this layer can be estimated using the expression $\delta_{\rm m} = \sqrt{D_{\rm eff} t_{\rm diff}}$, where $D_{\rm eff}$ and $t_{\rm diff}$ are the effective diffusion coefficient and time, respectively. The lower limit for $D_{\rm eff}$ is the Bohm diffusion coefficient $D_{\rm B} \simeq \zeta V_{\rm T_i} r_{\rm h_i}$, where $V_{\rm T_i}$ and $r_{\rm h_i}$ are the thermal velocity of the ions and their Larmor radius, respectively, and the dimensionless parameter ζ lies within the range 0.1–0.25 (Gosling *et al.* 1991). The upper limit for this parameter depends on the spectrum of turbulent motions at the magnetospheric boundary and can exceed significantly $D_{\rm B}$ under certain conditions (Anzer and Börner 1983).

The characteristic diffusion time is the time in which the plasma that diffuses into the magnetopause can escape from it by moving along the magnetic field lines toward the magnetic poles. The absolute lower limit for this quantity is the free-fall time, $t_{\rm ff} = R_{\rm m}^{3/2}/(GM_{\rm ns})^{1/2}$. However, the actual diffusion time can exceed significantly $t_{\rm ff}$. In particular, such a situation takes place in the case of a subsonic propeller.

The plasma penetrating into the stellar magnetic field is isolated from the region of main energy release via the propeller operation, and its motion inside the magnetosphere is controlled completely by the magnetic field. However, the plasma can move along the magnetic field lines toward the magnetic poles of the star only after the temperature of the plasma diffusing into the magnetopause has decreased to a critical value of $\sim 0.3 T_{\rm ff}$. Otherwise, the effective acceleration of a particle in the magnetopause region (Arons and Lea 1976),

$$g_{\rm eff} = \frac{GM_{\rm ns}}{R_{\rm m}^2(\psi)} \cos\psi - \frac{V_{\rm T_i}^2(R_{\rm m})}{R_{\rm curv}(\psi)}, \qquad (6)$$

would be negative (the centrifugal acceleration attributable to the curvature of magnetic field lines and described by the second term on the right-hand side dominates over the acceleration attributable to the gravitational potential of the neutron star and described by the first term on the right-hand side); therefore, the resultant force applied to this particle is directed away from the neutron star. Here, ψ denotes the angle between the radius vector and the normal to the magnetic field line, and $R_{\rm curv}(\psi)$ is the curvature of the magnetic field lines at the magnetospheric boundary that corresponds to the solution obtained by Arons and Lea (1976).

The main plasma cooling mechanism under the conditions of interest is bremsstrahlung (the cooling through cyclotron radiation and Compton scattering is inefficient due to the relatively small magnetic field strength in the magnetopause and the relatively low X-ray luminosity of the star). The characteristic cooling time can be expressed as

$$t_{\rm br} \simeq 5.4 \times 10^4 \mu_{30}^{4/7} m^{6/7} \left[\frac{\dot{M}_{\rm c}}{10^{15}\ {\rm g\ s^{-1}}}\right]^{-9/7} {\rm s} \qquad (7)$$

(note that the time it takes for the electron and ion temperatures to be equalized in the conditions under consideration is much shorter than the bremsstrahlung cooling time. Comparing this time with the free-

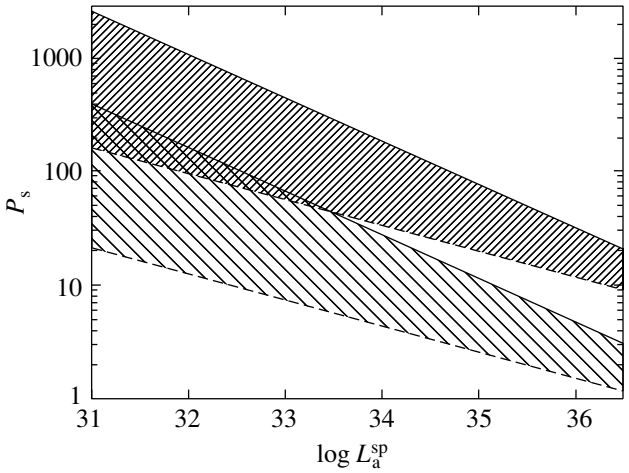

Fig. 2. Ranges of admissible spin periods for subsonic propellers as a function of their accretion luminosity for stars with magnetic dipole moments of $\mu = 10^{30}$ G cm^3 (sparse hatching) and $\mu = 10^{31}$ G cm^3 (dense hatching). These ranges are limited below and above by the periods P_{cd} and P_{br}, respectively.

fall time in the magnetopause region, we find that

$$\theta = \frac{t_{ff}}{t_{br}} \simeq 5 \times 10^{-5} \mu_{30}^{2/7} m^{-11/7} \left[\frac{\dot{M}_c}{10^{15}\ \mathrm{g\ s^{-1}}}\right]^{6/7}. \quad (8)$$

Thus, the characteristic time of plasma outflow from the magnetopause along the magnetic field lines toward the star exceeds significantly the free-fall time. Consequently, the characteristic time of accretion onto the surface of a neutron star in the state of a subsonic propeller is $t_a \gtrsim t_{br} \gg t_{ff}$, and, accordingly, the maximum accretion rate onto the surface of such an object is limited as follows:

$$\dot{M}_a \lesssim \dot{M}_a^{max} \simeq \theta \dot{M}_c \quad (9)$$
$$\simeq 5 \times 10^{10} \mu_{30}^{2/7} m^{-11/7} \left[\frac{\dot{M}_c}{10^{15}\ \mathrm{g\ s^{-1}}}\right]^{13/7} \mathrm{g\ s^{-1}}.$$

It follows from this expression that the accretion luminosity of subsonic propellers can be estimated as

$$L_x^{sp} \lesssim L_a^{sp} \quad (10)$$
$$\simeq 7 \times 10^{30} \mu_{30}^{2/7} m^{-4/7} R_6^{-1} \left[\frac{\dot{M}_c}{10^{15}\ \mathrm{g\ s^{-1}}}\right]^{13/7} \mathrm{erg\ s^{-1}},$$

where R_6 is the radius of the neutron star in units of 10^6 cm.

The accreting plasma reaches the neutron-star surface near the magnetic poles. As a result, two hot spots whose radiation is concentrated in the X-ray spectral range are formed on the stellar surface. Assuming that the magnetic and spin axes of the star are not aligned, we arrive at the classical picture of an accretion-powered X-ray pulsar. Thus, one may expect the neutron stars at the subsonic propeller stage to manifest themselves as accreting pulsars of low (or moderate) luminosity. At the same time, as we show in the next section, there are several significant differences in the manifestations of subsonic propellers and accretors.

PECULIARITIES IN THE MANIFESTATIONS OF SUBSONIC PROPELLERS

One of the criteria for identifying subsonic propellers is the following constrain imposed on the range of admissible spin periods: $P_{cd} < P_s < P_{br}$. The boundaries of this range depend on two main parameters: μ and $\dot{M}_c$. The admissible range of spin periods as a function of the subsonic-propeller luminosity ($L_x = \dot{M}_a G M_{ns}/R_{ns}$) can be determined by assuming that the accretion rate onto the surface of a neutron star in the state of a subsonic propeller is close to its maximum possible value (see (9)). The corresponding dependences are shown in Fig. 2. As we see from this figure, the range of admissible spin periods narrows significantly as the X-ray luminosity of the source increases.

The next important criterion that allows subsonic propellers to be distinguished from accretors of low (and moderate) luminosity is their relatively soft X-ray spectrum. The cause of this difference is as follows. The area of the hot spots near the magnetic poles of a neutron star in the regime of spherical accretion can be estimated, to the first approximation, as $S_{pol} \simeq \pi R_{ns}^3 R_m^{-1}$ (Lipunov 1987). If the star is in the state of an accretor, i.e., $\dot{M}_c = \dot{M}_a$, then the area of the hot spot can be expressed in terms of its X-ray luminosity as

$$S_{pol}^{acc} \simeq 6.4 \times 10^8 L_{33}^{2/7} m^{1/7} \mu_{30}^{-4/7} R_6^{23/7}\ \mathrm{cm^2}, \quad (11)$$

where L_{33} is the X-ray luminosity of the source in units of 10^{33} erg s^{-1}.

However, in the case of a subsonic propeller, $\dot{M}_c \gg \dot{M}_a$, and, hence, expression (9) should be used to calculate the function $S_{pol}^{sp}(L_x)$. As a result, we obtain

$$S_{pol}^{sp} \simeq 1.7 \times 10^{10} L_{33}^{2/13} m^{3/13} \mu_{30}^{-8/13} R_6^{42/13}\ \mathrm{cm^2}. \quad (12)$$

Comparison of expressions (11) and (12) leads us to conclude that the area of the hot spot on the surface of a neutron star in the state of a subsonic propeller is almost a factor of 30 larger than the spot area on the surface of a neutron star in the accretor state of

the same luminosity. A blackbody fit to the X-ray spectrum suggests that the effective radiation temperature of a subsonic propeller (other things being equal) is more than a factor of 2 lower than that of a neutron star in the accretor state. Thus, one may expect the subsonic propellers to manifest themselves as X-ray pulsars of low (or moderate) luminosity with an anomalously soft spectrum.

This difference between subsonic propellers and accretors is even more significant if matter is accreted onto the neutron star in the regime of an accretion disk. In this case, the accretion column is a hollow cylinder (Basko and Sunyaev 1976), and, accordingly, the area of the emitting region near the magnetic poles is smaller that its value given by expression (11).

One of the important criteria for observational identification of subsonic propellers is their relatively high spindown rate and regularity. Indeed, following Davies and Pringle (1981), let us write the rate of rotational energy loss by a neutron star in the state of a subsonic propeller as

$$L^{\rm sp} = 8\times10^{33}\mu_{30}^2 m^{-1}\left(\frac{P_{\rm s}}{5{\rm s}}\right)^{-3}\ {\rm erg\,s^{-1}}. \quad (13)$$

This implies that the spin period of subsonic propellers, on average, increases at a rate

$$\dot{P} = \frac{P_{\rm s}^3 L^{\rm sp}}{4\pi^2 I} \sim 2.5\times10^{-11}\mu_{30}^2 m^{-1} I_{45}^{-1}\ {\rm s\,s^{-1}}, \quad (14)$$

where I_{45} is the moment of inertia of the neutron star in units of 10^{45} g cm^2.

Finally, since the maximum possible mass capture rate by a neutron star in the regime of a subsonic propeller from the stellar wind of the massive companion exceeds significantly the accretion rate onto its surface, we can make a correction to the method for identifying the state of a neutron star by its X-ray luminosity, magnetic field strength, and spin period. Comparison of the magnetospheric and corotation radii of the neutron star underlies this method. However, whereas the corotation radius does not depend on the state in which the compact star is, the determination of the magnetospheric radius is model-dependent. The main parameter in calculating this quantity for stars with an independently determined magnetic field strength is the mass capture rate from the stellar wind of the normal companion. In general, this parameter can be estimated from the observed X-ray luminosity of the object: $\dot{M} = L_{\rm x}R_{\rm ns}/GM_{\rm ns}$. At the same time, this estimate allows us to calculate the accretion rate onto the stellar surface, i.e., $\dot{M}_{\rm a}$, which can be set equal to the mass capture rate, $\dot{M}_{\rm c}$, only if the star is in the accretor state. In the case of a subsonic propeller, calculating the mass capture rate from the X-ray luminosity of the object requires allowing for expression (9). The value of $\dot{M}_{\rm c}$ turns out to be a factor of θ^{-1} higher than the accretion rate onto the neutron-star surface calculated from its accretion luminosity. Thus, the magnetospheric radius of a subsonic propeller calculated from the observed X-ray luminosity is a factor of $\theta^{-2/7}$ smaller than the magnetospheric radius of a star with the same luminosity and the same magnetic field, but in the accretor state. For the parameters of interest, the correction is

$$\theta^{-2/7} \simeq 17\mu_{30}^{-4/49} m^{22/49}\left[\frac{\dot{M}_{\rm c}}{10^{15}\ {\rm g\,s^{-1}}}\right]^{-12/49} \quad (15)$$

for a spherically symmetric accretion flow and a factor of about 2 lower than that for disk accretion.

Thus, we arrive at yet another possible criterion for identifying stars in the state of a subsonic propeller. More specifically, pulsars for which the magnetospheric radius calculated using the equality $\dot{M}_{\rm a} = \dot{M}_{\rm c}$ exceeds the corotation radius are candidates for objects of this class. The application of this criterion to the X-ray transient A0535+26 of anomalously low luminosity was discussed previously (Ikhsanov 2001b).

CONCLUSIONS

The main criteria that allow subsonic propellers to be distinguished from accretors are:

(1) a limited range of admissible spin periods for subsonic propellers, which is a function of their luminosity (see Fig. 2);

(2) a relatively soft X-ray spectrum of subsonic propellers;

(3) rapid spindown of stars that manifest themselves as accretion-powered X-ray pulsars.

These criteria can be used to select candidates for subsonic propellers from among X-ray pulsars of low (or moderate) luminosity.

ACKNOWLEDGMENTS

I am grateful to L.A. Pustil'nik, N.G. Beskrovnaya, and A.I. Tsygan for valuable discussions and help in preparing the article. This work was supported by the Korea Science and Engineering Foundation (project KOSEF R01-2004-000-1005-0), the Russian Foundation for Basic Research (project no. 03-02-17223a), and the *Astronomy* Program.

REFERENCES

1. U. Anzer and G. Börner, Astron. Astrophys. **122**, 73 (1983).
2. J. Arons and S. M. Lea, Astrophys. J. **207**, 914 (1976).
3. M. M. Basko and R. A. Sunyaev, Mon. Not. R. Astron. Soc. **175**, 379 (1976).
4. S. Campana, L. Stella, G. L. Israel, *et al.*, Astrophys. J. **580**, 387 (2002).
5. R. E. Davies and J. E. Pringle, Mon. Not. R. Astron. Soc. **196**, 209 (1981).
6. R. E. Davies, A. C. Fabian, and J. E. Pringle, Mon. Not. R. Astron. Soc. **186**, 779 (1979).
7. J. T. Gosling, M. F. Thomsen, S. J. Bame, *et al.*, J. Geophys. Res. **96**, 14 097 (1991).
8. N. R. Ikhsanov, Astron. Astrophys. **368**, L5 (2001a).
9. N. R. Ikhsanov, Astron. Astrophys. **367**, 549 (2001b).
10. V. M. Lipunov, *Astrophysics of Neutron Stars* (Nauka, Moscow, 1987) [in Russian].
11. K. Menou and J. E. McClintock, Astrophys. J. **557**, 304 (2001).
12. M. M. Romanova, O. D. Toropina, Yu. M. Toropin, and R. V. E. Lovelace, Astrophys. J. **588**, 400 (2003).

Translated by V. Astakhov

Astronomy Letters, Vol. 31, No. 9, 2005, pp. 591–597. Translated from Pis'ma v Astronomicheskiĭ Zhurnal, Vol. 31, No. 9, 2005, pp. 661–668.

Region of Anomalous Compression Under Bondi–Hoyle Accretion

R. V. Shcherbakov*

Moscow Institute of Physics and Technology, Institutskiĭ per. 9, Dolgoprudnyĭ, Moscow oblast, 141700 Russia

Received March 15, 2005

Abstract—We investigate the properties of an axisymmetric gas flow without angular momentum onto a small compact object, in particular, on a Schwarzschild black hole in the supersonic region; the velocity of the object itself is assumed to be low compared to the speed of sound at infinity. First of all, we show that the streamlines intersect (i.e., a caustic is formed) on the symmetry axis at a certain distance r_x from the center on the front side if the pressure is ignored. The characteristic radial size of the region in which the streamlines emerging from the sonic surface at an angle no larger than θ_0 to the axis intersect is $\Delta r = r_x\theta_0^2/3$. To refine the flow structure in this region, we have numerically computed the system without ignoring the pressure in the adiabatic approximation. We have estimated the parameters of the inferred region with anomalously high matter temperature and density accompanied by anomalously high energy release. © *2005 Pleiades Publishing, Inc.*

Key words: *black holes, accretion.*

INTRODUCTION

Bondi–Hoyle accretion is the fall of matter onto a moving compact object. Although this problem was formulated back in the mid-20th century (Bondi and Hoyle 1944), many details of this process are still incomprehensible. In particular, there is virtually no detailed information about the properties of a flow in the supersonic region near a gravitating center in the model of smooth passage of the sonic surface (Bondi 1952).

The first-order correction to spherically symmetric accretion was first considered to calculate the accretion onto a nonrotating compact object moving through a gas (Beskin and Pidoprygora 1995). In this case, the ratio of the object's velocity v_∞ to the speed of sound at an infinite distance from the body c_∞ plays the role of a small parameter:

$$\varepsilon = \frac{v_\infty}{c_\infty}.$$

We consider only the first approximation with $\varepsilon \le 1$. This inequality holds for certain astrophysical objects. Accretion without shock formation is possible in this case. Since spherically symmetric smooth transonic accretion was shown (Bondi 1952; Garlick 1979) to be stable, it has physical meaning. It can then be assumed that Bondi–Hoyle accretion without shock formation is also stable at fairly small ε and, hence, also has physical meaning.

*E-mail: shcher@dgap.mipt.ru, avalon@lpi.ru

Recall the main properties of the smooth spherically symmetric solution denoted by the superscript $^{(0)}$ and the first approximation to it denoted by the superscript $^{(1)}$ (Bondi 1952; Beskin and Pidoprygora 1995). The solution is sought in the adiabatic approximation with a constant adiabatic index Γ. All of the coefficients k with different subscripts that appear below were calculated by Beskin and Pidoprygora (1995) and depend only on the adiabatic index Γ.

(1) The requirement of smoothness, i.e., the absence of shocks, leads to an additional condition on the sonic surface that yields $r_* = r_*^{(0)} + r_*^{(1)}$ for the radius of the sonic surface in the nonrelativistic limit, where in polar (r, θ, ϕ) coordinates

$$r_*^{(0)} = \left(\frac{5-3\Gamma}{4}\right)\frac{Gm}{c_\infty^2},$$

$$r_*^{(1)} = \varepsilon r_*^{(0)}\left(\frac{\Gamma+1}{5-3\Gamma}\right)k_1(\Gamma)\cos\theta.$$

(2) The Grad–Shafranov equation that defines the stream function $\Phi(r,\theta)$ has the solution $\Phi = \Phi^{(0)} + \Phi^{(1)}$, where

$$\Phi^{(0)} = \Phi_0(1-\cos\theta), \qquad (1)$$

$$\Phi^{(1)} = \Phi_0\varepsilon g(r)\sin^2\theta.$$

Here, $2\Phi_0$ is the accretion rate, the stream function is defined as $n\mathbf{v} = \nabla\Phi \times \mathbf{e}_\phi/2\pi r\sin\theta$, and $\mathbf{e}_\phi$ is a unit vector along the ϕ axis.

1063-7737/05/3109-0591$26.00

(3) The radial function $g(r)$ asymptotically behaves as $g(r) = K(\Gamma)\,(r/r_*)^2$ far from the sonic surface, which corresponds to a uniform flow. On the other hand, in the supersonic region $r \ll r_*$,

$$g(r) = k_{\rm in}(\Gamma)\,(r/r_*)^{-1/2}, \qquad (2)$$

where r_* is the radius of the sonic surface.

(4) We see that the perturbation $\Phi^{(1)}$ becomes significant in the supersonic region, while $\max_\theta(\Phi^{(1)}/\Phi_0)$ reaches unity at

$$r_x = r_*(\varepsilon k_{\rm in})^2; \qquad (3)$$

in this case, perturbation theory loses its meaning, and exact equations need to be solved.

In this paper, we describe the method used and the simplifications that help to realize it. We prove that these can be introduced without any significant loss of estimation accuracy and give basic formulas and results. Subsequently, we discuss whether this phenomenon is observable.

DESCRIPTION OF THE METHOD

The essence of the described method is to directly calculate the streamline, which allows the physically observable quantities to be easily found. This method is also the most natural for deriving equations that become more obvious.

Let us parametrize the streamline as $\theta = \theta(\theta_0, r)$. The initial polar angle θ_0 at a certain radius r_0 and the radius r are independent variables. We choose r_0 in the supersonic region where it makes sense to consider the first approximation. The thermodynamic potentials are functions of the same arguments.

First of all, note that this parametrization is unique. However, to determine the flow pattern, we must specify not only the trajectory, but also the velocity along it $v(\theta(\theta_0, r), r)$. In this case, two differential equations for the two functions v and θ are set up, which must then be solved. These are the energy equation and the continuity equation.

The problem is solved by assuming the absence of energy release at the stellar boundary; i.e., the object is actually assumed to be a black hole. There is no angular momentum along the $\theta = 0$ axis.

SIMPLIFYING ASSUMPTIONS

Let us introduce several simplifications none of which, as we will see, affects significantly the result.

(1) In our calculations, we use the metric of flat space.

(2) The radial velocity of the matter v_r is much higher than its nonradial velocity v_θ. Therefore, the tangential components of the gradients for all parameters of the system are much smaller than their radial components.

(3) To determine the radial velocity, we ignore the enthalpy of the matter compared to the gravitational energy.

(4) The solution can be represented as a converging series in θ_0 in the form

$$\theta = \sum_{n=0}^{\infty} {\theta_0}^{2n+1} k_{2n+1}(r)$$

on the front side of a compact object near the symmetry axis ($\theta(0, r) = 0$ on the axis).

BASIC EQUATIONS

Let us first solve the problem by disregarding the pressure in the supersonic region. We go to the frame of reference in which the body is at rest and the gas flows on it. Let us write that the angular momentum of the gas relative to the center of the object is conserved

$$\frac{d}{dt}\left(r^2\frac{d\theta}{dt}\right) = 0.$$

Next, we can write the expression for the radial velocity as

$$v_{\rm tot} \approx |v_r| = -\frac{dr}{dt} \approx \sqrt{\frac{r_{\rm g}}{r}}, \qquad (4)$$

where $r_{\rm g} = 2GM/c^2$ is the gravitational radius of an object of mass M. By eliminating dt from these equations, we immediately determine the streamline as

$$\frac{\partial}{\partial r}\left(r^{3/2}\frac{\partial\theta}{\partial r}\right) = 0.$$

The solution of this equation that satisfies the natural initial condition $\theta(\theta_0, r_0) = \theta_0$ is

$$\theta = \theta_0 - C(\theta_0)\left[\left(\frac{r_0}{r}\right)^{1/2} - 1\right]. \qquad (5)$$

We derive the form of the function $C(\theta_0)$ from (2), which yields the same solution for the streamline, but has a limited validity range as the first approximation. As a result, we obtain

$$\theta(\theta_0, r) = \theta_0 - \varepsilon k_{\rm in}\sqrt{r_*}\left(\frac{1}{\sqrt{r}} - \frac{1}{\sqrt{r_0}}\right)\sin\theta_0.$$

This expression has a nontrivial structure. It defines the caustic near the distance $R_{\rm ball}$ from the center where

$$R_{\rm ball} = r_*(\varepsilon k_{\rm in})^2.$$

For physically meaningful Γ ($\Gamma > 1.25$), this caustic is located on the front side of the object, although the saddle point with zero gas velocity is always on the rear side. The characteristic radial size of the region in which the streamlines emerging from the sonic surface at an angle no larger than θ_0 to the axis intersect is $\Delta r = R_{\rm ball}\theta_0^2/3$. Naturally, the gas pressure cannot be ignored in a region of significant compression; the trajectories will not intersect if the pressure is included. We can qualitatively predict that, in this case, a certain region of strong compression will be closer to the object than $R_{\rm ball}$.

Next, let us perform calculation without ignoring the pressure. Let us set up a continuity equation for the gas flow. The area of the cross-sectional element of the flow in a direction perpendicular to the radius is

$$\delta S = 2\pi r^2 \sin\theta\delta\theta. \quad (6)$$

The continuity equation itself from which we find the number density n can then be written as

$$v_r n\delta S = \text{const}. \quad (7)$$

Using (4) and (6), we obtain from (7)

$$r^{3/2} n \sin\theta\delta\theta = {r_0}^{3/2} n_0 \sin\theta_0\delta\theta_0,$$

where θ is a function of θ_0 at r_0. We then get

$$\frac{\delta\theta}{\delta\theta_0} = \partial_{\theta_0}\theta(\theta_0, r).$$

Hence, the number density can be written as

$$n = n_0\left(\frac{r_0}{r}\right)^{3/2}\frac{\sin\theta_0}{\sin\theta}\frac{1}{\partial_{\theta_0}\theta}. \quad (8)$$

Below, for simplicity, we consider an adiabatic process on an ideal gas, $p = k(s)n^\Gamma$, where the entropy s is constant in the entire space. The pressure, the temperature, and the speed of sound can then be expressed using (8).

We can now calculate the curvature of a streamline under the effect of pressure. The force of gravity and a force proportional to ∇p act on a point mass of matter. Let us derive an equation for the change in the angular momentum of the gas, with the moment of the force of gravity being equal to zero. By the angular momentum we mean the vector perpendicular to the cross-section through the symmetry axis. We will use assumption (3) and assume that ∇p is perpendicular to the radius.

The momental equation is

$$\frac{d}{dt}\Delta L = -\Delta K,$$

where L is the angular momentum, and K is the moment of force. The minus corresponds to the repulsion of streamlines.

The force acting on a small element is $\Delta F = l\Delta r\Delta p$, where l is the length of the circumference described in the plane perpendicular to the $\theta = 0$ axis. The corresponding moment of force is $\Delta K = lr\Delta r\Delta p$, and the mass of this element is $\Delta m = m_{\rm p} nlr\Delta\theta\Delta r$, where $m_{\rm p}$ is the mass of a single particle. Its angular momentum is $\Delta L = m_{\rm p} nlr\Delta\theta\Delta r r^2 d\theta/dt$. Finally, we find that

$$\frac{d}{dt}\left(r^2\frac{d\theta}{dt}\right) = -\frac{\Delta p}{\Delta\theta m_{\rm p} n}.$$

At $r = \text{const}$, we obtain $p = p(\theta_0)$ and $\theta = \theta(\theta_0)$; therefore, $\Delta p/\Delta\theta = \partial_{\theta_0} p(\theta_0, r)/\partial_{\theta_0}\theta(\theta_0, r)$. We replace the differentiation with respect to t by the differentiation with respect to r using (4):

$$\partial_r\left[r^{3/2}\partial_r\theta(\theta_0, r)\right] = -\frac{\partial_{\theta_0} p(\theta_0, r)\sqrt{r}}{m_p n\partial_{\theta_0}\theta(\theta_0, r) r_{\rm g}}. \quad (9)$$

Substituting the number density from relation (8) yields

$$\partial_r\left[r^{3/2}\partial_r\theta(\theta_0, r)\right] \quad (10)$$
$$= -\sqrt{r_0}\frac{{c_0}^2}{r_{\rm g}}\left(\frac{r}{r_0}\right)^{\frac{3}{2}\left(\frac{4}{3}-\Gamma\right)}$$
$$\times\frac{\left[\frac{\sin\theta(\theta_0, r)}{\sin\theta_0}\partial_{\theta_0}\theta(\theta_0, r)\right]^{2-\Gamma}}{(\partial_{\theta_0}\theta(\theta_0, r))}$$
$$\times\partial_{\theta_0}\left(\frac{\sin\theta_0}{\sin\theta(\theta_0, r)}\frac{1}{\partial_{\theta_0}\theta(\theta_0, r)}\right).$$

This expression can be written in convenient dimensionless coordinates. Let us denote

$$x = \frac{c_*^2 r}{4r_{\rm g}}.$$

Then, $x_* = 1$ and $x_0 = (r_0/r_*)$. As a result, Eq. (10) takes the form

$$\partial_x\left[x^{3/2}\partial_x\theta(\theta_0, x)\right] = -4\left(\frac{x}{x_0}\right)^{\frac{3}{2}\left(\frac{4}{3}-\Gamma\right)}$$
$$\times\frac{\left[\frac{\sin\theta(\theta_0, x)}{\sin\theta_0}\partial_{\theta_0}\theta(\theta_0, x)\right]^{2-\Gamma}}{(\partial_{\theta_0}\theta(\theta_0, x))}$$
$$\times\partial_{\theta_0}\left(\frac{\sin\theta_0}{\sin\theta(\theta_0, x)}\frac{1}{\partial_{\theta_0}\theta(\theta_0, x)}\right).$$

We have derived a second-order hyperbolic partial differential equation that is linear in two derivatives. Let us transform it to a system of ordinary differential equations. For this purpose, we use assumption (2) and substitute θ with a finite sum containing the

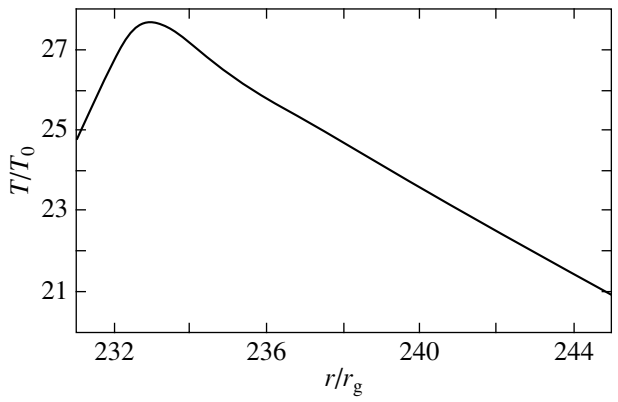

Fig. 1. Temperature ratio along the $\theta = 0$ axis versus r/r_g near the peculiarity for the parameters $\Gamma = 7/5, \varepsilon = 0.03, c_\infty = 0.00001$; T_0 corresponds to Bondi (1952) accretion.

terms with the powers of θ_0 up to $2N+1$:

$$\theta(\theta_0, r) = \sum_{n=0}^{N} {\theta_0}^{2n+1} k_{2n+1}(r). \qquad (11)$$

We know the function $\theta(\theta_0, r)$ (5) at the radius r_0. This defines the initial conditions for (9). Then,

$$k_1(r_0) = 1, \quad k_{2n+1}(r_0) = 0, \qquad (12)$$
$$n = 1, 2, \ldots, N.$$

$${k'}_{2n+1}(r_0) = (-1)^n \frac{\varepsilon k_{\rm in}}{2(2n+1)! r_0} \sqrt{\frac{r_*}{r_0}}, \qquad (13)$$
$$n = 0, 1, \ldots, N.$$

The Cauchy problem is Eq. (10) with the initial conditions (12) and (13). After substituting (11), we obtain a system for $N+1$ functions of the radius. The absence of terms with even powers can be explained by the zero initial conditions for them, while the equation to be solved is homogeneous.

The apparent complexity of the method of solution described above can be easily explained when it is considered that we must separate out a region of a very small size in both $\theta \ll 1$ and r when solving the second-order partial differential equation.

Qualitatively, the behavior of the trajectories can be described as follows. A plane uniform flow at infinity initially transforms into an almost spherically symmetric flow near the sonic surface. Subsequently, depending on the adiabatic index, three cases are possible (Beskin and Pidoprygora 1995):

(1) For $\Gamma \to 5/3$, the Mach number M, which defines the ratio of the gravitational forces to the pressure force, does not tend to infinity, but retains a value of the order of unity as r tends to zero. It can be no significant additional compression compared to that in the spherically symmetric case.

(2) For $\Gamma < 1.25$, $k_{\rm in}(\Gamma)$ is negative at positive $K(\Gamma)$ (onflow along the $\theta = \pi$ axis); therefore, the streamlines converge on the rear side (as can be seen from (1)).

(3) For $\Gamma > 1.25$, the sign of the coefficient $k_{\rm in}$ is opposite; the streamlines converge on the front side of the object. After the passage of the region of maximum streamline convergence near the symmetry axis, the pressure pushes them apart.

Thus, our region is described by the following quantities: the radius r_x at which there is maximum additional compression on the axis compared to that in Bondi accretion; the dimensionless radius x_x by definition (10); the radial size of the region Δr at the boundary of which the additional compression decreases by a factor of 2; the caustic radius at the same parameters, but without including the pressure $R_{\rm ball}$; the minimum achievable ratio θ/θ_0 in this region k_x; and the minimum Mach number M_x in the vicinity of r_x.

Let us make a calculation for two cases: $\Gamma = 4/3$, $c_\infty = 0.0002$ and $\Gamma = 7/5$, $c_\infty = 0.00001$. The first case is nonphysical. It has only a theoretical significance as an extension of classical astrophysical problems. In turn, the sonic surface can be passed in dense clouds of molecular hydrogen under conditions corresponding to the second case. The characteristic radial size of the region is $\Delta r \approx r_x/5$. The solution is stable for $r > r_x$; i.e., the result does not change with increasing N. Further out, the algorithm is unstable; therefore, the behavior of the solution cannot be determined at small $r \ll r_x$.

Let $k(r) = k_1(r)$, accordingly, $k_x = k(r_x)$. Let us estimate the physical parameters of the system on the axis. First, the number density can be written as

$$n(0, r) = n_0 \left(\frac{r_0}{r}\right)^{3/2} k(r)^{-2},$$

which yields

$$M = \frac{v}{c_s} \sim \frac{1}{\sqrt{T}\sqrt{r}} \sim \frac{n^{(1-\Gamma)/2}}{\sqrt{r}} \sim r^{(3\Gamma-5)/4} k^{\Gamma-1}$$

for the Mach number. Thus, $M(0, r) = (r_{kr}/r)^{(5-3\Gamma)/4} k(r)^{\Gamma-1}$ and

$$M_x \approx \left(\frac{R_{\rm ball}}{r_x}\right)^{(5-3\Gamma)/4} (\varepsilon k_{\rm in})^{(3\Gamma-5)/2} {k_x}^{\Gamma-1}.$$

We have $k_{\rm in} = 0.025$ for $\Gamma = 4/3$ and $k_{\rm in} = 0.026$ for $\Gamma = 7/5$ (Beskin and Pidoprygora 1995). In fact, the parameter of smallness for $\Phi^{(1)}$ is $\varepsilon k_{\rm in}$ rather than ε, which is of the order of 0.1–1.

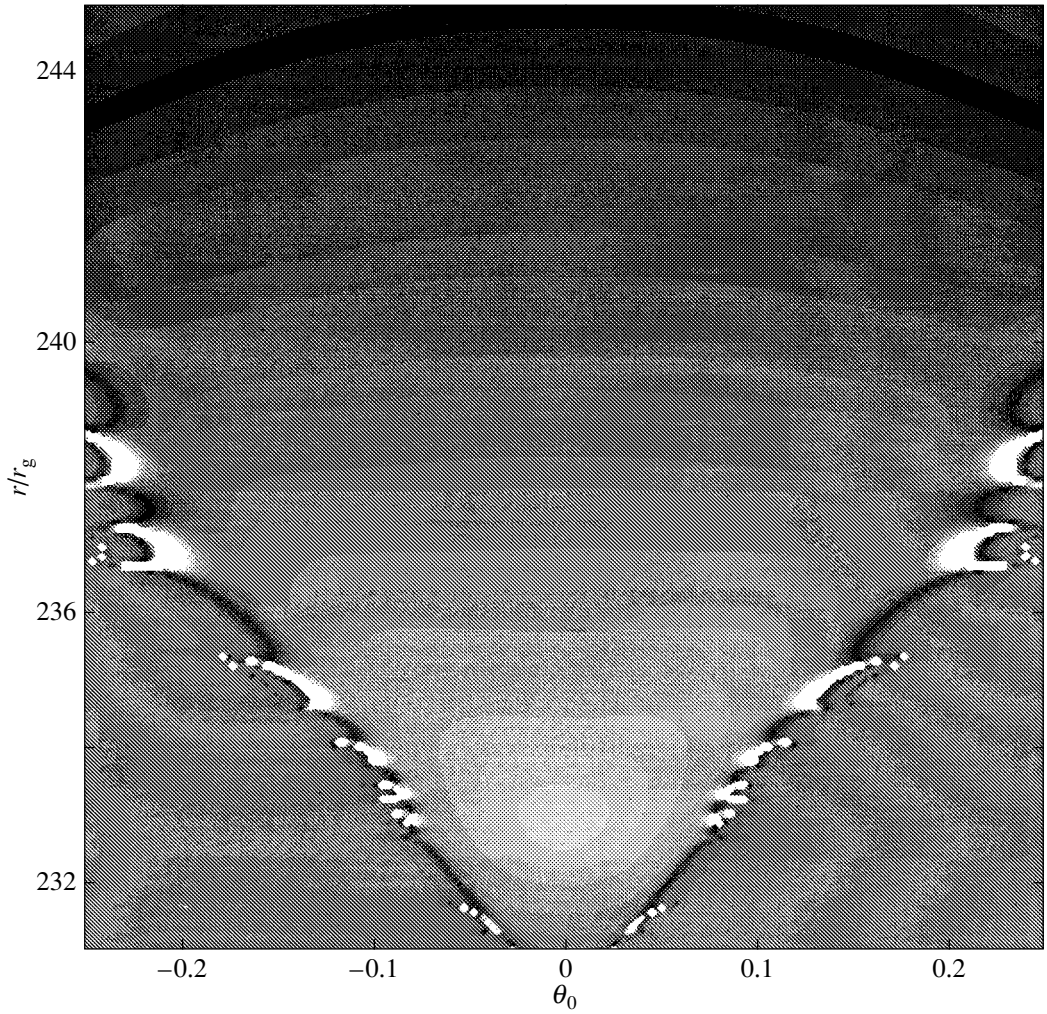

Fig. 2. Temperature versus coordinates in the plane of variables $(r/r_g, \theta_0)$ for the parameters $\Gamma = 7/5, \varepsilon = 0.03, c_\infty = 0.00001$. The light area at the center has the highest temperature.

Figure 1 shows the dependence of the ratio of the temperatures in our case and the spherically symmetric case on the dimensionless distance to a compact object calculated for the above parameters.

Figure 2 shows the corresponding bivariate dependence of the temperature on the dimensionless distance and the angle θ_0. The transformation to the $(r/r_g, \theta)$ plane near r_x was made by a factor of $1/k_x$ compression along the symmetry axis of the system. The light spots in the lower corners of the figure have no physical meaning, but are due to the divergence of the algorithm. Using Fig. 1, we can associate the brightness in Fig. 2 with temperature.

VALIDITY OF THE ASSUMPTIONS

To solve the problem, we made many assumptions. Let us substantiate them.

For our estimates, we set $c_\infty = 0.0002$.

(1) In most cases, the needed region is located far from the event horizon of the object, $r \gg r_g$, which allows the metric to be considered flat.

(2) The inclination of the streamline α to the radial vector is at a maximum precisely near r_x. The solution for $n(r)$ yields $\Delta r \approx 5 \times 10^5$ cm, $r_x \approx 10^7$ cm, and $k_x \approx 0.03$. The region is compressed almost identically to $\theta_0 < 0.3$, whence we can estimate $\alpha \approx \theta_0 k_x r_x / \Delta r \approx 0.2$; this is the maximum possible value of α.

(3) To substantiate the possibility of ignoring the enthalpy of matter compared to the gravitational energy, we calculated the Mach number M. The ratio of the enthalpy to the kinetic energy for a nonrelativistic gas is $2c_s^2/v^2(\Gamma - 1) = 2/M^2(\Gamma - 1)$, reaching unity at r_x. However, this is true in a small region. This effect can be easily estimated by solving the equations with the effective increased coefficient of the term

responsible for the pressure. When the coefficient increases by a factor of 1.5, r_x decreases by approximately the same factor (1.5), while k_x increases by no more than 10%.

(4) The smallness of ${\theta_0}^{25}k_{25}(r_x)$ compared to $\theta_0 k_1(r_x)$ corresponds to $\theta_0 < 0.3$ at $r = r_x = 2.85 \times 10^7$, which corresponds to an area fraction of 0.036 of the initial one at r_0. This implies that much (>1/30) of the flow is subjected to strong compression. At a large radius, i.e., larger than r_x, each succeeding term $\theta^{2n+1}r_{2n+1}$ is much smaller than the preceding term, while this is not the case for $r < r_x$. This is most likely because the convergence is lost in the method of solution used.

(5) Note also that the result does not depend on the chosen r_0. Let us make a check for $\varepsilon = 0.58$ and $\Gamma = 7/5$: when r_0 doubles, k_x decreases by 10% and r_x decreases by 20%. The difference stems from the fact that the flow becomes slightly compressed while moving from the sonic surface to r_0 and, most importantly, its direction slightly changes. For smaller ε, the r_0 dependence of the parameters of the region is even weaker.

Note that the satisfactory accuracy of the results cannot be improved significantly by abandoning the assumptions and performing more accurate calculations. First, we used the first approximation for our calculations with a finite ε, and, second, we used its form at small radii where the first approximation grows compared to the zeroth solution. We cannot specify any initial conditions near the sonic surface, since the behavior of formula (4) is asymptotic for $r \to 0$.

To make progress in this field requires numerically solving an exact system of two nonlinear partial differential equations, one first-order equation and one second-order equation. In this case, we must reveal features that are many orders of magnitude smaller than the outer radius of integration or even the sonic surface, which can be achieved only by using adaptive methods with a variable step. In addition, we must numerically calculate the parameters of the separatrix surface (the boundary of the causally connected region) in the case where its smooth passage is realized, solve the time-dependent problem of establishment of this regime, show that it will be stable, and find the percentage of cases in which accretion without shocks will be realized. Such calculations are far beyond the scope of this paper.

PHYSICAL AND OBSERVATIONAL SIGNIFICANCE OF THE RESULT

Noteworthy among the peculiarities of an axisymmetric flow on a compact object observed so far is the tail convergence of streamlines behind a moving object during accretion in a region of cold dense dust where star formation takes place.

The effect discussed in this paper has not yet been observed. The parameter $\Gamma = 7/5$ has a very narrow validity range. For example, it is realized at the initial stage of accretion onto a compact object from dense clouds of molecular hydrogen until its dissociation (the equations with a constant Γ cannot be used at all when the dissociation is included).

Let us consider in more detail the accretion of a hot gas from H II regions. $\Gamma = 5/3$ far from a massive object. The value of Γ is the same on the sonic surface, since the gas density and temperature at infinity and on the sonic surface differ by a small factor (Garlick 1979). In this case, the angular momentum of the gas relative to the stellar center is very low in a stable regime. Although the electrons become relativistic and the adiabatic index decreases sharply to $\Gamma = 13/9$ starting from a certain distance (Shapiro and Teukolsky 1983), no region of anomalous compression is formed in this case.

Nevertheless, let us calculate the energy release in the region of streamline convergence for nonphysical constant values of $\Gamma < 5/3$. The calculation will yield an upper limit for actual astrophysical objects. For our estimate, we assume that all of the observed radiation in the derived temperature range is only thermal bremsstrahlung (Shapiro 1973). Its intensity per unit volume is defined by the nonrelativistic formula $\Lambda = cn^2T^{1/2}$ with the coefficient c that depends weakly on the number density n and temperature T. The intensity of the radiation for spherically symmetric accretion is then

$$L_0 = \int \Lambda d^3r = \frac{16\pi}{3(\Gamma-1)} C n_x^{(\Gamma+3)/2} \times \left(\frac{r_x}{r_g}\right)^{3/4(\Gamma+3)} {r_g}^3,$$

where n_x corresponds to Bondi accretion. The characteristic radial size of the region in our case is $\Delta r \approx r_x/5$, and the tangential size is $r_\perp \approx r_x\theta_x k_x$, where θ_x defines the maximum angle at the radius r_0 at which the streamlines are still compressed by a factor of $1/k_x$. The released energy L_x in our region is

$$L_x \approx \Lambda_x \Delta r \pi r_\perp^2 = C n_x^{(\Gamma+3)/2} \pi \theta_x^2 k_x^{-1-\Gamma} r_x^3/5.$$

For our estimate, we set $\theta_x = 0.5$. The ratio of the released energies can then be written as

$$\frac{L_x}{L_0} = \frac{3(\Gamma-1)}{320} k_x^{-1-\Gamma} \left(\frac{r_x}{r_g}\right)^{3/4(1-\Gamma)}. \qquad (14)$$

It follows from (14) and from the table that the ratio of the released energies increases as the radius at which the streamlines focuse decreases. Let us

Table

ε	x_x	k_x	$R_{\rm ball}/r_x$	M_x	$r_x/r_{\rm g}$	ε	x_x	k_x	$R_{\rm ball}/r_x$	M_x	$r_x/r_{\rm g}$
$\Gamma = 4/3, c_\infty = 0.0002$						$\Gamma = 7/5, c_\infty = 0.00001$					
1	2.5×10^{-4}	0.036	2.5	2.5	7.8×10^2	1	1.6×10^{-4}	0.068	4.1	2.0	1.6×10^5
0.64	1.1×10^{-4}	0.029	2.3	2.9	3.6×10^2	0.38	2.7×10^{-5}	0.044	3.7	2.3	2.7×10^4
0.4	4.8×10^{-5}	0.023	2.1	3.4	1.5×10^2	0.15	5.2×10^{-6}	0.031	3.1	2.8	5.2×10^3
0.24	1.9×10^{-5}	0.017	1.9	4	59	0.06	8×10^{-7}	0.021	2.8	3.5	8×10^2
0.16	8.9×10^{-6}	0.014	1.8	4.5	28	0.03	2×10^{-7}	0.016	2.6	4.1	2.3×10^2
0.10	3.5×10^{-6}	0.011	1.8	5.3	11	0.013	5×10^{-8}	0.011	2.5	4.9	46
0.06	1.3×10^{-6}	0.008	1.7	6.1	4	0.006	1×10^{-8}	0.008	2.4	5.8	10

calculate it for the minimum possible ε at which the focusing still takes place. We take the lower rows of the tables of parameters describing the region of anomalous compression with $\Gamma = 4/3$ and $\Gamma = 7/5$. We find from (14) that L_x/L_0 reaches 100; i.e., when the focusing is present, the Bondi–Hoyle accretion efficiency can increase by up to a factor of 10^2. For a physically meaningful value of $\Gamma = 7/5$, the calculated ratio (14) actually specifies only an upper limit for L_x/L_0, since the gas dissociates rapidly and is subsequently ionized as it heats up, which ensures a transition to the regime with $\Gamma = 5/3$ and is accompanied by a significant decrease in L_x. However, the proper allowance for the change in adiabatic index in the axisymmetric case is beyond the scope of this paper. Although the velocity dispersion of compact objects is much higher than the speed of sound in the surrounding cloud of gas and dust, the described regime with $\varepsilon < 1$ can take place in certain cases at a low relative velocity of the gas cloud and the compact object. Such a change in energy release and accretion spectrum must be taken into account when analyzing experimental data to estimate the parameters of the black hole itself moving in regions of gas compression and its surrounding medium.

ACKNOWLEDGMENTS

I wish to thank Prof. V.S. Beskin, my scientific adviser, for fruitful discussions. This work was supported in part by the Russian Foundation for Basic Research (project no. 05-02-17700).

REFERENCES

1. V. S. Beskin and Yu. N. Pidoprygora, Zh. Éksp. Teor. Fiz. **107**, 1025 (1995) [JETP **80**, 575 (1995)].
2. H. Bondi, Mon. Not. R. Astron. Soc. **112**, 195 (1952).
3. H. Bondi and F. Hoyle, Mon. Not. R. Astron. Soc. **104**, 273 (1944).
4. A. R. Garlick, Astron. Astrophys. **73**, 171 (1979).
5. S. L. Shapiro, Astrophys. J. **180**, 531 (1973).
6. S. L. Shapiro and S. A. Teukolsky, *Black Holes, White Dwarfs, and Neutron Stars: The Physics of Compact Objects* (Wiley, New York, 1983; Mir, Moscow, 1985).

Translated by V. Astakhov

Astronomy Letters, Vol. 31, No. 9, 2005, pp. 598–611. Translated from Pis'ma v Astronomicheskiĭ Zhurnal, Vol. 31, No. 9, 2005, pp. 669–683.

Infrared Photometry for Five Close Binary Systems

O. G. Taranova* **and V. I. Shenavrin**

Sternberg Astronomical Institute, Universitetskiĭ pr. 13, Moscow, 119992 Russia

Received March 17, 2005

Abstract—We present the $JHKLM$ photometry for five close (W Ser) binary systems obtained in the period 1996–2004. Positive phase shifts (with respect of the adopted ephemerides) have been found in the orbital infrared light curves for three binaries, RX Cas, KX And, and β Lyr; the rates of increase in their periods are $\sim 3.5 \times 10^{-4}$, $\sim 1.6 \times 10^{-3}$, and $\sim 1.4 \times 10^{-4}$ days yr^{-1}, respectively. We have performed the spectral classification of the components of the binaries under study and estimated their parameters.

Key words: *stars—variable and peculiar, close binary systems.*

INTRODUCTION

W Ser binaries constitute a small group of strongly interacting binary systems that includes the binary W Ser itself, RX Cas, V367 Cyg, etc. These are believed to go through a short evolutionary phase of rapid mass transfer. The salient feature of these systems is the existence of circumstellar envelopes whose radiation in emission lines clearly shows up in the optical and ultraviolet wavelength ranges. W Ser binaries seem the natural progenitors of classical symbiotic stars and a continuation of Algols, but with shorter and longer orbital periods in the former and latter cases, respectively.

Near-infrared studies of these systems allow the parameters of their secondary components, which are generally cooler than the primary components, and the gas and dust envelopes in which both stellar components are embedded to be estimated.

At present, we are performing $JHKLM$ photometry for three W Ser binaries (RX Cas, V367 Cyg, and β Lyr). This list was supplemented by two peculiar emission-line binaries, KX And and V360 Lac. Stefl *et al.* (1990) classified the former as a strongly interacting binary with a high probability; Hill *et al.* (1997) tentatively classified the latter as a semidetached system at the phase of mass transfer between the components.

We began our observations of W Ser binaries in 1981; the results of observations obtained prior to 1996 were analyzed mainly in papers by Taranova (1987, 1997) and Taranova and Shenavrin (1997). In this paper, we analyze the results of our $JHKLM$ photometry for the above stars obtained in the period 1996–2004.

*E-mail: taranova@sai.msu.ru

OBSERVATIONS

Our photometry of all program stars in the standard $JHKLM$ system is performed using a photometer with an indium-antimonide (InSb) detector cooled with liquid nitrogen. The photometer is mounted at the Cassegrain focus of a 1.25-m telescope at the Crimean Station of the Sternberg Astronomical Institute; the exit aperture is $\sim 12''$. The photometric standards were stars from the catalog by Johnson (1966): BS 8860 (for KX And), BS 8632 (for RX Cas), BS 7949 (for V367 Cyg), and BS 7178 (for β Lyr). When necessary, we estimated the HLM magnitudes of the standards from their spectral types using relations from Koornneef (1983). In general, the photometric error of a single measurement for stellar photometry did not exceed a few hundredths of a magnitude.

General information about the stars studied here is given in Table 1. Its columns list sequentially the spectral types of the binary components (Kholopov *et al.* 1985), the orbital variability periods, the epochs of primary minima, the color excesses $E(B-V)$, and the distances to the systems r. The last column gives references to the papers from which $E(B-V)$ and r were taken.

The results of our $JHKLM$ photometry obtained in the period1996–2004 are summarized in Table 2.

Table 3 lists the mean $JHKLM$ magnitudes (with their standard deviations) for the program binaries at orbital phases near the primary and secondary minima and near maximum light. For the binary RX Cas, Table 3 also gives its mean $UBVR$ magnitudes calculated using our optical observations of RX Cas (Taranova and Shenavrin 1997).

1063-7737/05/3109-0598$26.00

Table 1. General parameters of the program objects

Object	Sp	P, days	Epoch of primary minimum, JD 2400000+	r, pc	$E(B-V)$	References
KX And	B3pe+K1 III	38.957	42 675.2	700	0.16	Guinan *et al.* (1984)
RX Cas	K1 III+A5eIII	32.33010	46 827.389	600	0.43	Martynov *et al.* (1980)
V367 Cyg	B8peIa+F4 III	18.59773	37 390.855	800	0.85	Akan (1987)
V360 Lac	B3 IVeav	10.085408	41 170.285	650	0.26	Hill *et al.* (1997)
β Lyr	B8II-IIIep	12.935	50 001.035	270	0.13	Phillips *et al.* (1980)

ORBITAL INFRARED BRIGHTNESS AND COLOR VARIATIONS OF THE BINARIES

RX Cas. This is the first W Ser binary for which we began to perform JHK photometry in 1981. References to our papers in which we analyzed the results of the binary's observations before 1996 are given in Taranova and Shenavrin (1997).

The system consists of a cool component (a G or K giant) and a hot source surrounded by a dense envelope. The binary's orbital period is ~32.33 days (Table 1). It was firmly established that the period of this binary increases (see, e.g., Kriz *et al.* 1980; Andersen *et al.* 1989; Oh Kyu-Dong 1991). In particular, Kriz *et al.* (1980) found that $\Delta P/P$ is $\sim 6.3 \times 10^{-7}$ and that the rate of mass transfer between the components exceeds $10^{-6}\ M_\odot\ \mathrm{yr}^{-1}$. In addition to the orbital period, RX Cas exhibits the brightness variations attributable to the physical variability of one of the binary components. The period of these variations is about 516 days (Kalv 1979).

Figure 1 shows the brightness and color variations of RX Cas with orbital phase. The phases were computed with the elements Min I = JD 2446827.389 + 32.3301E (Andersen *et al.* 1989). A phase shift of the light curves by about 0.02 with respect to the ephemeris of 1987 is clearly seen in Fig. 1. It would be natural to associate this shift with a change in the orbital period, which is $P_1 = 32.3351 \pm 0.0005$ days for the epoch of our observations, and, hence, the rate of increase in the period over the past ten years was about 3.5×10^{-4} days yr^{-1}, or 30 s yr^{-1}. For the components' masses of 0.5 $M_\odot$ and 5 $M_\odot$ (Taranova 1987), the mass transfer rate between the components is $\sim 2 \times 10^{-6}\ M_\odot\ \mathrm{yr}^{-1}$.

Analysis of the optical and infrared orbital brightness variations of RX Cas shows that only one minimum, near phase 0.0, is observed in the U and B brightness variations; the secondary minimum is almost unseen, and, hence, the cool component does not contribute noticeably to the total light from the binary components in the range 0.35–0.45 μm. The contribution from the cool component increases with wavelength, and both minima are seen even at a wavelength of 0.55 μm, the minima have the same depth near 1 μm, and the secondary minimum is deeper than the primary one at longer wavelengths (Fig. 1). The latter feature of the orbital light curve was analyzed in detail by Taranova (1987). Figure 1, which shows the J, M, V brightness variations and $J-K$, $U-B$ color variations (Taranova and Shenavrin, 1997), illustrates the above peculiarities of the brightness and color variations in RX Cas with orbital phase. The mean $J-K$ color index is 0.857 ± 0.003, and it may increase by two or three hundredths of a magnitude only near the primary minimum (Fig. 1). This implies that, in contrast to the range 0.36–0.45 μm, where the radiation from the cool component is almost unseen, in the range 1.25–5 μm the system's cool component mainly emits radiation.

KX And. Based on infrared spectra of the bright Be star KX And (=HD 218393), Polidan (1976) and Floquet *et al.* (1989, 1995) detected the secondary component in the system, a K(0–1) giant. Analyzing the spectral energy distribution (SED) for KX And up to 60 μm, they found the SED to be fitted best by the combined light from two B2III and K0II stars. Our scarce infrared observations of the binary in the period 1989–1996 (Taranova 1997) confirmed the existence of a K giant in the system. We continued our $JHKLM$ photometry of the binary in the period 1996–2002 (Table 2).

Figure 2 shows the J brightness and $J-K$ color variations with orbital phase for KX And. The phases were computed with the elements derived by Stefl *et al.* (1990) from the star's U brightness variations: JD = 2442675.26 + 38.957E.

The solid curve in this figure indicates a ninth-order approximation of the observed J brightness variations. It can be concluded from Fig. 2 that, on average, the observed infrared brightness variations of KX And have the same period as the U brightness variations, although the epochs of minima in the infrared light curves (the vertical dashed lines) are shifted in phase by about 0.2. The amplitudes of the

Table 2. $JHKLM$ photometry for the five close binary systems, 1996–2004

JD 2400000+	J	H	K	L	M	$\sigma(M)$	JD 2400000+	J	H	K	L	M	$\sigma(M)$
KX And							RX Cas						
50361.446	5.88	5.39	5.26	5	4.88	0.11	51452.487	6.6	5.88	5.72	5.48	5.86	0.13
50362.446	5.88	5.39	5.26	5	4.88	0.11	51453.465	6.46	5.79	5.58	5.36	5.5	0.06
51033.564	5.84	5.4	5.16	5.01			51454.476	6.4		5.56	5.31	5.41	0.08
51060.509	5.83	5.3	5.13	4.97			51455.535	6.39	5.72	5.57	5.28	5.58	0.07
51069.516	5.77	5.28	5.1	4.94	4.94	0.08	51475.52	6.31	5.64	5.48	5.22	5.43	0.05
51088.454	5.75	5.31	5.11	4.95	5.03	0.06	51502.403	6.66	5.99	5.8	5.58	5.76	0.08
51095.422	5.81	5.37	5.15	5.02	5.16	0.07	51504.415	6.46	5.79	5.62	5.38	5.55	0.05
51128.343	5.77	5.32	5.16	5.03	5.17	0.05	51525.332	6.28	5.59	5.4	5.18	5.32	0.08
51152.268	5.83	5.36	5.19	5.02	5.06	0.06	51526.424	6.34	5.69	5.5	5.21	5.39	0.09
51184.187	5.7	5.29	5.06	4.93	5.09	0.05	51532.397	6.89	6.26	6.06	5.78	6.08	0.09
51385.557	5.83	5.4	5.18	5.01	5.07	0.03	51548.248	6.7	5.99	5.84	5.65	5.68	0.07
51420.501	5.74	5.33	5.08	4.94	5.08	0.04	51581.234	6.71	6	5.84	5.6	5.89	0.08
51446.471	5.78	5.35	5.13	4.99	5.19	0.09	51779.557	6.4	5.73	5.54	5.29	5.48	0.1
51448.427	5.83	5.38	5.22	5.06	5.16	0.07	51824.544	6.77	6.13	5.94	5.68	5.95	0.08
51449.451	5.86	5.4	5.2	5.02	5.14	0.06	51831.489	6.34	5.66	5.48	5.23	5.46	0.06
51450.431	5.84	5.37	5.18	5.05	5.1	0.08	51832.494	6.27	5.66	5.47	5.19	5.36	0.07
51451.461	5.82	5.35	5.19	4.94	5.16	0.05	51833.497	6.35	5.68	5.54	5.31	5.34	0.08
51452.4	5.81	5.34	5.14	4.99	4.97	0.03	51834.458	6.36	5.68	5.52	5.29	5.48	0.07
51453.385	5.79	5.29	5.14	5.03	4.95	0.07	51848.465	6.32	5.63	5.47	5.23	5.47	0.06
51454.407	5.74	5.36	5.11	4.94	5.09	0.04	51850.427	6.4	5.77	5.58	5.32	5.48	0.07
51455.414	5.71	5.29	5.09	5.08	4.94	0.04	51853.416	6.66	5.99	5.81	5.51	5.61	0.07
51475.381	5.79	5.32	5.12	5	5.13	0.05	51862.388	6.34	5.64	5.49	5.24	5.35	0.05
51520.274	5.8	5.36	5.15	4.98	5.12	0.04	51863.375	6.33	5.68	5.51	5.25	5.51	0.07
51548.191	5.73	5.3	5.12	4.95	5	0.03	51864.346	6.33	5.68	5.52	5.28	5.54	0.07
51552.21	5.76	5.34	5.14	4.95	5.06	0.02	51865.312	6.33	5.68	5.48	5.24	5.58	0.07
51775.525	5.83	5.4	5.21	5	4.8	0.2	51866.355	6.35	5.68	5.5	5.26	5.55	0.08
51779.511	5.86	5.41	5.23	5.03	5.3	0.14	51867.346	6.41	5.72	5.54	5.28	5.5	0.05
51802.463	5.76	5.34	5.14	4.94	5.06	0.04	51868.399	6.44	5.75	5.57	5.32	5.54	0.05
51824.399	5.81	5.36	5.12	4.93			51888.328	6.84	6.15	5.98	5.68	6.06	0.1
51831.421	5.77	5.28	5.15	4.95	5.05	0.04	51901.365	6.42	5.74	5.58	5.32	5.65	0.06
51832.41	5.77	5.3	5.14	4.97	5.03	0.04	51902.252	6.53	5.83	5.66	5.43	5.68	0.05
51833.404	5.72	5.3	5.08	4.95	5.03	0.04	51917.343	6.56	5.91	5.71	5.48	5.69	0.07
51834.386	5.76	5.31	5.13	4.95	4.96	0.05	51918.251	6.73	6.08	5.91	5.59	5.71	0.08
51848.347	5.75	5.3	5.1	4.92	5.03	0.04	51926.226	6.41	5.76	5.56	5.29	5.55	0.04
51853.355	5.85	5.4	5.2	5.02	5.06	0.06	51927.314	6.39	5.7	5.52	5.29	5.49	0.06
51862.327	5.79	5.35	5.16	4.95	5.06	0.03	51934.214	6.51	5.84	5.66	5.41	5.69	0.06
51864.291	5.78	5.33	5.15	4.96	5.06	0.04	51935.197	6.62	5.93	5.76	5.52	5.77	0.07
51866.327	5.78	5.32	5.15	4.97	5.03	0.03	51948.192	6.46	5.81	5.63	5.38	5.5	0.06
51867.302	5.76	5.31	5.11	4.91	4.99	0.04	51950.198	6.69	6.03	5.84	5.58	5.79	0.07
51868.338	5.74	5.32	5.13	4.94	5.06	0.04	51951.237	6.87	6.21	6.02	5.75	5.82	0.07
51888.257	5.69	5.26	5.1	4.91			51976.219	6.35	5.67	5.52	5.3		
51888.257	5.67	5.22	5.04	4.87	5	0.03	52187.519	6.3	5.64	5.45	5.27	5.63	0.16
51902.174	5.73	5.28	5.09	4.91	4.97	0.03	52191.451	6.39	5.71	5.5	5.28	5.53	0.07
51917.224	5.75	5.31	5.11	4.94	5.08	0.03	52192.465	6.45	5.79	5.64	5.34	5.61	0.04
52129.541	5.84	5.42	5.22	5.01	5.16	0.05							
52154.507	5.72	5.31	5.14	4.96	4.96	0.04							
53284.431	5.79	5.38	5.19	4.96	4.96	0.05							

Table 2. (Contd.)

JD 2400000+	J	H	K	L	M	$\sigma(M)$	JD 2400000+	J	H	K	L	M	$\sigma(M)$
V360 Lac							V367 Cyg						
50853.1730	5.74	5.44	5.33				50753.327	5.82	5.52	5.36	5.04	4.72	0.06
50859.1770	5.49	5.31	5.24				50764.88	5.53	5.19	5	4.7	4.53	0.04
51010.5370	5.6	5.4	5.27	5.2	5.07	0.08	50777.331	5.37	5.03	4.85	4.51	4.22	0.04
51033.4920	5.68	5.48	5.41	5.33			50793.165	5.38	5.05	4.88	4.58	4.33	0.04
51036.5110	5.51	5.36	5.27	5.17	5.37	0.1	51008.53	5.26	4.92	4.76	4.47	4.24	0.06
51038.4880	5.56	5.44	5.34	5.24	5.13	0.08	51009.537	5.29	4.97	4.77	4.48	4.32	0.06
51059.5140	5.6	5.46	5.34	5.24	5.64	0.24	51010.509	5.35	5.02	4.83	4.53	4.28	0.06
51067.4700	5.54	5.38	5.27	5.22	5.2	0.22	51033.459	5.57	5.25	5.09	4.77	4.56	0.28
51088.3950	5.6	5.44	5.34	5.24	5.37	0.09	51037.413	5.3	4.97	4.78	4.48	4.28	0.07
51095.3830	5.6	5.44	5.33	5.26	5.25	0.1	51039.444	5.49	5.12	4.92	4.63	4.4	0.09
51121.3650	5.56	5.4	5.29	5.22	5.42	0.14	51060.399	5.93	5.45	5.33	4.98	4.52	0.1
51128.3840	5.57	5.42	5.32	5.26	5.33	0.09	51062.423	5.43	5.08	4.9	4.57	4.59	0.09
51180.1810	5.58	5.44	5.35	5.29	5.2	0.06	51065.372	5.33	4.96	4.78	4.47	4.25	0.07
51205.1670	5.63	5.52	5.38	5.32	5.27	0.12	51067.345	5.46	5.11	4.93	4.61	4.24	0.09
51384.5470	5.57	5.39	5.3	5.21	5.24	0.05	51069.406	5.75	5.42	5.28	4.99	4.58	0.11
51420.4740	5.58	5.39	5.28	5.17	5.2	0.05	51383.509	5.46	5.11	4.96	4.6	4.34	0.03
51446.4480	5.62	5.43	5.38	5.31	5.42	0.05	51384.496	5.58	5.25	5.1	4.73	4.51	0.03
51454.3750	5.51	5.36	5.25	5.19	5.11	0.08	51385.475	5.75	5.46	5.28	4.95	4.7	0.02
51455.3740	5.56	5.38	5.3	5.19	5.3	0.08	51387.479	5.45	5.14	4.96	4.65	4.29	0.05
51475.3420	5.55	5.4	5.3	5.21	5.24	0.05	51421.448	5.49	5.19	4.98	4.64	4.36	0.04
51524.2140	5.61	5.47	5.36	5.24	5.32	0.05	51448.389	5.42	5.06	4.89	4.53	4.25	0.04
51552.1790	5.62	5.48	5.38	5.28	5.17	0.04	51451.374	5.78	5.41	5.18	4.8	4.63	0.04
51774.5420	5.63	5.48	5.38	5.26	5.06	0.24	51452.373	5.54	5.2	5.02	4.76	4.45	0.03
51778.5210	5.63	5.44	5.36	5.31	5.4	0.14	51453.352	5.33	5.05	4.89	4.55	4.18	0.04
51802.4250	5.58	5.44	5.35	5.23	5.37	0.06	51454.343	5.31	4.93	4.79	4.49	4.25	0.03
51824.3680	5.68	5.5	5.42	5.32			51455.35	5.33	4.98	4.78	4.49	4.25	0.04
51831.3540	5.69	5.53	5.37	5.37			51456.331	5.4	5.03	4.78	4.46	4.18	0.05
51832.3350	5.61	5.43	5.33	5.26	5.22	0.03	51707.505	5.37	5.04	4.85	4.56	4.19	0.04
51833.3680	5.56	5.41	5.3	5.24	5.14	0.06	51708.546	5.44	5.1	4.92	4.58	4.32	0.05
51834.3190	5.62	5.46	5.37	5.27	5.18	0.04	51710.507	5.84	5.52	5.32	4.89	4.51	0.11
51853.3220	5.59	5.43	5.33	5.27	5.32	0.07	51711.538	5.82	5.46	5.25	4.9	4.54	0.05
51863.2550	5.59	5.42	5.33	5.25	5.17	0.05	51719.51	5.65	5.32	5.14	4.8	4.45	0.05
51866.3020	5.6	5.47	5.38	5.28	5.19	0.04	51737.537	5.56	5.21	5.02	4.71	4.45	0.04
51868.3100	5.55	5.41	5.32	5.23	5.24	0.06	51738.535	5.74	5.44	5.26	4.92	4.43	0.08
51917.1880	5.57	5.45	5.33	5.24	5.26	0.05	51741.53	5.44	5.12	4.95	4.67	4.38	0.03
52127.5680	5.67	5.51	5.46	5.32	5.31	0.08	51742.499	5.38	5.06	4.87	4.58	4.28	0.05
52153.4960	5.68	5.53	5.45	5.39	5.47	0.07	51774.506	5.48	5.15	4.98	4.67	4.57	0.17
V367 Cyg							51775.416	5.66	5.33	5.13	4.8	–	0.1
50361.327	5.53	5.29	5.1	4.91	4.81	0.13	51776.417	5.79	5.49	5.3	4.93	4.51	0.11
50362.327	5.53	5.29	5.1	4.91	4.81	0.13	51777.418	5.62	5.3	5.1	4.72	4.43	0.09
50625.47	5.47	5.1	4.95	4.63	4.36	0.06	51778.41	5.43	5.12	4.92	4.62	4.37	0.09
50699.412	5.49	5.15	4.98	4.68	4.35	0.03	51779.413	5.33	5.02	4.83	4.5	4.36	0.06
50700.394	5.43	5.09	4.92	4.55	4.35	0.03	51780.443	5.3	5	4.8	4.49	4.26	0.1
50702.423	5.41	5	4.83	4.5	4.34	0.04	51802.366	5.58	5.22	5.01	4.68	4.4	0.05
50704.388	5.47	5.15	4.98	4.64	4.39	0.05	51824.307	5.54	5.21	5.02	4.69		
50713.429	5.52	5.09	4.92	4.6	4.42	0.03	51831.291	5.71	5.4	5.18	4.85	4.52	0.05
50714.387	5.56	5.23	5.05	4.79	4.42	0.04	51832.271	5.8	5.5	5.33	4.99	4.68	0.05
50715.37		5.39	5.1	4.73	4.54	0.07	51833.312	5.6	5.28	5.1	4.78	4.47	0.04

Table 2. (Contd.)

JD 2400000+	J	H	K	L	M	$\sigma(M)$	JD 2400000+	J	H	K	L	M	$\sigma(M)$
V367 Cyg							β Lyr						
51834.272	5.46	5.14	4.92	4.62	4.34	0.03	52840.41	3.66	3.62	3.51	3.26	3.16	0.03
51835.285	5.4	5.16	4.97	4.65			52841.37	3.34	3.28	3.18	2.92	2.87	0.02
51848.257	5.43	5.11	4.92	4.6	4.27	0.03	52842.37	3.23	3.14	3.05	2.77	2.73	0.02
51853.297	5.43	5.1	4.92	4.61			52843.34	3.20	3.12	3.02	2.75	2.77	0.02
51863.231	5.28	4.93	4.75	4.45	4.24	0.03	52866.32	3.64	3.60	3.50	3.24	3.15	0.03
51864.217	5.22	4.9	4.71	4.39	4.08	0.03	52867.36	3.33	3.29	3.18	2.95	2.86	0.02
51865.285	5.29	4.96	4.78	4.43	4.24	0.04	52869.33	3.17	3.11	3.01	2.76	2.67	0.03
51866.224	5.38	5.05	4.85	4.5	4.23	0.04	52891.33	3.55	3.52	3.39	3.17	3.13	0.02
51867.239	5.43	5.12	4.93	4.58	4.22	0.03	52892.30	3.65	3.60	3.51	3.25	3.18	0.03
51868.263	5.62	5.29	5.11	4.78	4.5	0.05	53193.38	3.22	3.15	3.04	2.81	2.78	0.03
51902.151	5.31	4.97	4.77	4.49	4.25	0.02	53194.46	3.39	3.33	3.24	3.02	3.06	0.08
51903.154	5.39	5.04	4.85	4.52	4.28	0.03	53214.33	3.46	3.39	3.30	3.09	3.05	0.03
52125.485	5.4	5.06	4.85	4.52	4.38	0.03	53215.41	3.70	3.65	3.52	3.27	3.17	0.04
52127.48	5.49	5.17	5.02	4.66	4.44	0.04	53216.37	3.45	3.38	3.32	2.97	3.07	0.04
52131.434	5.54	5.2	5.04	4.71	4.37	0.03	53217.39	3.30	3.24	3.12	2.83	2.84	0.04
52153.431	5.36	5.04	4.84	4.53	4.33	0.04	53218.37	3.21	3.17	3.04	2.81	2.84	0.03
52154.444	5.4	5.08	4.88	4.56	4.35	0.04	53219.37	3.30	3.21	3.10	2.85	2.86	0.02
52158.388	5.73	5.36	5.15	4.8	4.56	0.03	53222.29	3.96	3.82	3.64	3.32	3.32	0.03
β Lyr							53223.36	3.44	3.35	3.24	2.98	3.00	0.03
52782.47	3.99		3.62	3.32	3.34	0.06	53224.38	3.25	3.18	3.08	2.82	2.81	0.02
52804.42	3.22	3.14	3.00	2.75	2.71	0.02	53225.33	3.30	3.22	3.12	2.86	2.87	0.02
52809.37	3.35	3.31	3.16	2.88	2.79	0.04	53226.31	3.32	3.29	3.15	2.90		
52832.39	3.46	3.39	3.27	3.02	2.96	0.04	53283.21	3.26	3.13	3.04	2.76	2.77	0.04
52834.37	3.68	3.60	3.47	3.16	3.10	0.03	53307.17	3.39	3.29	3.25	3.05	2.98	0.04
52836.41	3.23	3.17	3.06	2.78	2.72	0.02	53311.17	3.48	3.37	3.29	3.00	2.94	0.03
52839.44	3.50	3.46	3.34	3.07	3.08	0.03							

phase infrared brightness variations are $0^m.10 - 0^m.15$. The phase dependence in the $J - K$ color variations is also clearly seen from Fig. 2: the binary is slightly hotter at the secondary J brightness minimum.

If, as with other strongly interacting binaries (e.g., RX Cas), we associate the shift of the phase J light curve relative to the ephemeris used with a change in the orbital period, then the period at the epoch of primary minimum JD 2451449.451 (Table 2) was $P = 38.9964$ days. In other words, the period has increased over the past 25 years at a fairly high rate, no less than 1.6×10^{-3} days yr^{-1} or $\sim$140 s yr^{-1}. For the masses of the binary components of about 10 $M_\odot$, the rate of mass transfer between the components exceeds $\sim 6.8 \times 10^{-5}\ M_\odot$ yr^{-1}.

V360 Lac. Our list of observations of W Ser binaries includes the binary V360 Lac (HR 8690) with an orbital period of 10.075 days (Kholopov *et al.* 1985–1990). According to Hill *et al.* (1997), the stellar components of this system are similar in parameters to B3e and F9IV stars, with the secondary component (an F9IV star) probably filling its Roche lobe. These authors provided extensive data on the object, including those obtained by them from optical photometry and spectroscopy. The authors improved the orbital ephemeris and its elements Min I = HJD 2441170.285 + 10.085408 E.

The phase light curves for V360 Lac (Fig. 2) were constructed with these elements. The solid lines are ninth-order polynomial approximations for the J light curve. The bottom panel shows the phase $J - K$ color variations. The primary ($\Phi \sim 0$) and the secondary ($\Phi \sim 0.5$) J brightness minima are clearly seen in the figure, although their depths do not exceed a few tenths of a magnitude. A minimum near $\Phi \sim 0.5$ is

Table 3. Mean magnitudes of the binaries at their orbital maximum and minimum light

Parameter	Min I			Max			Min II		
	mean	sd	N	mean	sd	N	mean	sd	N
				RX Cas					
U	11.697	0.259	3	10.183	0.100	3	10.115	0.219	2
B	10.973	0.081	3	10.013	0.015	3	10.315	0.021	2
V	9.437	0.025	3	8.763	0.042	3	9.170	0.071	2
R	8.310	0.040	3	7.740	0.036	3	8.195	0.035	2
J	6.658	0.028	4	6.334	0.011	7	6.878	0.015	4
H	5.950	0.028	4	5.663	0.009	7	6.202	0.023	4
K	5.790	0.030	4	5.493	0.010	7	6.030	0.019	4
L	5.563	0.038	4	5.254	0.010	7	5.737	0.030	3
M	5.800	0.047	4	5.487	0.033	7	5.987	0.084	3
				KX And					
J	5.822	0.042	5	5.742	0.031	5	5.850	0.014	2
H	5.352	0.044	5	5.304	0.025	5	5.415	0.007	2
K	5.168	0.047	5	5.122	0.024	5	5.225	0.007	2
L	5.008	0.052	5	4.948	0.049	5	5.020	0.014	2
M	5.120	0.037	4	5.063	0.077	4	5.230	0.099	2
				V360 Lac					
J	5.683	0.055	3	5.550	0.021	6	5.655	0.035	2
H	5.480	0.040	3	5.390	0.018	6	5.490	0.014	2
K	5.373	0.040	3	5.293	0.023	6	5.400	0.028	2
L	5.325	0.007	2	5.208	0.016	6	5.290	0.042	2
M	5.270	0	1	5.258	0.101	6	5.060	0	1
				V367 Cyg					
J	5.863	0.059	3	5.300	0	3	5.803	0.015	3
H	5.477	0.038	3	4.997	0.021	4	5.503	0.015	3
K	5.300	0.044	3	4.820	0.039	4	5.330	0.030	3
L	4.923	0.049	3	4.498	0.017	4	4.987	0.055	3
M	4.523	0.015	3	4.365	0.147	4	4.637	0.112	3
				β Lyr					
J	3.98	0.02	2	3.20	0.02	5	3.66	0.03	4
H	3.82	0	2	3.13	0.02	5	3.62	0.02	4
K	3.63	0.01	2	3.02	0.02	5	3.51	0.01	4
L	3.32	0	2	2.77	0.03	5	3.25	0.01	4
M	3.33	0.01	2	2.75	0.07	5	3.17	0.01	4

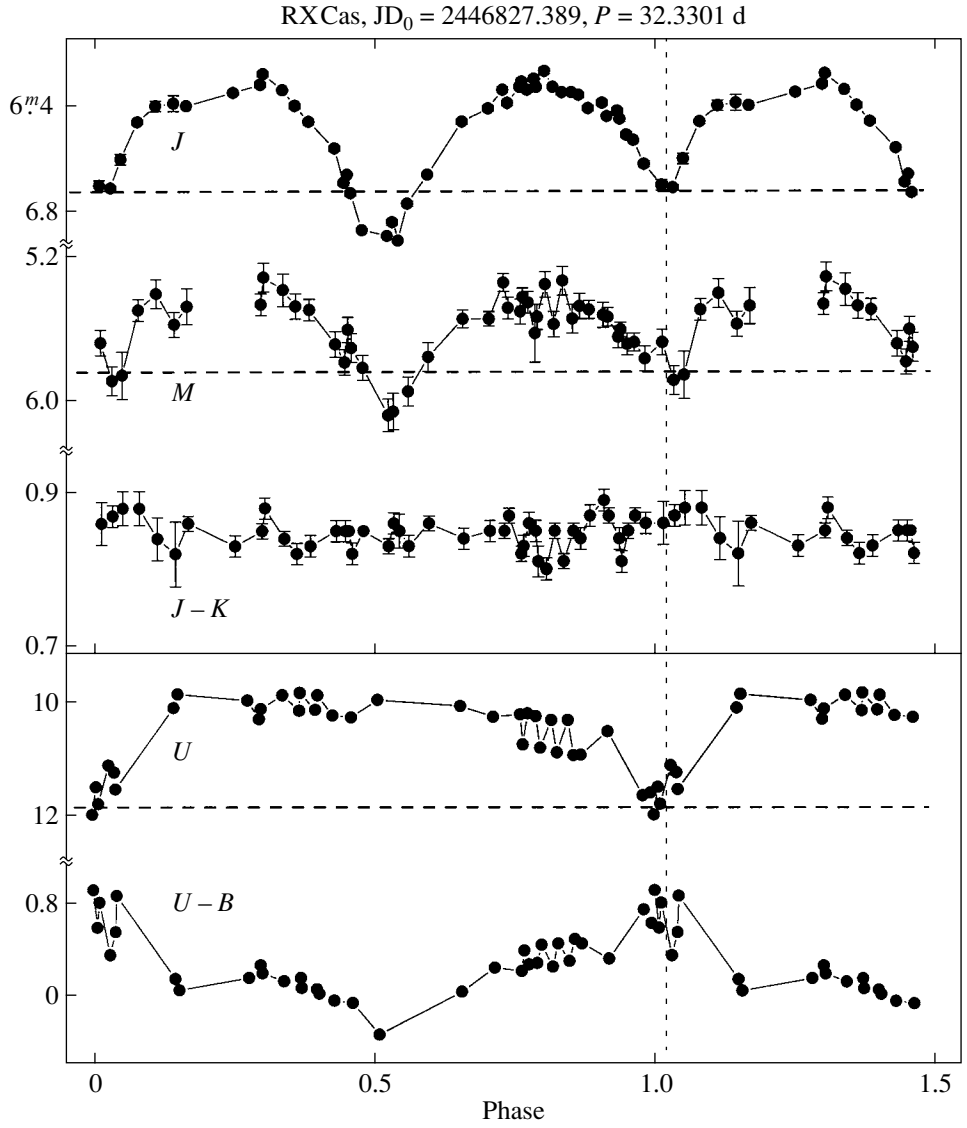

Fig. 1. Orbital brightness and color variations of RX Cas in the infrared and optical wavelength ranges. The vertical dotted line marks the phase of the primary minimum. The horizontal dashed lines indicate the levels of the primary minima.

also noticeable in the $J-K$ color variations; i.e. the hotter component is seen at the secondary minimum.

V367 Cyg. The binary V367 Cyg is a member of a multiple system in which two optical components are known: one is a faint ($V \sim 13^m.7$) star at a distance of about $2''$ from V367 Cyg, and the other is the star HD 198288 at a distance of less than $0''.1$. The latter component has not been detected by speckle interferometry, and its existence is currently open to question (Zola and Ogloza 2001). Since the contribution from the faint star to the total infrared radiation of V367 Cyg does not exceed a few fractions of a percent, all of the observed infrared (along with optical) radiation was attributed to the W Ser binary. The W Ser binary has a well-defined shell spectrum pointing to the existence of gas flows in the system. The spectrum imitates the radiation from an A7Ia star and makes it difficult to classify the stellar components of the binary using optical and infrared photometry.

In our previous paper (Taranova 1997), we classified the binary components as B0 and B0.5 giants and pointed out that there is an appreciable deficit of radiation in the U and B bands.

Figure 3 shows the phase JM light and $J-K$ color curves constructed from the 1996–2002 observations (Table 2) with the elements (Kholopov *et al.* 1985) JD(Min I) = 2437390.855 + 18.59773E. The shown dependences of the infrared brightness and color on the orbital phase are in good agreement with the ephemeris of 1979. The mean $J-K$

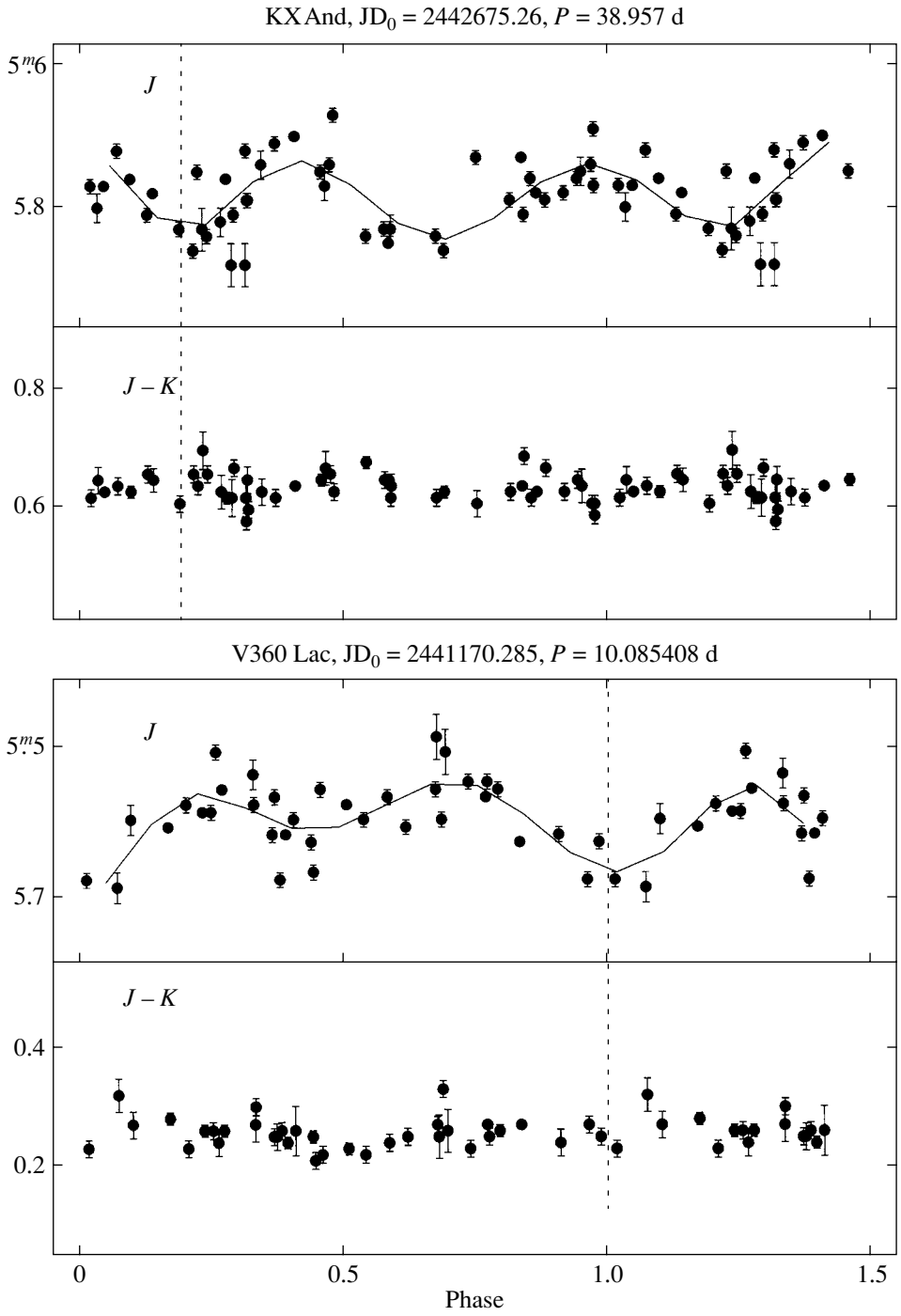

Fig. 2. Orbital J brightness and $J-K$ color variations in the binaries KX And and V360 Lac. The solid lines are ninth-order polynomial approximations of the observed J brightness variations.

color indices near the primary and secondary minima (Table 3) corrected for the interstellar extinction are $\sim 0^m.15$ and $\sim 0^m.06$–$0^m.07$, respectively. The color temperatures of such sources are $T_{C1} < 9000$ K and $T_{C2} > 11\,000$ K. The symbols $<$ and $>$ mean that, during partial eclipses, an illumination from the primary, generally hotter component and from the secondary, cooler component is possible in the former and latter cases, respectively.

On the other hand, it follows from the optical photometry by Heiser (1962) that the $U-B$ and $B-V$ color variations are within a few hundredths of a magnitude and that their mean values correspond to the spectral types A3–A4 and ~B2. If the pri-

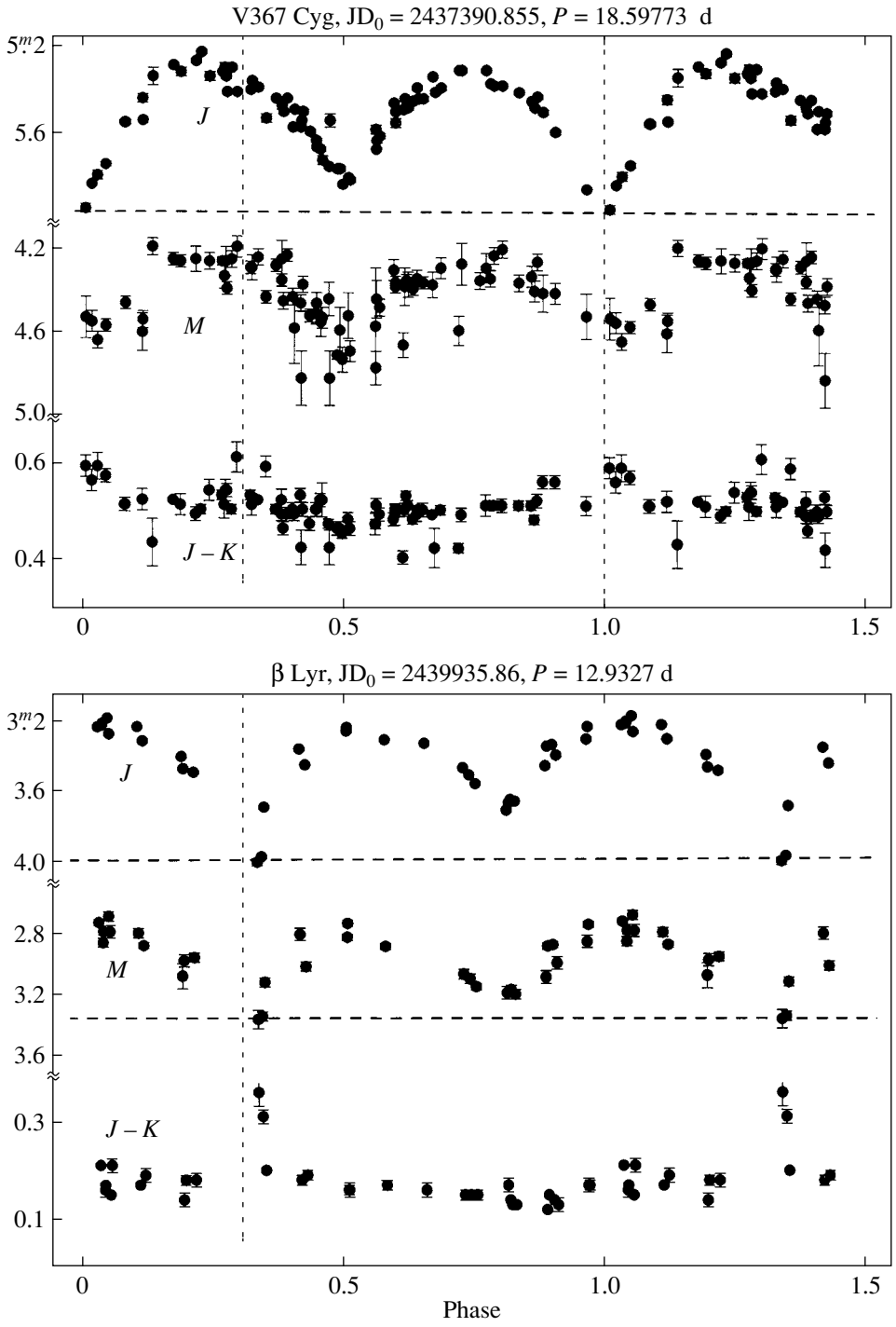

Fig. 3. Orbital JM brightness and $J - K$ color variations in the binaries V367 Cyg and β Lyr. The notation is the same as that in Fig. 1.

mary component were classified by the $V - J$ color index, whose mean value at the secondary minimum is $\sim -0^m.5$, then the spectral type of the source would be ~B0.5. Such a difference in the classification of the binary components is evidently attributable to the existence of a complex shell spectrum. The classification by infrared radiation is more correct, since the contribution from the shell lines to the range 1.25–5 μm is insignificant; therefore, we estimated the binary's parameters mainly from IR photometry, and their results are given below.

***β* Lyr.** The bright eclipsing binary β Lyr has been studied intensively for many years by all available means; nevertheless, it remains one of the most puz-

zling objects. The primary component of the system is classified as a B6–B8 giant; the secondary, more massive component is embedded in an optically thick accretion disk (Harmanec *et al.* 1996). Matter arrives to the accretion disk from the primary component, which fills its Roche lobe and rotates synchronously with the orbital motion (Harmanec and Scholz 1993). The orbital inclination is 80°–90°. Our $JHKLM$ photometry of this close binary (Table 2) was performed in the period 2003–2004.

Figure 3 shows the phase JM brightness and $J-K$ color variations constructed with the elements JD(Min I) = 2439935.86 + 12.9327E. These elements were taken from Jameson and Longmore (1976), who first performed infrared photometry (1.25–8.6 μm) of the binary in 1973. They pointed out that the depths of the minima become equal with increasing wavelength, and the secondary minimum becomes deeper than the primary one at wavelengths longer than 3.6 μm. This effect was not noticeable at the epoch of our observations (Fig. 3); the primary minimum remains deeper in the spectral range 1.25–5 μm.

We see from Fig. 3 that our series of observations is shifted in phase by about 0.3 with respect to the epoch of observations by Jameson and Longmore. If we associate the observed shift with an increase in the orbital period, then its value in 2003–2004 was 12.937 days; i.e. the increase in the period from 1973 (a mean Julian date of about 2442000) to 2003–2004 (a mean Julian date of about 2453000) was no less than 0.0043 days, i.e., the orbital period increased at a rate exceeded 1.4×10^{-4} days yr^{-1} or $\sim$25 s yr^{-1}. Harmanec and Scholz (1993) estimated the mean rate of increase in the period over 100 years (before 1990) to be 19 s yr^{-1}. The orbital period of β Lyr may increase with acceleration.

ESTIMATING THE PARAMETER OF THE BINARY COMPONENTS

We estimated the parameters for the components of the program binaries from our infrared photometry (Table 2) using optical photometry from the published papers of various authors. We made our estimates as follows.

When fitting the observed SEDs for each binary, we used the method of successive approximations, provided that both stellar components of each system were similar in photometric characteristics to normal stars (Johnson 1966; Korneef 1983). We first corrected all of the observed fluxes from the binary systems for the interstellar extinction (Table 1).

Initially, by analyzing the SEDs in the range 1.25–2.2 μm at different orbital phases, we estimated the color temperatures of the stellar components of the binaries, compared their values with the effective temperatures of normal stars (Johnson 1966), and determined the optimal spectral types of the stellar components. Based on the established spectral type, we extrapolated the radiation from the stellar components in the range 1.25–2.2 μm to the optical range and to wavelengths of 3.5 and 5 μm. Subsequently, the fluxes derived in the spectra of each stellar component of the binary in the range 0.36–5 μm were added in each band, and the result was compared with the observed flux from the binary at the orbital J brightness maximum.

At the next step, we estimated the total fluxes ($F_{\rm tot}$) from the stellar components. Their values were calculated from the component's SED in the range 0.36–5 μm by taking into account the contribution of this radiation to the component's total flux. The contribution was assumed to depend only on the component's temperature. As the latter, we took the color temperature estimated from the SED in the range 1.25–2.2 μm (see above).

Subsequently, we estimated the parameters of the binary components using the following relations.

(1) luminosity, $L = 4\pi r^2 F_{\rm tot}$;

$$\text{radius, } R = r[L/4\pi(\sigma T^4)]^{0.5}, \qquad (1)$$

where T is the component's temperature corresponding to its spectral type, and r is the distance to the system (Table 1);

(2) bolometric magnitude, $M_{\rm bol} = 4.75 - 2.5\log(L/L_\odot)$.

The set of L, R, and $M_{\rm bol}$ obtained for each of the components allows their luminosity classes to be estimated.

The 0.36–5 μm SEDs for the five binaries are shown in Fig. 4. All of the fluxes were corrected for the interstellar extinction (Table 1). Below, we give a description of the SEDs for each binary and the conclusions drawn from their analysis.

RX Cas. Our analysis of the 0.36–5 μm radiation from RX Cas at different orbital phases confirmed the existence of an ellipsoidal cool component, a K1 giant, in the system. During the orbital motion, its apparent radius changes by a factor of about 1.35. We estimated the flux of the hot component from the flux of RX Cas at the secondary minimum as the difference between the total flux and the flux from the cool giant. It turned out that the derived 0.36–0.7 μm SED of the hot source agrees with a color temperature of about 10 000 K. The binary's 0.36–5μm SEDs are shown in Fig. 4 (RX Cas).

We determined the total flux of the cool star ($F_{\rm tot}$) from its flux in the range 0.36–5 μm, which contains more than 95% of the total radiation for sources with temperatures in the range 4000–5000 K. A source

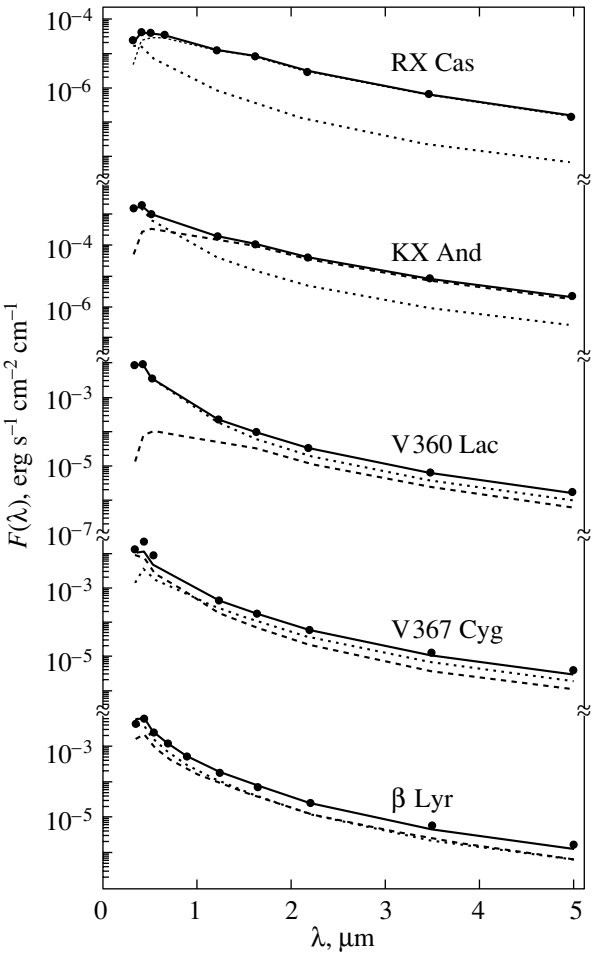

Fig. 4. Spectral energy distributions for the program binaries in the range 0.36–5 μm near quadratures: the filled circles indicate the observed fluxes; the dotted and dashed lines represent the spectral energy distributions for the primary (hotter) and secondary components of the binaries, respectively; and the solid lines represent the spectral energy distributions for the total radiation from the components of the binaries.

with a color temperature of ~10 000 K emits about 60% of its total radiation in the range 0.36–5 μm; taking into account this fraction, we estimated the total flux from the hot source. The remaining parameters were estimated using relations (1) and are given in the second and third columns of Table 4.

We assumed in our estimations that the temperature of the cool component at the primary minimum and at the maximum was 4600 K (K1) and that the distance to the system was $r = 600$ pc. It follows from these estimates that the system's cool component is a K1 giant. The luminosity and radius of the hot source are close to those of a star located slightly below the main sequence. The light from the gaseous envelope is visible only at the primary minimum as excess (against the radiation from the K1 giant) radiation in the U band (0.36 μm). We see from Fig. 4 that the total radiation of a K1 giant and a hot source with $T_C \sim 10\,000$ K describes satisfactorily the radiation from the binary at maximum light in the spectral range 0.36–5 μm.

Thus, our analysis of the new series of infrared observations for RX Cas in the period 1996–2002 generally confirms the main conclusions reached previously (Taranova 1987; Taranova and Shenavrin 1997) and allowed some of the parameters of the individual components to be improved.

KX And. We attempted to estimate and improve the parameters of the binary components using our 1996–2004 photometry for the binary (Table 2) and the UBV photometry by Steftl *et al.* (1990).

It follows from Table 3 and the UBV photometry that the light in the range 0.36–0.55 μm comes from the hotter source compared to the range 1.25–5 μm. For example, the color index $B - V \sim 0.14$ (Steftl *et al.* 1990), and, hence, the source's color temperature $T_C \sim 10\,000$ K. The color index $J - K \sim 0.5$ and $T_C \sim 5000$ K.

The observed 0.36–5 μm SED for KX And at maximum light (the filled circles in Fig. 4 (KX And)) can be optimally represented by the sum of radiations from two stars, a cool K(1 ± 1) giant and a hot source similar in parameters to a B(6 ± 1) giant.

The fourth and fifth columns of Table 4 give our estimates of the parameters for the stellar components of the binary KX And; their values were obtained from the total fluxes from B6 and K1 stars in the range 0.36–5 μm at a distance to KX And of $r = 700$ pc. Classifying the primary component as a hotter star would lead to a deficit of radiation in the range 0.36–0.45 μm.

The observed infrared light curves and our estimates of the radii for the stellar components yield an orbital inclination of no larger than 30°.

V360 Lac. To estimate the parameters for the components of this system, we used the technique described above for KX And. The optical photometry was taken from Pavlovski *et al.* (1997). Our analysis of the 0.36–5 μm SED for V360 Lac at maximum light (Fig. 4) indicates that the system's stellar components are sources similar to B3 and K2 stars. The sixths and seventh columns of Table 4 give our estimates of the total fluxes, radii (R), luminosities (L), and absolute magnitudes (M_{bol}) for the binary components. The cool and hot components are similar in parameters to giants and supergiants, respectively. The orbital inclination does not exceed 30°.

V367 Cyg. Classifying the components of this binary as normal stars (Johnson 1966; Korneef 1983) based on our 1996–2002 infrared photometry leads us to the following conclusion. The system's primary

Table 4. Estimated parameters for the components of the binaries

Parameter	RX Cas		KX And		V360 Lac		V367 Cyg		β Lyr	
	K1	10^4 K	B6III	K1III	B3I	K2III	B2I	F0I	B3I	A0I
$F_{\rm tot}$, erg s^{-1}cm^{-2}	3×10^{-8}	9×10^{-9}	8.2×10^{-8}	3.3×10^{-8}	6.5×10^{-7}	1.1×10^{-8}	6.2×10^{-7}	2×10^{-7}	2.5×10^{-6}	9.4×10^{-7}
L, $L_\odot$	335	100	1250	500	8500	140	12 200	3700	5700	2100
R, $R_\odot$	30	3.3	12	35	18	20	20	35	15	17
$M_{\rm bol}$	$-1\overset{m}{.}55$	$-0\overset{m}{.}25$	-3^m	-2^m	$-5\overset{m}{.}1$	$-0\overset{m}{.}6$	$-5\overset{m}{.}5$	$-4\overset{m}{.}2$	$-4\overset{m}{.}6$	$-3\overset{m}{.}5$

component is a B(1–3) supergiant, and the secondary component is a source with a spectrum similar to that of an F0 supergiant. Extrapolation of the radiation from these components to the optical range and comparison with the UBV photometry by Heiser (1962) show good agreement with the system's light in the U band (0.36 μm), although the fluxes in the B and V bands (0.45 and 0.55 μm) observed at maximum light exceed the total flux from the B2 and F0 components. The SED for V367 Cyg at maximum light is shown in Fig. 4 (V367 Cyg). The eighth and ninth columns of Table 4 give the parameters for the binary components.

***β* Lyr.** In estimating the parameters of the binary components, we used the $UBVRI$ photometry obtained by Bruton *et al.* in 1992 and 1995 and accessible at http://www.physics.sfasu.edu/astro/binstar.html.

At the primary minimum (Table 3), when the secondary (more compact) component of β Lyr is eclipsed, the radiation in the range 1.25–1.65 μm agrees with a blackbody source with a color temperature $T_{\rm C} \sim 8000$ K. The color temperature decreases with increasing wavelength; for example, the color index $K - L \approx 0.3$ and $T_{\rm C} \sim 3000$ K.

Our analysis of the SED for β Lyr in the optical and infrared ranges (0.36–5 μm) at different orbital phases shows that the binary components are B3 and A0 supergiants. The fitting errors for the maximum light of β Lyr do not exceed 10% of the flux. Figure 4 (β Lyr) presents the observed SED for β Lyr and the SEDs for the binary components in the range 0.36–5 μm near maximum light; the last two columns of Table 4 give our estimates of the parameters for the system's components.

EXCESS INFRARED RADIATION

In our studies of close binaries (Taranova and Shenavrin 1997; Taranova 1997), we detected excess (with respect to the total light from the systems' stellar components) radiation in the range 3.5–5 μm for the systems KX And, V367 Cyg, and RX Cas: for the first two systems, this was associated with the radiation from ionized disklike envelopes with emission measures of $\sim 6 \times 10^{59}$ cm^{-3} (KX And) and $\sim 8 \times 10^{59}$ cm^{-3} (V367 Cyg). The excess infrared radiation in the binary RX Cas was attributable to the existence of an optically thin circumstellar dust envelope.

Figure 5 shows the two-color $(J - K) - (K - L)$ diagram in which the filled circles indicate the mean color indices derived from our 1996–2004 data (Table 2). We see that the color excesses can be determined reliably only for the binaries V367 Cyg and β Lyr. Small excesses are probably present in KX And and RX Cas, and our conclusions regarding

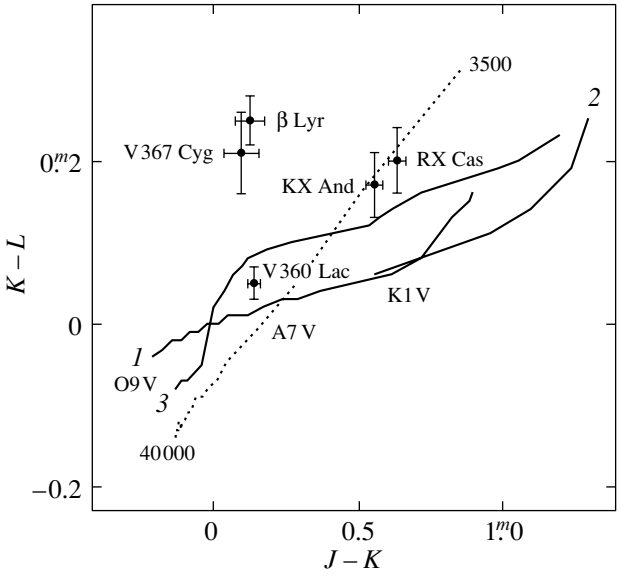

Fig. 5. Two-color $(J - K)-(K - L)$ diagram for the five binaries: the filled circles denote the mean observed values, the crosses are standard deviations, line *1* represents normal main-sequence stars, lines *2* and *3* represent normal giant and supergiant stars, respectively, and the dotted line indicates the colors of a blackbody with its temperature varying between 3500 and 40 000 K.

their nature and our estimates of the parameters for the sources of excess infrared radiation (Taranova and Shenavrin 1997; Taranova 1997) remain valid. No color excess was detected in the infrared radiation from the binary V360 Lac. The excess infrared radiation for the system V367 Cyg, whose hot component was classified as a B0 supergiant, was explained by the radiation of an ionized gas (Taranova 1997). In this paper, we classify the binary's hot source as a B2 supergiant (Table 4), and its radiation could be insufficient to ionize the gas envelope to the required level. In this case, the excess infrared radiation from V367 Cyg can be associated with the radiation from a circumstellar dust envelope. To reach a firm conclusion, we must improve the classification of the system's stellar components and to continue the infrared photometry of the binary. The same is true for the binary β Lyr: its infrared excess is determined with good accuracy, but its interpretation depends on the spectral classification of the hot component. A normal B3 supergiant as the hot star cannot provide the observed excess fluxes at wavelengths of 3.5 and 5 μm.

CONCLUSIONS

Thus, our analysis of the $JHKLM$ photometry for several close binaries has shown the following.

(1) A phase shift of the light curves by about 0.02 relative to the ephemeris of 1987, which corresponds to an increase in the orbital period by about 0.005 days over recent years, is clearly seen in the dependences of the infrared brightness of RX Cas on its orbital phase. The rate of increase in the period is about 3.5×10^{-4} days yr^{-1} or 30 s yr^{-1}. At the components' masses of 0.5 $M_\odot$ and 5 $M_\odot$, the rate of mass transfer between the components is $\sim 2 \times 10^{-6}$ $M_\odot$ yr^{-1}. Our analysis of the radiation from RX Cas in the range 0.36–5 μm at different orbital phases confirms the existence of an ellipsoidal cool component, a K1 giant, in the system. Its apparent radius changes by a factor of about 1.35 during the orbital motion. The 36–0.7 μm SED for the hot source agrees with a color temperature of $\sim$10 000 K.

(2) The observed infrared brightness variations of KX And in 1996–2004 were within $0^m.10$–$0^m.15$ and occurred with the same period as the U brightness variations prior to 1975, but the epochs of minima of the infrared light curves were shifted in phase by about 0.2, and the period increase in almost 30 years was about 0.049 days. The rate of increase in the period is $\sim 1.6 \times 10^{-3}$ days yr^{-1} or $\sim$140 s yr^{-1}. For the components' masses of about 10 $M_\odot$, the mass transfer rate between the components of the binary is $\sim 6.8 \times 10^{-5}$ $M_\odot$ yr^{-1}. The 0.36–5 μm SED for KX And at maximum light can be optimally represented by the sum of radiation from two stars: a cool K(1 ± 1) giant and a hot source similar in parameters to a B(6 ± 1) giant. The observed infrared light curves and the estimates of the radii for the stellar components yield an orbital inclination of no more than 30°.

(3) The infrared brightness variations of V360 Lac in 1996–2002 with orbital phase agree with the elements calculated for optical observations prior to 1971. The primary and secondary infrared brightness minima are clearly seen in the phase light curves, although their depths do not exceed a few tenths of a magnitude. A minimum near $\Phi \sim 0.5$ is also seen in the $J - K$ color variations; i.e., we see the hotter component at the secondary minimum. Our analysis of the 0.36–5 μm SED for V360 Lac (Fig. 4) indicates that the system's stellar components are sources similar to B3 and K2 stars. The cool and hot components are similar in parameters to giants and supergiants, respectively. The orbital inclination does not exceed 30°.

(4) The dependences of the infrared brightness and color of V367 Cyg on its orbital phase are in good agreement with the ephemeris of 1979. The mean $J - K$ color indices near the primary and secondary minima are $\sim 0^m.15$ and $\sim 0^m.06 - 0^m.07$, respectively. The color temperatures of such sources are $T_{C1} <$ 9000 K and $T_{C_2} >$ 11 000 K. The system's primary component is a B(1–3) supergiant, and the secondary component is a source with a spectrum similar to that of an F0 supergiant.

(5) The observed infrared brightness variations of β Lyr folded with the orbital elements derived from observations before 1973 exhibit a phase shift by about 0.3. The increase in the orbital period from 1973 to 2003–2004 was $\sim$0.0043 days. The rate of increase in the orbital period is $\sim 1.4 \times 10^{-4}$ days yr^{-1} or $\sim$25 s yr^{-1}. Our analysis of the SED for β Lyr in the optical and infrared ranges (0.36–5 μm) at different orbital phases shows that the binary components are B3 and A0 supergiants. The fitting errors for the maximum light of β Lyr do not exceed 10% of the flux.

(6) Excess radiation (with respect to the radiation from the stellar components) at wavelengths of 3.5 and 5 μm was observed in all of the program stars.

ACKNOWLEDGMENTS

We are grateful to the Ministry of Education and Science (the *Astronomy* Federal Science and Technology Program) for partial financial support.

REFERENCES

1. M. C. Akan, Astrophys. Space Sci. **135**, 157 (1987).
2. J. Andersen, K. Pavlovski, and V. Piirola, Astron. Astrophys. **215**, 272 (1989).
3. D. Bruton, R. Linenschmidt, and Jr. Schmude, http://www.physics.sfasu.edu/astro/binstar.htm1 (1992, 1995).
4. M. Floquet, A. M. Hubert, J. P. Maillard, *et al.*, Astron. Astrophys. **214**, 295 (1989).
5. M. Floquet, A. M. Hubert, J. P. Maillard, and J. Chauville, Astron. Astrophys. **294**, 227 (1995).
6. E. F. Guinan, R. H. Koch, and M. J. Plavec, Astrophys. J. **282**, 667 (1984).
7. P. Harmanec and G. Scholz, Astron. Astrophys. **279**, 131 (1993).
8. P. Harmanec, F. Morand, D. Bonneau, *et al.*, Astron. Astrophys. **312**, 879 (1996).
9. A. M. Heiser, Astrophys. J. **135**, 78 (1962).
10. G. Hill, P. Harmanec, K. Pavlovsky, *et al.*, Astron. Astrophys. **324**, 965 (1997).
11. R. F. Jameson and A. J. Longmore, Mon. Not. R. Astron. Soc. **174**, 217 (1976).
12. H. L. Johnson, Annu. Rev. Astron. Astrophys. **4**, 163 (1966).
13. H. L. Johnson, R. I. Mitchel, B. Iriarte, and W. Z. Wisnievski, Comm. Lunaz and Planet. Lab. **4**, 99 (1966).
14. P. Kalv, Publ. Tartu Obs. **60**, 3 (1979).
15. P. N. Kholopov, N. N. Samus', V. P. Goranskiĭ, *et al., General Catalogue of Variable Stars* (Nauka, Moscow, 1985).
16. J. Korneef, Astron. Astrophys. **128**, 84 (1983).
17. S. Kriz, J. Arsenijevic, J. Grygar, *et al.*, Bull. Astron. Inst. Czech. **31**, 284 (1980).
18. D. Ya. Martynov, G. V. Zaĭtseva, and M. I. Kumsiashvili, Perem. Zvezdy **21**, 451 (1980).
19. Oh Kyu-Dong, Proc. Astron. Soc. Aust. **9**, 289 (1991).
20. K. Pavlovski, P. Harmanec, H. Bozic, *et al.*, Astron. Astrophys. **125**, 75 (1997).
21. J. P. Phillips, M. J. Selby, R. Wade, and C. S. Magro, Mon. Not. R. Astron. Soc. **190**, 337 (1980).
22. R. S. Polidan, in *IAU Symposium No. 70 (Merrill-McLaughlin Memorial Symposium): Be and Shell Stars, Bass River, Massachusetts, USA, 1975,* Ed. by A. Slettebak (Reidel, Dordrecht, 1976), p. 401.
23. S. Steftl, P. Harmanec, J. Horn, *et al.*, Bull. Astron. Inst. Czech. **41**, 29 (1990).
24. O. G. Taranova, Pis'ma Astron. Zh. **13**, 502 (1987) [Sov. Astron. Lett. **13**, 206 (1987)].
25. O. G. Taranova, Pis'ma Astron. Zh. **23**, 810 (1997) [Astron. Lett. **23**, 704 (1997)].
26. O. G. Taranova and V. I. Shenavrin, Pis'ma Astron. Zh. **23**, 803 (1997) [Astron. Lett. **23**, 698 (1997)].
27. S. Zola and W. Ogloza, Astron. Astrophys. **368**, 932 (2001).

Translated by N. Samus'

Astronomy Letters, Vol. 31, No. 9, 2005, pp. 612–619. Translated from Pis'ma v Astronomicheskiĭ Zhurnal, Vol. 31, No. 9, 2005, pp. 684–692.

Oscillations of Optical Emission from Flare Stars and Coronal Loop Diagnostics

A. V. Stepanov[1*], Yu. G. Kopylova[1], Yu. T. Tsap[2], and E. G. Kupriyanova[1]

[1] *Pulkovo Astronomical Observatory, Russian Academy of Sciences, Pulkovskoe sh. 65, St. Petersburg, 196140 Russia*

[2] *Crimean Astrophysical Observatory, p/o Nauchnyi, Crimea, 98409 Ukraine*

Received April 15, 2005

Abstract—Based on an analogy between stellar and solar flares, we investigate the ten-second oscillations detected in the U and B bands on the star EV Lac. The emission pulsations are associated with fast magnetoacoustic oscillations in coronal loops. We have estimated the magnetic field, $B \approx 320$ G; the temperature, $T \approx 3.7 \times 10^7$ K; and the plasma density, $n \approx 1.6 \times 10^{11}$ cm^{-3}, in the region of energy release. We provide evidence suggesting that the optical emission source is localized at the loop footpoints.

Key words: *stars—variable and peculiar, stellar flares, coronal loops, oscillations, EV Lac, plasma diagnostics.*

INTRODUCTION

Cool dwarf stars with irregular variability (UV Cet stars) are estimated (Gershberg 2002) to comprise from 40 to 90% of all stars in our Galaxy. Observations show that, in contrast to solar flares, the visual luminosity of such stars can increase by several orders of magnitude, while their emission is often at a maximum in the optical wavelength range. Nonetheless, there is currently strong evidence for a common origin of flare energy release on the Sun and stars (Gershberg 2002).

The main structural elements of solar and red-dwarf coronae are magnetic loops. A special role is assigned to loop structures in the overwhelming majority of current models for flare energy release. According to the universally accepted scenario of solar flares, accelerated particles precipitating at the footpoints of coronal loops through diffusion are accumulated in the latter during energy release. The heated dense plasma of the lower atmosphere emits in Balmer lines and in the optical continuum, whereas its hottest part, with a temperature of $T = 10^7 - 10^8$ K, while evaporating, fills the loop structures and cools radiatively in the ultraviolet and soft X-ray ranges.

The validity of this approach for the Sun follows both from the spatial coincidence of the continuum and hard X-ray emission sources and from the temporal correlation between the time profiles (Matthews *et al.* 2003; Metcalf *et al.* 2003; Xu *et al.* 2004; Chen and Ding 2005), including the microwave range (Fang and Ding 1995). This is also evidenced by Neupert's effect (Neupert 1968), which suggests a coincidence in the behavior of the profiles for the emission attributable to chromospheric plasma evaporation with the time-integrated emission generated by accelerated particles. For red dwarfs, this effect was found, in particular, by Hawley *et al.* (1995) on AD Leo by analyzing the optical and ultraviolet emission profiles. Since the emission sources cannot yet be resolved on flare stars due to their great distances, Neupert's effect may be considered as a weighty argument for the scenario described above.

Indirect techniques including a large number of unknown parameters (Reale 2002) are commonly invoked to diagnose stellar loops. Therefore, the results obtained by different authors differ markedly. For example, depending on the adopted constraints, the characteristic lengths of coronal loops L vary between several stellar radii R_* (Benz *et al.* 1998) and $L < 0.1R_*$ (Reale 2002), while the flare plasma densities vary between 10^7 and 10^{12} cm^{-3} (Mullan 1976; Mathioudacis *et al.* 2003). Therefore, the methods for diagnosing the parameters of coronal loops on flare stars should be developed further. Substantial progress in this direction can be made by analyzing the fine temporal structure of the emission from stellar flares.

[*] E-mail: stepanov@gao.spb.ru

1063-7737/05/3109-0612$26.00

As follows from observations, in certain cases, quasi-periodic pulsations with periods from several seconds (Andrews 1990) to several minutes (Mathioudacis *et al.* 2003) are superimposed on smooth light curves of flare stars. These were first detected (Rodono 1974) during observations of the star H II 2411 (dM4e). Oscillations with a mean period of $P \approx 13$ s and a modulation depth of about 15% were detected during the flare of November 28, 1972. Andrews (1990) also managed to distinguish quasi-periods in the optical (13 and 8 s) oscillations observed in the U band 10 to 15 min after the maximum of a flare on AT Mic (dM4.5e). Nevertheless, in view of the possible atmospheric and instrumental effects, the stellar origin of these pulsations remained an open question.

Recently, in-phase quasi-periodic oscillations were detected in the U and B bands with periods $P = 10-30$ s during simultaneous observations of three flares on EV Lac using telescopes at the Terskol peak (Northern Caucasus), at the Stephanion Observatory (Greece), at the Crimean Observatory, and in Belogradchik (Bulgaria) (Zhilyaev *et al.* 2000). Their pulsed fractions in the U and B bands were 10–15 and 2.5%, respectively. Thus, it has been convincingly shown that the oscillations of flare stellar emission actually exist.

Mullan (1976) suggested associating the quasi-periodic oscillations detected by Rodono (1974) with the propagation of a whistler wave packet in the dipole magnetic field of the star. Subsequently, based on an analogy between solar and stellar flares, he developed the theory by Ionson (1984) about the interaction of convective motions with coronal magnetic loops in active regions (Mullan 1984). However, within the framework of this hypothesis, it is difficult to understand why quasi-periodic oscillations of flare emission are not observed in all events. In our view, an approach suggested by Zaitsev and Stepanov (1989) appears more attractive; according to this approach, the observed pulsations of solar flares are produced by flare energy release or chromospheric plasma evaporation, causing a sharp rise in the gas pressure inside the loop and the excitation of magnetohydrodynamic (MHD) eigenmodes. This model has been repeatedly invoked to interpret the minute oscillations observed on flare stars (Mullan *et al.* 1992; Mathioudacis *et al.* 2003). In these papers, the emission modulation was assumed to be produced by kink coronal loop oscillations. Meanwhile, as we show in the next section, these wave modes are unlikely to be capable of producing large-amplitude emission oscillations.

In this paper, we consider the optical quasi-periodic oscillations detected by Zhilyaev *et al.* (2000) during a flare on EV Lac on September 11, 1998. Using a technique based on the ideas of sausage fast magnetoacoustic (FMA) modes of coronal loops, we estimate the flare plasma parameters and discuss the localization of the optical emission source of stellar flares.

THE EIGENMODES OF CORONAL LOOPS

When gravity is ignored, it follows from the linearized system of equations of ideal MHD (Priest 1982) that four principal modes can be excited in a magnetic loop: torsional, kink, slow magnetoacoustic (SMA), and sausage FMA modes (Roberts *et al.* 1984; Hollweg 1984; Aschwanden 2003; Goossens *et al.* 2002; Roberts 2004). Let us consider the most important properties of the eigenmodes. We restrict our analysis to the first harmonics, for which the number of half-waves that fit along the loop is $q = 1$, by assuming that these are excited the most efficiently.

For the torsional and kink modes, the oscillation periods are, respectively,

$$P_{\rm tor} = 2L/v_{\rm A_i},$$

$$P_{\rm kink} \approx 2L/v_f, \quad v_f^2 = \frac{\rho_{\rm i} v_{\rm A_i}^2 + \rho_{\rm e} v_{\rm A_e}^2}{\rho_{\rm i} + \rho_{\rm e}},$$

where $v_{\rm A_i}$ and $v_{\rm A_e}$ are the Alfvén speeds inside (i) and outside (e) the loop, $\rho_{\rm i}$ and $\rho_{\rm e}$ are the corresponding densities.

We note at once that the torsional modes do not compress a plasma. We show in the Appendix that the kink modes compress a plasma only slightly. It thus follows that these modes cannot be responsible for the pulsations observed on EV Lac. Indeed, if the torsional modes arose from the increase in the gas pressure inside the loop due to flare energy release, then this would cause the longitudinal magnetic field B_z to change. For the kink modes, $\delta B_z \ll \delta B_r$ and δB_φ (see A.20). Therefore, assuming, for example, that $\delta B_z/B_z \sim 0.1$, we obtain $\delta B_r/B_z \sim \delta B_\varphi/B_z \sim 1$. Large amplitudes of the corresponding magnetic field components suggest large values of the plasma parameter, $\beta \sim 1$. Under coronal conditions, $\beta \approx c_{\rm s}^2/v_{\rm A}^2 \ll 1$, where $c_{\rm s}$ is the speed of sound, and, hence, the modes under consideration can hardly be responsible for the observed ten-second oscillations of the flare emission.

The FMA modes weakly perturb the magnetic field, and their period is (Aschwanden 2003)

$$P_{\rm sound} \approx 2L/c_{T_{\rm i}}, \quad c_{T_{\rm i}}^2 = \frac{c_{\rm s_i}^2 v_{\rm A_i}^2}{c_{\rm s_i}^2 + v_{\rm A_i}^2}. \qquad (1)$$

According to (1), the coronal loop length L is

$$L \approx c_{s_i} P_{sound}/2 = 5.86P\sqrt{T}.$$

Assuming that the temperature is $T = 10^7$–10^8 K and $P = 10$ s in the latter formula, we obtain $L = (2–6) \times 10^8$ cm. The radius of EV Lac is $R_* = 0.39R_\odot$, and, hence, $L/R_* = (0.7–2) \times 10^{-2}$, which seems unlikely in light of the powerful energetics of stellar flares.

The sausage modes efficiently modulate both the plasma density and the magnetic field strength (see Appendix). Depending on whether these generate traveling MHD waves in the surrounding medium or not, leaky or nonleaky modes can be excited in a coronal loop (see, e.g., Kopylova *et al.* 2002). The choice between these is determined by the loop parameters. In particular, at low values of the plasma parameter, $\beta \ll 1$, the critical longitudinal wave number is (Nakariakov *et al.* 2003)

$$k_c \approx \frac{j_0}{a}\left(\frac{v_{A_e}^2}{v_{A_i}^2} - 1\right)^{-1/2}, \qquad (2)$$

where $j_0 \simeq 2.4$ is the first zero of the Bessel function J_0, and a is the radius of the loop cross-section. Nonleaky and leaky modes are excited at $k \geq k_c$ and $k < k_c$, respectively. For example, when $v_{A_e}/v_{A_i} = 3$, we obtain $a/L \approx 0.3$ from Eq. (2) by setting $k_c = \pi/L$. This suggests that the coronal loops must be fairly thick in the case of excitation of nonleaky modes. At the same time, TRACE observations show (Aschwanden *et al.* 1999) that the solar coronal loops have a small ratio $a/L \ll 1$. Therefore, in our view, the leaky modes with the period (Kopylova *et al.* 2002)

$$P_{saus} = 2\pi a/(j_0 v_r), \quad v_r^2 = v_{A_i}^2 + c_{s_i}^2 \qquad (3)$$

are most likely responsible for the observed oscillations on EV Lac.

FLARE PLASMA DIAGNOSTICS

Let the flare energy release in a coronal loop, which can be represented as a magnetic trap (a coronal magnetic bottle), lead to the excitation of FMA oscillations (see Fig. 1). Since the plasma parameter under solar and stellar coronal conditions is $\beta = 8\pi p/B^2 \ll 1$, following Zaitsev and Stepanov (1982), we obtain for the amplitude of the magnetic field perturbation δB, attributable to a rise in the gas pressure p inside the loop,

$$p + \frac{B\delta B}{4\pi} = 0, \qquad (4)$$

where we assumed that $B_z = B$. Writing Eq. (4) as

$$\beta = |2\delta B/B|, \qquad (5)$$

we conclude that the relative perturbation amplitude $\delta B/B$ is determined by the parameter β.

The FMA oscillations of a coronal loop are damped mainly due to the losses through the emission of MHD waves into the surrounding medium (the acoustic mechanism) (see, e.g., Kopylova *et al.* 2002) as well as the dissipative processes in the loop itself (Zaitsev and Stepanov 1982; Stepanov *et al.* 2004). Papers in which the rapid damping of the kink oscillations of solar coronal loop observed from the TRACE satellite is associated either with an Alfvén resonance (Ruderman and Roberts 2002) or with phase mixing (Roberts 2000, 2004) have appeared in recent years. In the former case, the damping is attributable to the presence of a singularity in the wave equation at $\omega = kV_A(r)$. This suggests a sharp rise in the perturbation amplitude near the resonance surface. In the latter case, the dissipation is enhanced appreciably by the transverse gradient in Alfvén speed, causing the viscous stresses to grow. However, the physical nature of the Alfvén resonance has not yet been elucidated (Bellan 1994), while the phase mixing is efficient only for strongly inhomogeneous coronal loops; therefore, below, we will disregard these dissipation mechanisms. In addition, based on an analogy with solar flares, we will also disregard the damping of sausage FMA oscillations by assuming that the plasma density inside the flare loop is several orders of magnitude higher than that outside (Kopylova *et al.* 2002).

Estimates (Stepanov *et al.* 2004) indicate that the ion viscosity (v) and the electron heat conductivity (c) make a major contribution to the damping of the FMA oscillations of coronal loops; the total damping decrement is

$$\gamma_\Sigma = \gamma_v + \gamma_c \qquad (6)$$
$$= \frac{1}{12\sqrt{2}}\sqrt{\frac{M}{m}}\frac{\omega^2}{\nu_{ei}}\beta\sin^2\theta\left(1 + \sqrt{\frac{32M}{m}}\beta\cos^2\theta\right).$$

Here, M and m are the ion and electron masses, respectively, and $\theta = \arctan(k_\perp/k_{||})$ is the angle between the direction of the magnetic field $\mathbf{B}$ and the wave vector $\mathbf{k}$, where the longitudinal wave number $k_{||} \approx \pi/L$, while the transverse wave number $k_\perp \approx j_0/a$. The effective electron–ion collision frequency in (6) is defined as follows (Ginzburg 1970):

$$\nu_{ei} = \frac{5.5n}{T^{3/2}}\ln\left(10^4\frac{T^{2/3}}{n^{1/3}}\right) \approx 60\frac{n}{T^{3/2}}\ \mathrm{s}^{-1}.$$

Since the oscillation Q factor is $Q = \omega/\gamma_\Sigma$, we derive formulas for the flare plasma parameters (temperature T, particle density n, and magnetic field B) from Eqs. (2) and (6) using the period $P = P_{saus}$, the Q factor, and the plasma parameter β:

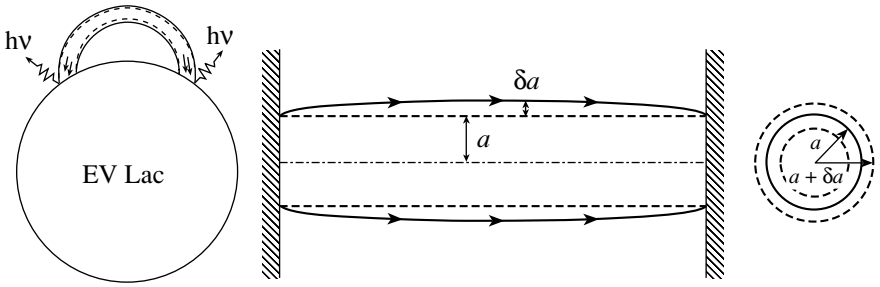

Fig. 1. Schematic view of the model for the pulsations of optical flare emission (left). The global sausage mode of a coronal loop associated with the axisymmetric variations in its diameter (right).

$$T \approx 1.2 \times 10^{-8} \frac{\tilde{r}^2 \beta}{P^2 \chi}, \quad (7)$$

$$n \approx 3.49 \times 10^{-13} \frac{\tilde{r}^3 \kappa \beta^{5/2} Q \sin^2 \theta}{P^4 \chi^{3/2}}, \quad (8)$$

$$B \approx 3.81 \times 10^{-18} \frac{Q^{1/2} \tilde{r}^{5/2} \kappa^{1/2} \beta^{5/4} \sin \theta}{P^3 \chi^{5/4}}, \quad (9)$$

where $\tilde{r} = 2\pi a/j_0$, $\kappa = 243\beta \cos^2 \theta + 1$.

To find the relationship between the modulation depth of the optical emission attributable to the flux of accelerated electrons precipitating at the flare loop footpoints,

$$\Delta = (F_{\max} - F_{\min})/F = 2\delta F/F, \quad (10)$$

where $F_{\max} = F + \delta F$ and $F_{\min} = F - \delta F$ are the maximum and minimum fluxes of the modulated emission, respectively, and the plasma parameter β, we turn to the model of a coronal magnetic bottle (Stepanov and Tsap 1999, 2002).

Depending on the escape time T_0 of the trapped electrons from the trap, their diffusion time T_D, and the mirror ratio σ, three regimes of electron pitch-angle diffusion into the loss cone can be realized in magnetic traps: weak ($T_D > \sigma T_0$), moderate ($T_0 < T_D < \sigma T_0$), and strong ($T_D < T_0$). The diffusion of accelerated electrons is determined by Coulomb collisions rather than whistlers if $T_{D_c} < T_{D_w}$, where T_{D_c} and T_{D_w} are the diffusion time scales on background plasma particles and waves, respectively (Stepanov and Tsap 1999). Since

$$T_{D_c} \approx 4.2 \times 10^9 \frac{E^{3/2}}{n\Lambda},$$

where the Coulomb logarithm $\Lambda = 24 - \ln(n^{1/2}/T_e)$, T_e is the background electron temperature in eV, and E is the fast electron energy in keV, assuming that $n = 10^{11}$ cm^{-3}, $T_e = 1$ keV, and $E = 50$ keV in the latter formula (Grinin *et al.* 1993), we obtain $T_{D_c} \approx 0.8$ s. Taking $L = 10^{10}$ cm for the flare loop length and $v = 1.3 \times 10^{10}$ cm s^{-1} ($\approx$50 keV) for the electron velocity, we obtain the characteristic particle escape time from the trap $T_0 \approx L/(2v) \approx 0.4$ s. Consequently, $T_0 \lesssim T_{D_c} < \sigma T_0$ at $\sigma \gtrsim 10$; i.e., the moderate diffusion regime is realized in stellar coronal loops. As regards the whistlers and the related regime of strong diffusion, the electron pitch-angle diffusion on Coulomb collisions appears preferred, since these undergo strong Landau damping due to the high background plasma temperature (Stepanov and Tsap 2002).

In the adopted model, the variations of the optical emission from the loop footpoints are determined by the variations in the flux of passing electrons S, which in the regime of moderate diffusion is $S \approx Nv/(\sigma L)$, where N is the number of trapped particles (Stepanov and Tsap 1999). Since the mirror ratio is $\sigma = B_{\max}/B$, $S \propto \sigma^{-1} \propto B$. It thus follows that the flux variations δS are determined by the variations in the magnetic field of the coronal part of the loop and $\delta S \propto \delta B$ and, therefore, $\delta F/F \approx \delta S/S \approx \delta B/B$; hence, according to (5) and (10), we obtain for the modulation depth Δ

$$\Delta \approx \beta. \quad (11)$$

As follows from observations (Zhilyaev *et al.* 2000), $P \approx 13$ s, $Q \approx 50$, and $\Delta \approx 0.2$ for the event of September 11, 1998 (Fig. 2). Based on an analogy between solar and stellar flares and setting $a/L = 0.1$, we then obtain $\theta \approx \arctan[j_0 L/(\pi a)] \approx 76°$. Using this value and assuming that $\tilde{r} = 2.62a \approx 2.62 \times 10^9$ cm, we find the plasma temperature $T = 3.7 \times 10^7$ K, the particle density $n = 1.6 \times 10^{11}$ cm^{-3}, and the magnetic field $B = 320$ G from (7)–(11).

We particularly emphasize that, according to our model for the oscillations of flare loops on EV Lac, the characteristic loop length is $L \approx 0.4R_*$, while on the Sun $L \approx 0.01R_\odot$. If, however, we set the loop radius a equal to 10^8 or 10^{10} cm, then we will obtain either greatly underestimated (1.6×10^8 cm^{-3}) or greatly overestimated (1.6×10^{14} cm^{-3}) densities n from (7)–(11). This result is consistent with the

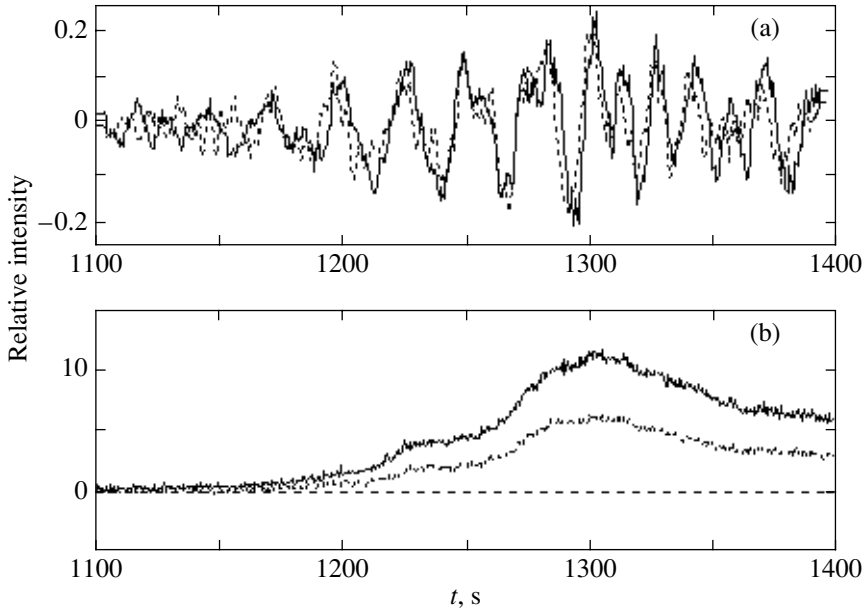

Fig. 2. (a) The oscillations of the U (solid line) and B (dotted line) emission with a period $P \approx 13$ s separated from the light curve for EV Lac, the flare of September 11, 1998. (b) The U and B light curves. The amplitude of the relative intensity of the optical emission $I_{\rm flare}/I_{\rm star}$ ($I_{\rm flare}$ and $I_{\rm star}$ are the intensities of the flare emission and the background stellar emission, respectively) in the B band was increased by a factor of 5 in both panels. The figure was taken from Zhilyaev *et al.* (2000).

direct VLBA/VLA observations of the coronae on the stars UV Ceti, AD Leo, and YZ CMi (Benz *et al.* 1998; Pestalozzi *et al.* 2000) and with other model calculations (Haisch 1983).

ON THE SOURCE OF OPTICAL EMISSION

Mullan *et al.* (1992) assumed that the optical emission from flares could be determined by the bremsstrahlung of a hot plasma in the coronal part of the loop. However, an analogy between solar and stellar flares suggests that the optical emission source is localized at the loop footpoints. Therefore, let us make estimates using our model.

The bremsstrahlung fluxes for optically thin and thick sources, respectively, can be represented as (Priest 1982)

$$F_1 \propto \frac{n^2}{\sqrt{T}}V, \quad F_2 \propto TV, \tag{12}$$

where $V \approx \pi a^2 L$ is the volume of the emitting region. Taking into account the adiabatic equation $n^{3/2}/T = \text{const}$, we obtain in place of (12)

$$F_1 \propto n^{5/4}V, \quad F_2 \propto n^{3/2}V. \tag{13}$$

Since the excitation of FMA oscillations causes the volume of the emitting region to change due to variations in the loop radius a,

$$\frac{\delta V}{V} = \frac{2\delta a}{a}. \tag{14}$$

In turn, it follows from the condition for the conservation of the longitudinal magnetic flux, $Ba^2 = \text{const}$, that

$$\frac{\delta B}{B} = -\frac{2\delta a}{a}. \tag{15}$$

Using (15), we transform Eq. (14) to

$$\frac{\delta V}{V} = -\frac{\delta B}{B}. \tag{16}$$

The following relation holds for the FMA modes (Braginskiĭ 1963):

$$\frac{\delta n}{n} = \frac{\delta B}{B}\sin\theta, \tag{17}$$

and we obtain from (13), (16), and (17)

$$\frac{\delta F_1}{F_1} = (1.25\sin\theta - 1)\frac{\delta B}{B}, \tag{18}$$
$$\frac{\delta F_2}{F_2} = (1.5\sin\theta - 1)\frac{\delta B}{B}.$$

Thus, according to (5), (6), and (18), we have

$$\Delta_1 \approx (1.25\sin\theta - 1)\beta, \tag{19}$$
$$\Delta_2 \approx (1.5\sin\theta - 1)\beta.$$

Substituting the same parameters as those in the previous case into (7)–(9), we obtain using (19) $T \approx 9 \times 10^7$ K, $n \approx 10^{13}$ cm^{-3}, and $B \approx 2000$ G for an optically thin source and $T \approx 6 \times 10^7$ K, $n \approx 1.4 \times 10^{12}$ cm^{-3}, and $B \approx 850$ G for an optically thick

source, whence we find the plasma parameter $\beta_1 \approx 0.9$, $\beta_2 \approx 0.5$.

Coronal loops with large values of the parameter β are very unstable against flute perturbations (Shibasaki 2001). The hypothesis by Mullan *et al.* (1992) that the optical emission source could be localized in the coronal part of the loop is in poor agreement with the adopted model.

DISCUSSION OF RESULTS AND CONCLUSIONS

In this paper, we associated the observed ten-second optical quasi-periodic oscillations detected during the flare energy release on EV Lac with the sausage FMA modes of coronal loops, which produce the deepest modulation of the emission. This allowed us to estimate the main parameters of coronal loops from the observed period P, the modulation depth Δ, and the pulsation Q factor. Based on the suggested model, we showed that the hypothesis by Mullan *et al.* (1992), in which the optical emission of stars is determined by a hot flare plasma in the loop volume, runs into difficulties.

When performing our calculations based on an analogy between stellar and solar flares, we assumed that $a/L \sim 0.1$. The observations of soft X-ray emission from the coronae of flare stars in binary systems argue for the validity of this approach. Thus, for example, using observational data from the Italian BeppoSAX orbiting observatory, Schmitt and Favata (1999) were able to detect an eclipse of the flare coronal plasma of component A by component B in the binary Algol. This allowed the characteristic heights h of coronal loops to be estimated. It turned out that $h \leq 0.6R_*$, which is in satisfactory agreement with our estimates of the loop lengths on EV Lac ($L \approx 0.4R_*$). VLBI observations of the dMe star UV Ceti, which showed that the coronal loops could extend to distances of $(2–4)R_*$ (Benz *et al.* 1998), provide further evidence for the larger sizes of stellar coronal loops than those on the Sun.

According to Zhilyaev *et al.* (2000), the modulation depth in the U band is several times larger than that in the B band. In our opinion, this is because the energy of accelerated particles transforms into the thermal energy of plasma mainly in the upper layers of the lower atmospheres of stars. This inevitably leads to an increase in the role of the smoothed fluxes of heat and radiation (back-warming) in heating the deeper and cooler lower layers.

Mullan *et al.* (1992) also used a model suggested by Zaĭtsev and Stepanov (1989) to interpret the minute oscillations observed on red dwarfs. The modulation was determined by the kink modes, whose excitation, as we showed, due to a rise in the gas pressure in the loop appears rather problematic. We also emphasize that in performing our analysis, including the model by Mullan *et al.* (1992), we ignored the influence of the evaporating plasma on the loop oscillations, since the characteristic time it takes for the loop to be filled with a hot plasma τ considerably exceeds their period P. Indeed, taking $P = 10–30$ s and the loop length $L = 10^{10}$ cm and assuming the velocity of the evaporating plasma to be comparable to the speed of sound, $v_e = (1–3) \times 10^7$ cm s^{-1}, we obtain $\tau \approx L/(2v_e) = 3–8$ min, i.e., $\tau \gg P$.

In conclusion, we would like to note that the minute oscillations of the optical emission from flare stars with a modulation depth no larger than a few percent observed in certain cases can still be generated by the kink modes of coronal loops. However, the centrifugal force that arises from the motion of high-velocity flows of evaporating chromospheric matter along the curved magnetic field lines is most likely responsible for their excitation (Zaĭtsev and Stepanov 1989). We hope to consider this question in more detail in our next paper.

ACKNOWLEDGMENTS

This work was supported by the Russian Foundation for Basic Research (project nos. 03-02-17218 and 03-02-17357), State Foundation for Natural Sciences of China RFBR (project no. 04-02-39029GFEN2004a), the *Astronomy* State Science and Technology Program, the *Nonstationary Phenomena in Astronomy* Program, and by the Department of Physical Sciences of the Russian Academy of Sciences, Program no. 18.

Yu.G. Kopylova thanks the Administration of St. Petersburg for financial support (project PD04-1.9-35).

APPENDIX

We model a coronal loop in the form of an axisymmetric magnetic tube with $\mathbf{B}_0 = (0, 0, B_z(r))$. Let us assume that the system was disturbed from the equilibrium, i.e., $\mathbf{v} = \mathbf{v}'$, $\rho = \rho_0 + \rho'$, $p = p_0 + p'$, $\mathbf{B} = B_z\mathbf{e}_z + \mathbf{B}'$, where we use the standard notation, and the subscript and the prime denote, respectively, the equilibrium and perturbed quantities, with the latter being proportional to $\delta f(r)\exp(-i\omega t + in\varphi + ikz)$. The linearized system of equations of ideal MHD can then be reduced to

$$-i\omega\rho_0\delta v_r = -\frac{\partial}{\partial r}\left(\delta p + \frac{\delta B_z B_z}{4\pi}\right) + \frac{ikB_z}{4\pi}\delta B_r, \quad \text{(A.1)}$$

$$-i\omega\rho_0\delta v_\varphi = \frac{in}{r}\left(\delta p + \frac{\delta B_z B_z}{4\pi}\right) + \frac{ikB_z}{4\pi}\delta B_\varphi, \quad (A.2)$$

$$\omega\rho_0\delta v_z = k\delta p, \quad (A.3)$$

$$\delta B_r = -\frac{kB_z}{\omega}\delta v_r, \quad (A.4)$$

$$\delta B_\varphi = -\frac{kB_z}{\omega}\delta v_\varphi, \quad (A.5)$$

$$-i\omega\delta B_z = -\frac{1}{r}\frac{\partial}{\partial r}rB_z\delta v_r - \frac{inB_z}{r}\delta v_\varphi, \quad (A.6)$$

$$i\omega\delta\rho = \frac{1}{r}\frac{\partial}{\partial r}r\rho_0\delta v_r + \frac{in}{r}\rho_0\delta v_\varphi + ik\rho_0\delta v_z, \quad (A.7)$$

$$\delta p = c_s^2\delta\rho, \quad (A.8)$$

where $c_s^2 = \gamma p_0/\rho_0$ is the speed of sound. In particular, when the radial and longitudinal velocity vector components are $\delta v_r = \delta v_z = 0$ and the perturbation amplitude of the total pressure is $\delta P = \delta p + \delta B_z B_z/4\pi = 0$, we can easily derive the dispersion relation for the torsional modes $\omega = kv_A$ from (A.1)–(A.8).

Generally, the system of equations that was first derived by Hain and Lüst (1958) follows from Eqs. (A.1)–(A.8):

$$i\rho_0(\omega^2 - k^2v_A^2)\frac{1}{r}\frac{\partial}{\partial r}(r\delta v_r) = \omega\left(\mu^2 - \frac{n^2}{r^2}\right)\delta P, \quad (A.9)$$

$$\omega\frac{\partial\delta P}{\partial r} = i\rho_0(\omega^2 - k^2v_A^2)\delta v_r, \quad (A.10)$$

where $v_A = \sqrt{B_z^2/4\pi\rho_0}$ is the Alfvén speed,

$$\mu^2 = \frac{(k^2c_s^2 - \omega^2)(\omega^2 - k^2v_A^2)}{(v_A^2 + c_s^2)(k^2c_T^2 - \omega^2)}, \quad (A.11)$$

$$c_T^2 = \frac{v_A^2c_s^2}{v_A^2 + c_s^2}.$$

According to (A.2) and (A.5), we have

$$\delta v_\varphi = \frac{n\omega\delta P}{r\rho_0(k^2v_A^2 - \omega^2)}. \quad (A.12)$$

As follows from (A.3) and (A.8),

$$\frac{\delta\rho}{\rho_0} = \frac{\omega}{kc_s}\frac{\delta v_z}{c_s}. \quad (A.13)$$

Using (A.7), (A.9), (A.12), and (A.13), we then find that

$$\delta v_z = \frac{kc_s^2\omega}{\rho_0}\frac{\delta P}{(v_A^2 + c_s^2)(k^2c_T^2 - \omega^2)}. \quad (A.14)$$

Using (A.9) and (A.14), we obtain from (A.13)

$$\frac{\delta\rho}{\rho_0} = ir\frac{\omega(\omega^2 - k^2v_A^2)}{(v_A^2 + c_s^2)(k^2c_T^2 - \omega^2)(\mu^2r^2 - n^2)}\frac{\partial}{\partial r}(r\delta v_r). \quad (A.15)$$

The dispersion relation for the kink modes ($n = 1$) is (Tsap and Kopylova 2001)

$$\omega^2 = k^2\frac{\rho_i v_{A_i}^2 + \rho_e v_{A_e}^2}{\rho_i + \rho_e}. \quad (A.16)$$

Since the plasma parameter under solar coronal conditions is $\beta \approx c_s^2/v_A^2 \ll 1$, $\rho_i \gg \rho_e$, and, in addition, $v_{r_i} \propto r$ inside the loop (Tsap and Kopylova 2001), we find using (A.15) and (A.16) that

$$\left|\frac{\delta\rho_i}{\rho_i}\right| \approx (kr)\frac{\delta v_r}{v_f}, \quad (A.17)$$

where $v_f \approx \omega/k \approx v_{A_i}$. for the kink modes, $ka \ll 1$; therefore, the density amplitude $\delta\rho$, according to (A.17), has the second order of smallness relative to ρ_0.

Using (A.3) and (A.6)–(A.8), we can easily derive the equality

$$\frac{\delta B_z}{B_z} = \frac{\omega^2 - k^2c_s^2}{\omega kc_s^2}\delta v_z. \quad (A.18)$$

According to (A.4), (A.10), (A.14), and (A.18), we then have

$$\frac{\delta B_z}{\delta B_r} = \frac{\omega^2 - k^2v_A^2}{kv_A^2}\frac{\delta P}{\delta P'}, \quad (A.19)$$

where $\delta P' = \partial\delta P/\partial r$. Since $\delta P/\delta P' \approx r$ (Tsap and Kopylova 2001), we obtain from (A.16) and (A.19)

$$\frac{\delta B_z}{\delta B_r} \approx kr. \quad (A.20)$$

Using similar reasoning, we can also easily show that $\delta B_\varphi/\delta B_r \sim 1$. Consequently, since $r \le a$, i.e., $kr \ll 1$, for the inner part of the loop, we obtain the following from (A.20): $\delta B_z \ll \delta B_r, \delta B_\varphi$.

For the sausage FMA modes, for which $v_{r_i} \propto J_1(\mu r)$ (Kopylova *et al.* 2002), where J_1 is the Bessel function of the first kind and $\omega \approx v_{A_i}/a$, we can make sure that the following relation is valid:

$$\frac{\delta\rho}{\rho_0} \approx \frac{\delta B_z}{B_z} \approx \frac{\delta v_r}{v_{A_i}}.$$

REFERENCES

1. A. D. Andrews, Astron. Astrophys. **227**, 456 (1990).
2. M. J. Aschwanden, in *Proceedings of NATO Advanced Research Workshops*, Ed. by R. von Fay Siebenburgen, K. Petrovy, B. Roberts, and M. J. Aschwanden (Kluwer, Dordrecht, 2003), NATO Sci. Ser. II, p. 22.

3. M. J. Aschwanden, L. Fletcher, C. J. Schrijver, and D. Alexander, Astrophys. J. **520**, 880 (1999).
4. P. M. Bellan, Phys. Plasmas **1**, 3523 (1994).
5. A. O. Benz, J. E. Conway, and M. Güdel, Astron. Astrophys. **331**, 596 (1998).
6. S. I. Braginskiĭ, Vopr. Teor. Plazmy **1**, 183 (1963).
7. Q. R. Chen and M. D. Ding, Astrophys. J. **618**, 537 (2005).
8. C. Fang and M. D. Ding, Astron. Astrophys. **110**, 99 (1995).
9. R. E. Gershberg, *Activity of Solar-Type Main-Sequence Stars* (Astroprint, Odessa, 2002) [in Russian].
10. V. A. Ginzburg, *Propagation of Electromagnetic Waves in Plasma* (Pergamon Press, Oxford, 1970).
11. M. Goossens, A. De Groof, and J. Andries, in *Proceedings of the SOLMAG: Magnetic Coupling of the Solar Atmosphere Euroconference and IAU Coll. No. 188*, Ed. by H. Sawaya-Lacoste (ESA Publ. Division, Noordwijk, 2002), ESA SP-505, p. 137.
12. V. P. Grinin, V. M. Loskutov, and V. V. Sobolev, Astron. Zh. **70**, 350 (1993) [Astron. Rep. **37**, 182 (1993)].
13. K. Hain and R. Lüst, Z. Naturforsh. A **13**, 936 (1958).
14. B. M. Haisch, in *Proceedings of the 71st Colloquium "Activity in Red–Dwarf Stars,"* Ed. by P. B. Byrne and M. Rodono (Reidel, Dordrecht, 1983), p. 255.
15. S. L. Hawley, G. H. Fisher, T. Simon, *et al.*, Astrophys. J. **453**, 464 (1995).
16. J. V. Hollweg, Astrophys. J. **277**, 392 (1984).
17. J. Ionson, Astrophys. J. **276**, 357 (1984).
18. Yu. G. Kopylova, A. V. Stepanov, and Yu. T. Tsap, Pis'ma Astron. Zh. **28**, 870 (2002) [Astron. Lett. **28**, 783 (2002)].
19. M. Mathioudacis, J. H. Seiradakis, D. R. Williams, *et al.*, Astron. Astrophys. **403**, 1101 (2003).
20. S. A. Matthews, L. van Driel-Gesztelyi, H. S. Hudson, and N. V. Nitta, Astron. Astrophys. **409**, 1107 (2003).
21. T. R. Metcalf, D. Alexander, H. S. Hudson, and D. W. Longcope, Astrophys. J. **595**, 483 (2003).
22. D. J. Mullan, Astrophys. J. **204**, 530 (1976).
23. D. J. Mullan, Astrophys. J. **282**, 603 (1984).
24. D. J. Mullan, R. B. Herr, and S. Bhattacharyya, Astrophys. J. **391**, 265 (1992).
25. V. M. Nakariakov, V. F. Melnikov, and V. E. Reznikova, Astron. Astrophys. **412**, L7 (2003).
26. W. M. Neupert, Astrophys. J. **153**, L59 (1968).
27. M. R. Pestalozzi, A. O. Benz, J. E. Conway, and M. Güdel, Astron. Astrophys. **353**, 569 (2000).
28. E. R. Priest, *Solar Magnetohydrodynamics* (Reidel, Dordrecht, 1982; Mir, Moscow, 1985).
29. F. Reale, in *Stellar Coronae in the Chandra and XMM–Newton Era*, Ed. by F. Favata and J. J. Drake (Astron. Soc. Pac., San Francisco, 2002); Astron. Soc. Pac. Conf. Ser. **277**, 103 (2002).
30. B. Roberts, Sol. Phys. **193**, 139 (2000).
31. B. Roberts, in *Proceedings of SOHO 13–Waves, Oscillations, and Small-Scale Transient Events in the Solar Atmosphere: A Joint View from SOHO and TRACE*, Ed. by H. Lacoste (ESA Publ. Division, Noordwijk, 2004), ESA SP-547, p. 1.
32. B. Roberts, P. M. Edwin, and A. O. Benz, Astrophys. J. **279**, 857 (1984).
33. M. Rodono, Astron. Astrophys. **32**, 337 (1974).
34. M. S. Ruderman and B. Roberts, Astrophys. J. **577**, 475 (2002).
35. J. H. M. M. Schmitt and F. Favata, Nature **401**, 44 (1999).
36. K. Shibasaki, Astrophys. J. **557**, 326 (2001).
37. A. V. Stepanov, Yu. G. Kopylova, Yu. T. Tsap, *et al.*, Pis'ma Astron. Zh. **30**, 530 (2004) [Astron. Lett. **30**, 480 (2004)].
38. A. V. Stepanov and Yu. T. Tsap, Astron. Rep. **43**, 838 (1999).
39. A. V. Stepanov and Y. T. Tsap, Sol. Phys. **221**, 135 (2002).
40. Yu. T. Tsap and Yu. G. Kopylova, Pis'ma Astron. Zh. **27**, 859 (2001) [Astron. Lett. **27**, 737 (2001)].
41. Y. Xu, W. Cao, C. Liu, *et al.*, Astrophys. J. **607**, L131 (2004).
42. V. V. Zaitsev and A. V. Stepanov, Pis'ma Astron. Zh. **8**, 248 (1982) [Sov. Astron. Lett. **8**, 132 (1982)].
43. V. V. Zaitsev and A. V. Stepanov, Pis'ma Astron. Zh. **15**, 154 (1989) [Sov. Astron. Lett. **15**, 66 (1989)].
44. B. E. Zhilyaev, Ya. O. Romanyuk, I. A. Verlyuk, *et al.*, Astron. Astrophys. **364**, 641 (2000).

Translated by V. Astakhov

Astronomy Letters, Vol. 31, No. 9, 2005, pp. 620–626. Translated from Pis'ma v Astronomicheskiĭ Zhurnal, Vol. 31, No. 9, 2005, pp. 693–700.

Electron Acceleration by Electric Fields Near the Footpoints of Current-Carrying Coronal Magnetic Loops

V. V. Zaitsev*

Institute of Applied Physics, Russian Academy of Sciences, ul. Ul'yanova 46, Nizhni Novgorod, 603950 Russia

Received March 15, 2005

Abstract—We analyze the electric fields that arise at the footpoints of a coronal magnetic loop from the interaction between a convective flow of partially ionized plasma and the magnetic field of the loop. Such a situation can take place when the loop footpoints are at the nodes of several supergranulation cells. In this case, the neutral component of the converging convective flows entrain electrons and ions in different ways, because these are magnetized differently. As a result, a charge-separating electric field emerges at the loop footpoints, which can efficiently accelerate particles inside the magnetic loop under appropriate conditions. We consider two acceleration regimes: impulsive (as applied to simple loop flares) and pulsating (as applied to solar and stellar radio pulsations). We have calculated the fluxes of accelerated electrons and their characteristic energies. We discuss the role of the return current when dense beams of accelerated particles are injected into the corona. The results obtained are considered in light of the currently available data on the corpuscular radiation from solar flares. © *2005 Pleiades Publishing, Inc.*

Key words: *Sun, solar corona, magnetic loops, electron acceleration.*

INTRODUCTION

Much of the energy in solar and stellar flares is released in the form of energetic particles. The bulk of the electrons and ions in impulsive solar flares are accelerated to energies of 100 keV and 100 MeV, respectively (Miller *et al.* 1997) and produce hard X-ray and gamma-ray line emission. In addition, the continuum gamma-ray emission and the occasionally observed emission from neutral pions suggest that the electron and ion energies in flares can reach 10 MeV and 1 GeV, respectively. If the hard X-ray emission in flares were assumed to arise from the bremsstrahlung of fast electrons in the chromosphere (the nonthermal thick-target model) (Emslie *et al.* 1981; McClymont and Canfield 1986; Canfield and Gayley 1987; Mariska *et al.* 1989), then an impulsive solar flare would produce $\sim 10^{37}$ electrons with energies >20 keV per second during 10–100 s. This implies that the rate of energy release in the form of accelerated electrons is $\dot{E}_e \approx 3 \times 10^{29}$ erg s^{-1} during 100 s, which corresponds to a total electron energy $E_e(>20\ \text{keV}) \approx 3 \times 10^{31}$ erg at a total number of accelerated electrons $N_e(>20\ \text{keV}) \approx 10^{39}$.

The requirements imposed on the acceleration rate are slightly reduced if it is assumed that the hard X-ray spectrum at energies <30 keV is determined by the emission of a hot ($\sim 3 \times 10^7$ K) plasma and that the emission at high energies is generated by fast electrons with a power-law spectrum. This constitutes the content of the hybrid thermal/nonthermal (T/NT) model (Holman and Benka 1992). In this case, the required production rate of electrons with energies >20 keV decreases to $\dot{N}_e \approx 2 \times 10^{35}$ el. s^{-1} at a duration of the process $\sim$100 s, which yields $N_e(>20\ \text{keV}) \approx 2 \times 10^{37}$ el., $\dot{E}_e(>20\ \text{keV}) \approx 6 \times 10^{27}$ erg s^{-1}, and $E_e(>20\ \text{keV}) \approx 6 \times 10^{29}$ erg.

Bearing in mind a good correlation between impulsive flares and coronal magnetic loops, we will consider the acceleration of electrons by the large-scale electric fields generated by convective motions of photospheric plasma at the footpoints of a coronal magnetic loop by assuming that other acceleration mechanisms are also relaized under solar coronal conditions. The large-scale electric fields in coronal magnetic loops arise when the loop footpoints are at the nodes of several supergranulation cells. In this case, the converging convective plasma flows interact with the magnetic field at the loop footpoints to generate a charge-separating electric field, which can efficiently accelerate particles under certain conditions. The loop can contain a fairly large store of energy, up to $10^{32} - 10^{33}$ erg, and can provide the energy release of an intense flare. This energy is concentrated in the form of a nonpotential part of the magnetic field that arises from the existence in the loop of an electric current up to $\sim 3 \times 10^{12}$ A generated by photospheric

*E-mail: za130@appl.sci-nnov.ru

1063-7737/05/3109-0620$26.00

convection and flowing along the loop (Zaitsev and Stepanov 1992; Zaitsev and Khodachenko 1997). In the next section, we discuss the most likely location of the acceleration region in a magnetic loop. Subsequently, we consider the acceleration mechanism and calculate the fluxes of accelerated electrons. We also consider the impulsive (as applied to simple flares) and pulsating (as applied to solar and stellar radio pulsations) acceleration regimes. We discuss the neutralization of the electric current produced by accelerated electrons. In conclusion, we formulate our main results.

THE ACCELERATION REGION: THE CHROMOSPHERE OR THE CORONA?

A fairly large number of particles must be injected into the acceleration regime to provide the fluxes of fast electrons observed during impulsive flares. What is the reservoir of these particles if the acceleration takes place in a flare magnetic loop? The total number of electrons in a flare loop with a plasma density of 10^{10} cm^{-3}, a cross-sectional area of 10^{18} cm^2, and a length of $(1-5)\times 10^9$ cm is $(1-5)\times 10^{37}$ el. If it is considered that any plausible acceleration mechanism in plasma accelerates only a minor fraction of particles, then the estimated total number of electrons contained in the coronal part of a flare loop is evidently too small to provide acceleration even in the most favorable case of the hybrid model ($\sim 2\times 10^{37}$ el.).

There are two important sources in a magnetic loop that can, in principle, provide the required number of particles. The parts of the loop near its footpoints in the chromosphere constitute the first source. In the chromospheric part of the loop, $\sim 5\times 10^{40}$ particles are contained in the column from the temperature minimum to the chromosphere–corona transition region if the cross-sectional area of the loop in this region is assumed to be $\sim 10^{18}$ cm^2. If the acceleration takes place in the chromospheric part of the loop, then the above number of particles is large enough to provide the injection of the required number of electrons into the acceleration regime.

The second possibility of particle enrichment of a flare magnetic loop arises when it interacts with prominences (Zaitsev and Stepanov 1991, 1992). In this case, the flare process can be triggered by the flute instability that grows at the loop top and that causes the dense prominence plasma to penetrate into the current channel of the magnetic loop. The number of particles supplied by a prominence in the flare time, $t_{\rm f}\sim 100$ s, can be estimated as $N\approx 2\pi r r_{\rm f} n_{\rm p} V_{\rm p} t_{\rm f}$, where $r_{\rm f}$ is the thickness of the prominence "tongue" penetrating into the current channel, $r\approx 10^8$ cm is the loop half-thickness, $n_{\rm p}\approx 10^{12}$ cm^{-3} is the plasma density in the prominence, and $V_{\rm p}\approx V_{\rm Ti}\approx 2\times 10^6$ cm s^{-1} is the characteristic plasma inflow velocity in the current channel of the loop, which is approximately equal to the thermal ion velocity at a prominence temperature of $\sim 5\times 10^4$ K. At these parameters, we obtain $N\approx 3\times 10^{38}$ el. This value is approximately an order of magnitude larger than that required for the hybrid T/NT model, but it is severalfold smaller than that required by the nonthermal thick-target model. It thus follows that, to satisfy the demand of the acceleration mechanisms for particles during the most intense flares, the preferred location of the acceleration region is the chromospheric part of the coronal loop. For flares with moderate energy release, the acceleration region can be located near the loop top, where the required store of particles is provided by the plasma flow from a prominence (if it exists).

THE FLUXES OF ACCELERATED ELECTRONS

Many acceleration mechanisms have been suggested to explain the generation of fast particles during flares. These can be arbitrarily divided into three main classes: (1) stochastic wave acceleration, (2) shock acceleration, and (3) direct acceleration in quasi-stationary electric fields. The most efficient way for particle acceleration in the region of flare energy release is the direct acceleration by an electric field, where the large-scale electric field E of the flare magnetic loop acts as the latter. It is important that, if there is a magnetic field $\mathbf{B}$ in plasma, with $|\mathbf{B}|>|\mathbf{E}|$, then only the electric field component along the magnetic field, $E_{||}=\mathbf{EB}/B$, will accelerate particles. If $E_{||}$ is smaller than the Dreicer electric field $E_{\rm D}=e\Lambda\omega_{\rm p}^2/V_{\rm T}^2$, then electrons with velocities $V>(E_{\rm D}/E_{||})^{1/2}V_{\rm T}$, where $V_{\rm T}$ is the thermal electron velocity, Λ is the Coulomb logarithm, and $\omega_{\rm p}$ is the Langmuir frequency, become involved in the acceleration process (runaway). The kinetic theory yields the following formula for the electron acceleration rate (Knoepfel and Strong 1979):

$$\dot{N}_{\rm e}=0.35 n\nu_{\rm ei}V_{\rm a}x^{3/8}\exp\left(-\sqrt{2x}-\frac{x}{4}\right), \quad (1)$$

where $x=E_{\rm D}/E_{||}$, $V_{\rm a}$ is the volume of the acceleration region, $\nu_{\rm ei}=5.5n\Lambda/T^{3/2}$ is the effective electron–ion collision frequency, n is the plasma electron density, and T is the temperature. In the coronal part of a magnetic loop even with a large electric current, $I=10^{12}$ A; and typical parameters, $n=10^{10}$ cm^{-3}, a half-thickness of $r=5\times 10^8$ cm, and $T=10^6$–10^7 K—the electric field attributable to

a finite plasma conductivity is too weak to produce any appreciable acceleration, ($x = E_D/E_{||} > 200$). The strongest electric fields are generated in the dynamo region at the footpoints of a magnetic loop, where the charges are efficiently separated through a convective flow of photospheric matter into the flux tube and different electron and ion magnetizations. We will estimate the acceleration efficiency using the self-consistent model of a vertical, homogeneous (in height) cylindrical tube with a magnetic field $\mathbf{B} = (0, B_\varphi(r), B_z(r))$, an electric field $\mathbf{E} = (E_r(r), 0, 0)$, and a radially converging plasma flow $V_r(r)$ (Khodachenko and Zaitsev 2002) as an example. The other two velocity components in this model, $V_\varphi(r)$ and $V_z(r)$, can be determined from the continuity equation and do not lead to the generation of azimuthal and vertical electric fields. The photospheric emf maintains the required potential difference and the electric current in the "coronal magnetic loop–photosphere" electric circuit (Zaitsev *et al.* 1998). More general models of magnetic flux tubes in the dynamo region, including the radial divergence, were considered by Henoux and Somov (1991). As was noted above, only the radial charge-separating electric field component in our model of a vertical cylindrical tube with a radial converging plasma flow approximates the part of the actual flux tube located near the photospheric footpoints. Since this component is perpendicular to the magnetic field of the stationary tube (B_φ, B_z), there is no acceleration by the charge-separating electric field under stationary conditions. Acceleration arises when the magnetic field of the tube is deformed in such a way that the radial magnetic field B_r appears. In this case, the electric field component along the magnetic field is (Zaitsev and Khodachenko 1997)

$$E_{||} \approx \frac{1-F}{2-F}\frac{\sigma V_r B^2}{enc^2(1+\alpha B^2)}\frac{B_r}{B}. \qquad (2)$$

Here, the radial magnetic field $B_r \ll B$, $F = n_a m_a/(n_a m_a + n m_i)$ is the relative density of neutral particles, $\sigma = e^2 n/m_e(\nu_{ei} + \nu_{ea})$ is the Coulomb conductivity, $\alpha = \sigma F^2/(2-F)c^2 n m_i \nu_{ia}$, ν_{jk} is the effective collision frequency between a particle of type j and a particle of type k, and V_r is the radial velocity of the convective plasma motion at the loop footpoints. The particle acceleration associated with the charge-separating electric field can arise, for example, during the growth of a flute instability at the footpoints of a magnetic flux tube (see below), when the plasma tongue penetrating into the current channel at velocity v_r is inhomogeneous in height.

In this case, it can be shown that a radial magnetic field

$$B_r = B\frac{\partial}{\partial z}\int_0^t v_r(t')\mathrm{d}t'$$

is generated, and an accelerating electric field $E_{||}$ arises. $E_{||}$ increases when the magnetic loop footpoints is heated, since heating causes an increase in σ and a decrease in α. In this case, the relative density of neutral particles F decreases. Under significant heating, when there is almost total ionization ($F \ll 1$), we may assume that $\alpha B^2 \ll 1$. Expression (2) then takes a simple form:

$$E_{||} \approx \frac{1}{2}\frac{V_r}{c}B\left(\frac{\omega_e}{\nu_{ei}}\right)\frac{B_r}{B}, \quad \alpha B^2 \ll 1.$$

In the opposite limiting case, expression (2) takes the form

$$E_{||} \approx \frac{1-F}{F^2}\frac{m_i V_r \nu_{ia}}{e}\frac{B_r}{B}, \quad \alpha B^2 \gg 1.$$

At $V_r < 0$ (the convective flow is directed into the tube), the component $E_{||}$ is directed downward and accelerates electrons toward the corona and ions toward the photosphere; i.e., energetic ions and electrons will move toward different loop footpoints. This can lead to a situation where the gamma-ray emission attributable to energetic ions will emanate from one of the loop footpoints and the X-ray emission associated with fast electrons will emanate from the other footpoint.

In the case of strong heating of the tube footpoints, where $\alpha B^2 \ll 1$, the ratio $x = E_D/E_{||}$ is defined by the formula

$$\frac{E_D}{E_{||}} \simeq 7.7\times 10^{-5}\frac{n^2}{B^2 V_r T^{5/2}}\left(\frac{\Lambda}{20}\right)^2\frac{B}{B_r} \qquad (3)$$
$$\simeq 2.6\left(\frac{n}{10^{15}}\right)^2\left(\frac{B}{10^3}\right)^{-2}\left(\frac{V_r}{3\times 10^4}\right)^{-1}$$
$$\times\left(\frac{T}{10^6}\right)^{-5/2}\left(\frac{\Lambda}{20}\right)^2\frac{B}{B_r}.$$

Note that x depends strongly on the temperature and the magnetic field, which can vary over a wide range in the dynamo region. It follows from (3) that the accelerating electric field at $B_r \approx 0.1B$ can reach or even exceed the Dreicer field if the loop footpoints are heated to a temperature of 3.5×10^6 K. In this case, all electrons become involved in the runaway process, while the electric field reaches 17 V cm^{-1}. This enables the particles on a scale of $\sim 10^8$ cm to gain an extremely high energy, ~ 1 GeV. The peculiarities of the electron acceleration in super-Dreicer electric fields were considered by Litvinenko (1996).

Extreme electric fields emerge at the maximum possible magnetic fields, $\sim 10^3$ G, and strong heating of the photospheric footpoints of a magnetic loop, which, certainly, is realized not in all flares. However, this demonstrates the ability of current-carrying magnetic loops to efficiently accelerate particles. In the case of acceleration at the chromospheric loop footpoints, the production rate of energetic electrons exceeds 10^{35} el. s^{-1}; this is enough for the hybrid T/NT model if we take $n = 10^{11}$ cm^{-3} in the acceleration region, the tube radius 10^8 cm, $T = 10^5$ K, and the height of the acceleration region $h = 10^8$ cm. In this case, $x = E_D/E_{||} = 26$, $E_{||} = 2.15 \times 10^{-3}$ V cm^{-1}, and the energy of the bulk of accelerated electrons is 200 keV. At the parameters of the acceleration region chosen as an example, the losses through optical emission from this region are 2×10^{25} erg s^{-1}, which is much smaller than the mean flare power. Therefore, it may be assumed that a flare can provide the heating required for the needed acceleration rate.

IMPULSIVE AND PULSATING ACCELERATION REGIMES

The appearance of a radial magnetic field at the footpoints of a magnetic loop where a strong charge-separating electric field is localized may be attributable not only to the growth of a flute instability here, but also to the excitation of loop eigenmodes. In the former case, the acceleration is apparently impulsive, because the flute instability is aperiodic. In the latter case, a pulsating acceleration regime is possible, which often manifests itself after a flare in the form of quasi-periodic sequences of type-III radio bursts.

Impulsive Acceleration

When a magnetic flux tube goes out from the photosphere into the chromosphere, it expands due to a decrease in the ambient pressure; therefore, a magnetic field curvature directed into the tube appears. A value on the order of the scale height of an inhomogeneous atmosphere can be taken as an estimate of the radius of curvature,

$$R_c \approx \frac{k_B T}{\mu m_H g},$$

where k_B is the Boltzmann constant, m_H is the mass of the hydrogen atom, μ is the mean molecular weight, and g is the gravity. A centrifugal force appears due to the magnetic field curvature,

$$\mathbf{f}_c = \frac{2nk_B T}{R_c^2}\mathbf{R}_c;$$

this force acts on plasma with a density of $\rho = (n + n_a)m_H$. Therefore, the effective centrifugal acceleration acting on the chromospheric plasma surrounding the magnetic flux tube near its footpoints is

$$\mathbf{g}_c = \frac{\mathbf{f}_c}{\rho} = \frac{2gn}{(n+n_a)m_H}\frac{\mathbf{R}_c}{R_c^2}.$$

In the case under consideration, the condition for the flute instability of the ballooning mode is

$$g_c - g\cos\Theta \geq 0,$$

where Θ is the angle between the direction of the radius of curvature $\mathbf{R}_c$ and the vertical.

When $\mathbf{R}_c$ is almost perpendicular to g, the growth time of the ballooning mode of the flute instability is

$$\tau_b \approx \frac{1}{2}\frac{\lambda}{\pi g}\left(\frac{n}{n+n_a}\right)^{-1/2}, \quad (4)$$

where λ is the wavelength of the disturbance. Estimate (4) corresponds to the most unstable case where the wave vector of the disturbances is perpendicular to the magnetic field (Priest 1982).

When $n_a \ll n$,

$$\tau_b \approx 2 \times 10^{-3}\lambda^{1/2} \quad (5)$$

and the disturbances with a wavelength $\lambda \approx R_c$ at $T = 10^5$ K grow in a time of $\sim$35 s. In this time, the tube-surrounding plasma penetrates inward, generating a radial magnetic field, which gives rise to the component of the charge-separating electric field along the magnetic field that is responsible for the particle acceleration. To a first approximation, time (5) can be taken as the characteristic duration of the impulsive acceleration phase.

A decrease in the radial convection velocity due to an increase in the gas pressure inside the tube as the flare process develops or the stoppage of the flute of ambient plasma penetrating into the magnetic loop could be responsible for the termination of the acceleration process. It should be noted that time (5) is equal in order of magnitude to the duration of simple impulsive flares (10–100 s). At the above plasma parameters in the acceleration region, the total number of electrons accelerated at the footpoints of a current-carrying magnetic flux tube in time (5) is $N_e(>200\ \text{keV}) \approx \dot{N}_e\tau_b \approx 3.5 \times 10^{36}$ el., which is large enough to explain the observed efficiency of the acceleration mechanism in terms of the T/NT model for the generation of hard X-ray emission from impulsive solar flares (Holman and Benka 1992).

Pulsating Acceleration

The presence of broadband periodic pulsations in solar type-IV radio bursts suggests that a pulsating regime of electron acceleration occasionally arises immediately after flares; this regime is characterized by a much lower production rate of fast electrons, but usually lasts much longer than the main flare. One example of such events, on October 25, 1994, was investigated by Aurass *et al.* (2003). Based on a combined analysis of spectral and heliographic radio data as well as optical and X-ray data, these authors reconstructed the spatial structure of the radio pulsation source, which turned out to be a coronal magnetic loop. Electrons were periodically injected at velocities of $\sim 0.3\ c$ from the loop footpoint with a stronger magnetic field and subsequently moved along the trap axis, generating a sequence of type-III bursts with a rapid frequency drift. The pulsation period was, on average, 1.33 s, while the duration of the pulsating phase was about 3.5 min; i.e., the pulsations had a high Q factor. Analysis of the efficiency of the acceleration mechanism for this event has shown (Zaitsev *et al.* 2005) that the mean rate of electron acceleration in pulsations is approximately three orders of magnitude lower than that during a moderate-intensity solar flare, $3 \times 10^{32}\ \mathrm{s}^{-1}$. Pulsations are also found in the radio emission from flares on late-type stars. For example, a spectral analysis of the low-frequency modulation of the microwave emission from the flare of May 19, 1997, on the star AD Leo revealed two regular components in its radio spectrum: a periodic modulation whose frequency decreased smoothly during the flare from ≈ 2 Hz to ≈ 0.2 Hz and a periodic sequence of pulses with a repetition frequency of about 2 Hz (Zaitsev *et al.* 2004). The rapid negative frequency drift of the radio pulsations in this flare (Stepanov *et al.* 2001) is indicative of a periodic acceleration of particles in the lower atmosphere followed by their injection into the stellar corona. A detailed analysis of this event led us to conclude that the radio emission source in this case is a current-carrying magnetic loop, while the pulsations with a gradually decreasing repetition frequency are attributable to the excitation of loop eigenmodes as an equivalent (LRC) electric circuit with the frequency (see Zaitsev *et al.* 2004)

$$\nu_{\mathrm{LRC}} \approx \frac{1}{\sqrt{\pi\chi}} \left[1 + \left(\frac{cr_0 B_z}{2I_z}\right)^2\right]^{1/2} \frac{I_z}{2cr_0^2\sqrt{\pi n m_{\mathrm{i}}}}, \quad (6)$$

where

$$\chi = \ln\frac{4l}{\pi r_0} - \frac{7}{4},$$

I_z is the total electric current flowing along the loop through its cross-section, c is the speed of light, r is the minor radius (half-thickness) of the loop, B_z is the magnetic field strength along the loop axis, and l is the length of the coronal part of the loop. For simplicity, the magnetic loop in the coronal part is assumed to be homogeneous, with a mean plasma density n inside the loop. Frequency (6) depends on the current, because the equivalent capacitance of the loop is determined by the Alfvén velocity, which depends not only on the z component, but also on the φ component of the magnetic field in the loop. The oscillations of a coronal magnetic loop as an equivalent electric circuit were considered by Zlotnik *et al.* (2003) as a possible cause of the appearance of radio pulsations in solar type-IV radio bursts. The high Q factor of the observed pulsations, which is ensured by the loop parameters in the case under consideration, while the Q factor of the MHD eigenmodes of the loop is fairly low under coronal conditions, is an argument for this conclusion. We have already noted above that the efficiency of the pulsating electron acceleration regime at the post-flare phase of development of the active region estimated for the event of October 25, 1994, is approximately three or four orders of magnitude lower than the mean one for the impulsive solar flare phase. The energy of the accelerated electrons in this event (about 40 keV) was approximately equal to the characteristic energy of the fast electrons accelerated at the impulsive phase. As we see from Eqs. (1) and (3), such a situation arises when the geometrical sizes (volume) of the acceleration region decrease significantly, while the parameters of the acceleration process (T, n, B, B_r, V_r) are approximately constant.

THE CURRENT OF ACCELERATED ELECTRONS

Another important question is being discussed in the literature in connection with the large electric current associated with accelerated electrons (Melrose 1991, 1995). If the efficiency of the acceleration mechanism is $\mathrm{d}N_{\mathrm{e}}/\mathrm{d}t \geq 10^{35}$ el. s^{-1}, then an electric current $I = e\dot{N}_{\mathrm{e}} \geq 1.6 \times 10^{15}$ A will arise. If this current flows in a magnetic loop with a cross-section of $\sim 10^{18}\ \mathrm{cm}^2$, then an induced magnetic field $B \geq 6 \times 10^6$ G, which is actually not observed in coronal structures, will correspond to these values of the current. Two possibilities for eliminating this contradiction are commonly considered.

The first possibility is related to the assumption about filamentation of the current of accelerated electrons, i.e., about a breakup of the current channel into a set of current filaments with oppositely directed currents in neighboring filaments; as a result, the

total magnetic field of the current channel does not exceed the observed value (Holman 1985; Van der Oord 1990). However, it is unclear how a system of filaments with oppositely directed currents can arise in a beam of electrons flying apart. As was shown by Fadeev *et al.* (1965), current filamentation is indeed possible under certain conditions; in this case, however, the current direction is not reversed in neighboring filaments, and we do not get rid of the problem of the generation of strong magnetic fields on the periphery of the current channel.

The other possibility is related to the formation of a return current in plasma (Hammer and Rostoker 1970; Cox and Bennet 1970; Lee and Sudan 1971; Lovelace and Sudan 1971). Let, for example, an electron beam with radius r_0 is injected into a plasma along the z axis of an external magnetic field. The field B_φ at each fixed point of the plasma will then change with time during the passage of the beam front. The change in B_φ gives rise to an electric field E_z at the front of the electron beam that acts on plasma electrons in such a way that a current directed against the injected current emerges. Consequently, the total current decreases until it is completely neutralized. If the radius of the electron beam exceeds the screening length ($r_0 > c/\omega_\mathrm{p}$), then there is no magnetic field at $r > r_0$. The beam current is neutralized by the return plasma current, which flows almost entirely inside the beam. The condition for total neutralization appears as follows: $c/\omega_\mathrm{p} \ll r_0$, $\nu_\mathrm{ei} t < 1$, where t is the time after injection. For $\nu_\mathrm{ei} t \gg 1$, the return current decays, and the neutralization gradually disappears. However, the decay time scale of the return current is determined by the magnetic diffusion time scale $t_\mathrm{D} = \pi\sigma r_0^2/c^2$, which exceeds significantly all of the time scales characteristic of flare processes at r_0 of the order of the loop thickness. Therefore, it may be assumed that the injection of accelerated electrons does not change the external magnetic field. The Lenz law allows the beam of accelerated electrons to propagate in plasma without spending energy on modifying the magnetic field.

CONCLUSIONS

We drew attention to the important role of convective plasma motions in the photospheres and lower chromospheres of the Sun and late-type stars in generating large-scale electric fields and in accelerating particles. The chromospheric footpoints of magnetic loops, where an acceleration rate of $\dot{N}_\mathrm{e} > 10^{35}$ el. s^{-1} at a mean electron energy of $E_\mathrm{e} \geq 100$ keV can be ensured, while energies of $\sim$1 GeV can be reached in the case of strong heating of the loop footpoints, is the preferred acceleration region (from the standpoint of the production rate of fast electrons). A large-scale charge-separating electric field (with a scale length of the order of the loop thickness) emerges at the footpoints of a coronal magnetic loop, because electrons and ions are entrained in different ways by the converging convective flows of photospheric plasma. Such a situation takes place when the loop footpoints are at the nodes of several supergranulation cells. The acceleration process could be triggered by a flute instability for which there are appropriate conditions at the loop footpoints (the magnetic field curvature here is directed into the loop, because the pressure of the surrounding plasma decreases with height). The penetration of the surrounding plasma tongue into the coronal magnetic loop through the flute instability leads to a distortion of the loop magnetic field (to the appearance of a small radial magnetic field component); as a result, a component of the charge-separating electric field along the magnetic field emerges, and an impulsive acceleration process is triggered. In this case, the accelerated electrons and ions move in opposite directions, which can result in the localization of the hard X-ray and gamma-ray emission sources at the opposite loop footpoints if, for example, the loop is asymmetric and the acceleration process arises only at one of the footpoints. The data obtained from the RHESSI satellite suggest that this situation is possible. The injection of accelerated electrons into the coronal part of the loop does not lead to the generation of a strong magnetic field, because the return current neutralizing the current of accelerated electrons emerges.

ACKNOWLEDGMENTS

This work was supported in part by the Russian Foundation for Basic Research (project nos. 05-02-15242a and 03-02-20009), the *Nonstationary Processes in Astronomy* Program of the Presidium of the Russian Academy of Sciences, the *Study of Solar-Wind Disturbance Sources over a Wide Range of Electromagnetic Disturbances* Program of the Department of Physical Sciences of the Russian Academy of Sciences, and the Program for Support of Leading Scientific Schools (NSh-1744.2003.2).

REFERENCES

1. H. Aurass, K. L. Klein, E. Ya. Zlotnik, and V. V. Zaitsev, Astron. Astrophys. **410**, 1001 (2003).
2. R. C. Canfield and K. G. Gayley, Astrophys. J. **322**, 999 (1987).
3. J. D. Cox and W. N. Bennet, Phys. Fluids **13**, 182 (1970).
4. A. G. Emslie, J. C. Brown, and M. T. Machado, Astrophys. J. **246**, 337 (1981).

5. V. M. Fadeev, I. F. Kvartskhava, and N. N. Komarov, Yad. Sint. **5**, 202 (1965).
6. D. A. Hammer and N. Rostoker, Phys. Fluids **13**, 1831 (1970).
7. J. C. Henoux and B. V. Somov, Astron. Astrophys. **241**, 613 (1991).
8. G. D. Holman, Astrophys. J. **293**, 584 (1985).
9. G. D. Holman and S. G. Benka, Astrophys. J. **400**, L79 (1992).
10. M. L. Khodachenko and V. V. Zaitsev, Astrophys. Space Sci. **279**, 389 (2002).
11. H. Knoepfel and D. A. Strong, Nucl. Fusion **19**, 785 (1979).
12. R. Lee and R. H. Sudan, Phys. Fluids **14**, 1213 (1971).
13. Yu. E. Litvinenko, Astrophys. J. **462**, 997 (1996).
14. R. V. Lovelace and R. N. Sudan, Phys. Rev. Lett. **27**, 1256 (1971).
15. J. T. Mariska, A. G. Emslie, and P. Li, Astrophys. J. **341**, 1067 (1989).
16. A. N. McClymont and R. C. Canfield, Astrophys. J. **305**, 936 (1986).
17. D. B. Melrose, Astrophys. J. **381**, 306 (1991).
18. D. B. Melrose, Astrophys. J. **451**, 391 (1995).
19. J. A. Miller, P. J. Cargill, G. D. Holman, *et al.*, J. Geophys. Res. **102**, 14 631 (1997).
20. E. R. Priest, *Solar Magnetohydrodynamics* (Reidel, Dordrecht, 1982; Mir, Moscow, 1985).
21. A. V. Stepanov, B. Kliem, V. V. Zaitsev, *et al.*, Astron. Astrophys. **374**, 1072 (2001).
22. G. H. J. Van der Oord, Astron. Astrophys. **234**, 496 (1990).
23. V. V. Zaitsev and M. L. Khodachenko, Izv. Vyssh. Uchebn. Zaved. Radiofiz. **40**, 176 (1997).
24. V. V. Zaitsev, A. G. Kislyakov, A. V. Stepanov, *et al.*, Pis'ma Astron. Zh. **30**, 362 (2004) [Astron. Lett. **30**, 319 (2004)].
25. V. V. Zaitsev and A. V. Stepanov, Astron. Zh. **68**, 384 (1991) [Sov. Astron. **35**, 189 (1991)].
26. V. V. Zaitsev and A. V. Stepanov, Sol. Phys. **139**, 343 (1992).
27. V. V. Zaitsev, A. V. Stepanov, S. Urpo, and S. Pohjolainen, Astron. Astrophys. **337**, 887 (1998).
28. V. V. Zaitsev, E. Ya. Zlotkin, and G. Aurass, Pis'ma Astron. Zh. **31**, 315 (2005) [Astron. Lett. **31**, 285 (2005)].
29. E. Ya. Zlotnik, V. V. Zaitsev, H. Aurass, *et al.*, Astron. Astrophys. **410**, 1011 (2003).

Translated by V. Astakhov

Astronomy Letters, Vol. 31, No. 9, 2005, pp. 627–633. Translated from Pis'ma v Astronomicheskiĭ Zhurnal, Vol. 31, No. 9, 2005, pp. 701–708.

Multiple Resonance in One Problem of the Stability of the Motion of a Satellite Relative to the Center of Mass

A. P. Markeev*

Institute for Problems of Mechanics, Russian Academy of Sciences, Moscow, Russia

Received March 30, 2005

Abstract—We investigate the stability of the periodic motion of a satellite, a rigid body, relative to the center of mass in a central Newtonian gravitational field in an elliptical orbit. The orbital eccentricity is assumed to be low. In a circular orbit, this periodic motion transforms into the well-known motion called hyperboloidal precession (the symmetry axis of the satellite occupies a fixed position in the plane perpendicular to the radius vector of the center of mass relative to the attractive center and describes a hyperboloidal surface in absolute space, with the satellite rotating around the symmetry axis at a constant angular velocity). We consider the case where the parameters of the problem are close to their values at which a multiple parametric resonance takes place (the frequencies of the small oscillations of the satellite's symmetry axis are related by several second-order resonance relations). We have found the instability and stability regions in the first (linear) approximation at low eccentricities. © *2005 Pleiades Publishing, Inc.*

Key words: *celestial mechanics, resonance, stability, periodic motion, satellite.*

INTRODUCTION

Consider the motion of a satellite relative to the center of mass in a central Newtonian gravitational field. The satellite is a rigid body whose central ellipsoid of inertia is an ellipsoid of revolution. We denote the equatorial and polar moments of inertia by A and C, respectively. The linear size of the satellite is small compared to the size of the orbit of its center of mass O. Therefore, the motion of the satellite relative to the center of mass may be assumed (Beletskiĭ 1975) to have no effect on the shape of the orbit. We assume that the center of mass moves in an elliptical orbit with an eccentricity e.

Let $Oxyz$ be a coordinate system rigidly bound to the satellite and its Oz axis be directed along the dynamical symmetry axis of the satellite. We refer the motion of the satellite to the orbital $OXYZ$ coordinate system; its OX, OY, and OZ axes are directed along the transversal to the orbit, the binormal, and the radius vector of the satellite's center of mass relative to the attractive center, respectively. We specify the orientation of the $Oxyz$ trihedron relative to the orbital coordinate system by the Euler angles ψ, θ, and φ.

Since the satellite is dynamically symmetric, the r projection of its absolute angular velocity onto the symmetry axis is constant:

$$r = \omega(\dot{\psi}\cos\theta + \dot{\varphi}) = r_0 = \text{const},$$

$$\omega = \frac{d\nu}{dt} = \frac{\omega_0}{(1-e^2)^{3/2}}(1+e\cos\nu)^2, \quad \omega_0 = \frac{2\pi}{T},$$

where ν is the true anomaly, T is the orbital period of the center of mass, and the dot denotes differentiation with respect to ν.

We denote the momenta corresponding to the angles θ and ψ that were made dimensionless using the factor $A\omega_0(1-e^2)^{-3/2}$ by p_θ and p_ψ. We take the true anomaly as an independent variable. The Hamiltonian that describes the motion of the symmetry axis of the satellite in the orbital coordinate system is (Markeev 1967)

$$\begin{aligned}\Gamma = {} & \frac{p_\theta^2}{2(1+e\cos\nu)^2} + \frac{p_\psi^2}{2(1+e\cos\nu)^2\sin^2\theta} \\ & - p_\theta\sin\psi - p_\psi cot\theta\cos\psi \\ & - \frac{\alpha\beta(1-e^2)^{3/2}}{(1+e\cos\nu)^2}p_\psi\frac{\cos\theta}{\sin^2\theta} \\ & + \alpha\beta(1-e^2)^{3/2}\frac{\cos\psi}{\sin\theta} + \frac{\alpha^2\beta^2(1-e^2)^3}{2(1+e\cos\nu)^2}cot^2\theta \\ & + \frac{3}{2}(\alpha-1)(1+e\cos\nu)\cos^2\theta,\end{aligned} \tag{1}$$

where

$$\beta = \frac{r_0}{\omega_0}, \quad \alpha = \frac{C}{A}, \quad 0 \leqslant \alpha \leqslant 2.$$

In a circular orbit ($e = 0$), there are families of satellite motions for which the dynamical symmetry

*E-mail: markeev@ipmnet.ru

axis of the satellite occupies a fixed position in the orbital coordinate system, while the satellite precesses regularly in absolute space (see the monographs by Beletskiĭ (1975) and Sarychev (1978) and references therein). We will consider only one of these families of satellite motions that came to be known as hyperboloidal precessions. The following solution of the equations of motion corresponds to these:

$$\theta_0 = \frac{\pi}{2}, \quad \cos\psi_0 = -\alpha\beta, \quad p_{\theta_0} = \sin\psi_0, \quad p_{\psi_0} = 0. \tag{2}$$

For solution (2), the Oz axis of dynamical symmetry of the satellite lies in the OXY plane that is perpendicular to the radius vector of the center of mass and makes the angle $\pi - \psi_0$ with the OY normal to the orbital plane. In this case, the angular velocity of proper rotation is constant and defined by

$$\frac{d\varphi}{dt} = \omega_0 \frac{\alpha - 1}{\alpha}\cos\psi_0.$$

In absolute space, the symmetry axis describes a one-sheet hyperboloid of revolution whose axis passes through the attractive center and is perpendicular to the orbital plane.

The hyperboloidal precession is unstable against perturbations in θ, ψ, p_θ, and p_ψ for a dynamically prolate ($\alpha < 1$) satellite and stable for a dynamically oblate ($\alpha > 1$) satellite. The assertion about the instability can be proven by considering the characteristic equation of the linearized equations of perturbed motion, while the stability follows from the positive definiteness of Hamiltonian (1) (at $e = 0, \alpha > 1$) in the neighborhood of solution (2) (Beletskiĭ 1975; Sarychev 1978).

We also assume that the set of admissible values of the parameters α and ψ_0 is given by the inequalities

$$1 < \alpha \leqslant 2, \quad 0 < \psi_0 < \frac{\pi}{2}. \tag{3}$$

The frequencies ω_1 and ω_2 ($\omega_1 > \omega_2$) of the small oscillations of the symmetry axis in the vicinity of its stationary position (2) in the orbital coordinate system obey the equation

$$\omega^4 - (3\alpha - 2)\omega^2 + 3(\alpha - 1)\sin^2\psi_0 = 0.$$

The oscillation frequencies in domain (3) can be shown to obey the inequality

$$0 < \omega_2 < 1 < \omega_1 < 2. \tag{4}$$

If the center of mass moves in an elliptical orbit, then the equations of motion do not admit of the stationary solution (2). Sarychev (1965) showed that for a weakly elliptical orbit ($0 < e \ll 1$) at any α and ψ_0 from domain (3), solution (2) transforms into the 2π-periodic (in ν) solution $\tilde\theta(\nu)$, $\tilde\psi(\nu)$, $\tilde p_\theta(\nu)$, $\tilde p_\psi(\nu)$, which can be represented as a power series of e. For this solution, the symmetry axis of the satellite periodically oscillates near its stationary position (2) with a period equal to the orbital period of the center of mass.

Let us analyze the stability of these periodic oscillations in the first (linear) approximation. We introduce the perturbations q_j, p_j ($j = 1, 2$) in a standard way:

$$\theta = \tilde\theta(\nu) + q_1, \quad \psi = \tilde\psi(\nu) + q_2, \tag{5}$$
$$p_\theta = \tilde p_\theta(\nu) + p_1, \quad p_\psi = \tilde p_\psi(\nu) + p_2.$$

The Hamiltonian F of the perturbed motion can be calculated using the formula

$$F = \Gamma + \frac{d\tilde p_\theta}{d\nu}q_1 + \frac{d\tilde p_\psi}{d\nu}q_2 - \frac{d\tilde\theta}{d\nu}p_1 - \frac{d\tilde\psi}{d\nu}p_2, \tag{6}$$

where Γ is Hamiltonian (1) with the change of variables (5).

Instability regions (regions of parametric resonance) exist in the space of parameters α, ψ_0, e at low e. At $e = 0$, they degenerate into curves in the α, ψ_0 plane, which we call generating curves. Recalling that the part of the Hamiltonian of perturbed motion (6) at $e = 0$, which is quadratic in q_j, p_j ($j = 1, 2$), has a fixed sign (Beletskiĭ 1975) and that the frequencies of the small oscillations obey inequality (4), we find on the basis of the Krein–Gelfand–Lidskii theorem (Yakubovich and Starzhinskiĭ 1987) that three generating curves exist in domain (3):

$$(1)\ 2\omega_2 = 1, \quad (2)\ \omega_1 + \omega_2 = 2, \quad (3)\ 2\omega_1 = 3. \tag{7}$$

Curves (7) are shown in Fig. 1. They intersect at point Q^* with the coordinates $\alpha^* = 3/2$, $\psi_0^* = \arcsin(\sqrt{6}/4) \approx 37°45'$. A multiple parametric resonance takes place at this point.

The goal of this study is to solve the problem of the stability of the periodic motion of a satellite's symmetry axis in the first (linear) approximation for low eccentricities e and parameters α, ψ_0 close or equal to α^*, ψ_0^*. The multiple resonance in linear Hamiltonian systems has been studied inadequately. Some of the algorithms for analyzing multiple resonances and their applications to the dynamics of satellites have been published quite recently (Markeev 2005a, 2005b).

PERIODIC MOTION

The functions $\tilde\theta(\nu)$, $\tilde\psi(\nu)$, $\tilde p_\theta(\nu)$, $\tilde p_\psi(\nu)$ that specify the periodic motion of the satellite's symmetry axis under study can be found by setting the first-order form in the expansion of Hamiltonian (6) into a power series of q_j, p_j ($j = 1, 2$) equal to zero. Calculations

show that these functions can be represented as the expansions

$$\tilde{\theta}(\nu) = \frac{\pi}{2} + \frac{9}{2}(\alpha-1)\sin\psi_0\delta_1\delta_2[e^2 a_{2,2}\sin 2\nu + e^3(a_{1,3}\sin\nu + a_{3,3}\sin 3\nu)] + O(e^4), \quad (8)$$

$$\tilde{\psi}(\nu) = \psi_0 - \frac{1}{2}tan\psi_0[4e\cos\nu + e^2(b_{0,2} + b_{2,2}\cos 2\nu) - 9e^3(\alpha-1)\delta_1\delta_2(b_{1,3}\cos\nu + b_{3,3}\cos 3\nu)] + O(e^4),$$

$$\tilde{p}_\theta(\nu) = \sin\psi_0 + \frac{3}{2}(\alpha-1)\sin\psi_0\delta_1[e^2(c_{0,2} + c_{2,2}\cos 2\nu) - 18e^3\delta_2(c_{1,3}\cos\nu + c_{3,3}\cos 3\nu)] + O(e^4),$$

$$\tilde{p}_\psi(\nu) = \frac{1}{2}tan\psi_0[4e\sin\nu - 6e^2(\alpha-1)d_{2,2}\sin 2\nu + 27e^3(\alpha-1)^2\delta_1\delta_2(d_{1,3}\sin\nu + d_{3,3}\sin 3\nu)] + O(e^4).$$

Here, we use the following notation:

$$a_{2,2} = 2(\cos^2\psi_0 - 4),$$
$$a_{1,3} = -3(\alpha-1)\delta_1(\cos^2\psi_0 - 2)(\cos^2\psi_0 - 4),$$
$$a_{3,3} = -3\delta_3[(\alpha-1)\cos^4\psi_0 - 2(35\alpha-67)\cos^2\psi_0 + 8(19\alpha-43)],$$
$$b_{0,2} = 2,$$
$$b_{2,2} = 3\delta_2[(\alpha-1)\cos^2\psi_0 + 2(5\alpha-9)],$$
$$b_{1,3} = 3(\alpha-1)\delta_1[(\alpha-1)\cos^6\psi_0 - (8\alpha-7)\cos^4\psi_0 + 2(4\alpha+1)\cos^2\psi_0 - 8(3\alpha-4)],$$
$$b_{3,3} = \delta_3[(\alpha-1)^2\cos^6\psi_0 - (\alpha-1)(2\alpha-1)\cos^4\psi_0 + 2(104\alpha^2 - 519\alpha + 535)\cos^2\psi_0 - 8(\alpha-4)(3\alpha+5)],$$
$$c_{0,2} = 3\cos^2\psi_0 + 2,$$
$$c_{2,2} = 3\delta_2[5(\alpha-1)\cos^2\psi_0 - 2(3\alpha+1)],$$
$$c_{1,3} = \delta_1(\alpha-1)[(2\alpha-1)\cos^4\psi_0 - (11\alpha-7)\cos^2\psi_0 + 12(\alpha-1)],$$
$$c_{3,3} = \delta_3[(\alpha-1)(2\alpha-3)\cos^4\psi_0 - (29\alpha^2 - 50\alpha - 3)\cos^2\psi_0 + 4(7\alpha^2 + 6\alpha - 37)],$$
$$d_{2,2} = \delta_2(\cos^2\psi_0 - 4),$$
$$d_{1,3} = \delta_1[(25\alpha-34)\cos^4\psi_0 - 2(4\alpha+5)\cos^2\psi_0 + 8(3\alpha-4)],$$
$$d_{3,3} = 3\delta_3[(9\alpha-20)\cos^4\psi_0 - 6(4\alpha-11)\cos^2\psi_0 + 8(\alpha-4)],$$
$$\delta_n = [(\omega_1^2 - n^2)(\omega_2^2 - n^2)]^{-1}, \quad n = 1, 2, 3.$$

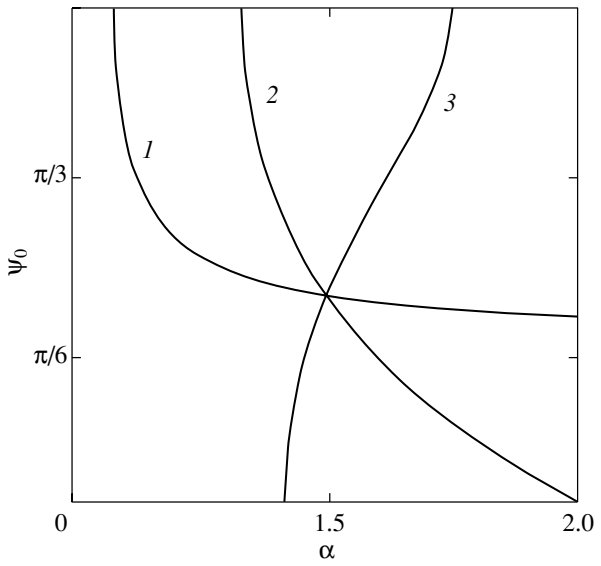

Fig. 1. Generating curves: (*1*) $2\omega_2 = 1$, (*2*) $\omega_1 + \omega_2 = 2$, (*3*) $2\omega_1 = 3$.

Expansions (8) take the following form at point Q^* of the multiple parametric resonance:

$$\tilde{\theta}(\nu) = \frac{\pi}{2} + e^2\frac{108\sqrt{6}}{175}\sin 2\nu - e^3\frac{2\sqrt{6}}{55\,125}(18\,711\sin\nu + 12\,503\sin 3\nu) + O(e^4),$$

$$\tilde{\psi}(\nu) = \arcsin\frac{\sqrt{6}}{4} - e\frac{2\sqrt{15}}{5}\cos\nu - e^2\frac{\sqrt{15}}{5}\left(1 - \frac{43}{70}\cos 2\nu\right) + e^3\frac{\sqrt{15}}{551\,250}(188\,307\cos\nu - 121\,375\cos 3\nu) + O(e^4),$$

$$\tilde{p}_\theta(\nu) = \frac{\sqrt{6}}{4} - e^2\frac{\sqrt{6}}{1400}(1085 - 1208\cos 2\nu) - e^3\frac{8\sqrt{6}}{55\,125}(1701\cos\nu + 2626\cos 3\nu) + O(e^4),$$

$$\tilde{p}_\psi(\nu) = e\frac{2\sqrt{15}}{5}\sin\nu + e^2\frac{27\sqrt{15}}{175}\sin 2\nu - e^3\frac{4\sqrt{15}}{91\,875}(22\,533\sin\nu - 485\sin 3\nu) + O(e^4).$$

CONSTRUCTING THE STABILITY AND INSTABILITY REGIONS IN THE SPACE OF PARAMETERS α, ψ_0, e

At $e = 0$, the surface that separates the stability and instability regions in the space of α, ψ_0, e degenerates into the multiple resonance point Q^*. Let the Q^*e axis be orthogonal to the α, ψ_0 plane. Consider a

family of planes that are orthogonal to the α, ψ_0 plane and pass through the Q^*e axis. Any plane from this family intersects with the α, ψ_0 plane along a straight line that makes an angle whose tangent we denote by k ($-\infty < k < \infty$) with the horizontal line. We represent the equation for the sought-for boundary surface in parametric form by taking the eccentricity e and slope k as the parameters.

Retaining the first-order terms in e, we write the equation for the sought-for boundary surface as

$$\alpha = \frac{3}{2} + es, \quad \psi_0 = \arcsin\frac{\sqrt{6}}{4} + eks, \qquad (9)$$

where s is a function of the parameter k. Below, we determine this function from the condition that the point with coordinates (9) lie on the boundary surface at given e and k.

We substitute formulas (9) for α and ψ_0 into the part F_2 of Hamiltonian (6) of perturbed motion, which is quadratic in q_j, p_j ($j = 1, 2$), and expand it into a power series of e to obtain

$$F_2 = F_2^{(0)} + eF_2^{(1)} + O(e^2), \qquad (10)$$

where

$$F_2^{(0)} = \frac{3}{4}q_1^2 + \frac{1}{2}q_2^2 - \frac{\sqrt{10}}{4}q_2p_1 + \frac{1}{2}p_1^2 + \frac{1}{2}p_2^2,$$

$$F_2^{(1)} = \frac{6s - \cos\nu}{4}q_1^2 - \frac{3\sqrt{10}\sin\nu}{10}q_1q_2$$
$$+ \frac{4\sqrt{10}\cos\nu}{5}q_1p_2 + \frac{5\sqrt{6}ks - 6\sqrt{10}\cos\nu}{20}q_2p_1$$
$$- \cos\nu p_1^2 - \cos\nu p_2^2.$$

Let us make a linear periodic (in ν) canonical transformation that eliminates ν from all terms of Hamiltonian (10) up to the first order in e inclusive according to an algorithm from Markeev (2005b). We construct this substitution using Kamel's modification of the Deprit–Hori method (Markeev 1978). To simplify the calculations, we should first make a canonical change of variables $q_1, q_2, p_1, p_2 \to x_1, x_2, X_1, X_2$ that eliminates the "unperturbed" part $F_2^{(0)}$ from Hamiltonian (10). This change of variables can be specified by the equality

$$(q_1, q_2, p_1, p_2)^{\mathrm{t}} = \mathbf{X}(\nu)\,(x_1, x_2, X_1, X_2)^{\mathrm{t}}, \qquad (11)$$

where the superscript "t" denotes transposition and $\mathbf{X}(\nu)$ is the fundamental matrix of solutions of the system with the Hamiltonian $F_2^{(0)}$. The matrix elements $x_{mn}(\nu)$ can be calculated using the formulas

$$x_{11} = \frac{1}{8}(3\cos\frac{\nu}{2} + 5\cos\frac{3\nu}{2}),$$

$$x_{12} = \frac{\sqrt{10}}{16}(\sin\frac{\nu}{2} - 3\sin\frac{3\nu}{2}),$$

$$x_{13} = \frac{1}{8}(\sin\frac{\nu}{2} + 5\sin\frac{3\nu}{2}),$$

$$x_{14} = -\frac{\sqrt{10}}{8}(\cos\frac{\nu}{2} - \cos\frac{3\nu}{2}),$$

$$x_{21} = -\frac{\sqrt{10}}{8}(3\sin\frac{\nu}{2} - \sin\frac{3\nu}{2}),$$

$$x_{22} = \frac{1}{8}(5\cos\frac{\nu}{2} + 3\cos\frac{3\nu}{2}),$$

$$x_{23} = \frac{\sqrt{10}}{8}(\cos\frac{\nu}{2} - \cos\frac{3\nu}{2}),$$

$$x_{24} = \frac{1}{4}(5\sin\frac{\nu}{2} + \sin\frac{3\nu}{2}),$$

$$x_{3n} = \frac{\sqrt{10}}{4}x_{2n} + \frac{dx_{1n}}{d\nu},$$

$$x_{4n} = \frac{dx_{2n}}{d\nu}, \quad n = 1, 2, 3, 4.$$

The Hamiltonian in variables x_1, x_2, X_1, and X_2 is still 2π-periodic in ν and can be written as

$$H = H_0 + eH_1(x_1, x_2, X_1, X_2, \nu; k, s) + O(e^2), \qquad (12)$$

where $H_0 \equiv 0$, a H_1 is the function $F_2^{(1)}$ from expansion (10) with the change of variables (11).

Let us now make the linear canonical 2π-periodic (in ν) transformation $x_1, x_2, X_1, X_2 \to y_1, y_2, Y_1, Y_2$ that eliminates ν from the terms of the new Hamiltonian up to the first order in e. We obtain the following formula for the new Hamiltonian K:

$$K = eK_1 + O(e^2), \qquad (13)$$

where the function K_1 is defined by the equality (Markeev 2005b)

$$K_1 = \frac{1}{2\pi}\int_0^{2\pi} H_1(y_1, y_2, Y_1, Y_2, \nu; k, s)d\nu.$$

Calculations show that this function can be written as

$$K_1 = \frac{1}{1024}(88\sqrt{15}ks + 408s - 81)y_1^2 \qquad (14)$$
$$- \frac{1}{2560}(1000\sqrt{6}ks - 120\sqrt{10}s + 657\sqrt{10})y_1Y_2$$
$$+ \frac{1}{2048}(24\sqrt{15}ks + 600s + 309)y_2^2$$
$$+ \frac{1}{5120}(600\sqrt{6}ks - 840\sqrt{10}s - 483\sqrt{10})y_2Y_1$$
$$- \frac{1}{1024}(8\sqrt{15}ks - 312s + 255)Y_1^2$$
$$+ \frac{1}{512}(56\sqrt{15}ks + 120s + 483)Y_2^2.$$

We drop the terms higher than the first order in e in Hamiltonian (13) to obtain an approximate system whose motion can be described by a linear autonomous system of differential equations of the form

$$\frac{dy_j}{d\tau} = \frac{\partial K_1}{\partial Y_j}, \quad \frac{dY_j}{d\tau} = -\frac{\partial K_1}{\partial y_j}, \quad j = 1, 2, \qquad (15)$$

where $\tau = e\nu$ is taken as an independent variable.

The characteristic equation of system (15) is

$$\lambda^4 + a\lambda^2 + b = 0, \qquad (16)$$

where

$$a = \frac{1}{128}(75k^2 - 6\sqrt{15}k + 117)s^2 + \frac{3357}{20\,480},$$

$$b = \frac{9}{65\,536}(\sqrt{15} - k)^2(15k + \sqrt{15})^2 s^4 - \frac{27}{5\,242\,880}(\sqrt{15} - k)(23\,645k + 11\,203\sqrt{15})s^2 + \frac{96\,059\,601}{419\,430\,400}.$$

At low e, a sufficient condition for stability is the satisfaction of the system of inequalities

$$a > 0, \quad b > 0, \quad d = a^2 - 4b > 0. \qquad (17)$$

If at least one of inequalities (17) is satisfied with the opposite sign, then instability takes place.

The fact that the coefficient of s^2 in the formula for the coefficient a is positive at any k implies that the first inequality in (17) is always satisfied. Therefore, the values of $s = s(k)$ corresponding to the boundaries of the stability and instability regions can be found from the equation $b = 0$ or $d = 0$.

The formula for d can be written as

$$d = \frac{9}{25\,600}(5k - \sqrt{15})^2(5k + 3\sqrt{15})^2 s^4 - \frac{27}{409\,600}(895k - 1268\sqrt{15})(5k + 3\sqrt{15})s^2 - \frac{74\,593\,791}{83\,886\,080}.$$

Both equations $b = 0$ and $d = 0$ do not change when $-s$ is substituted for s. It follows from this and from equalities (9) that, to a first approximation in e, the stability and instability regions in the α, ψ_0 plane (at fixed e) are centrally symmetric, with the point Q^* of multiple resonance being the center of symmetry.

Let us introduce the deviations ξ and η from point Q^* defined by the formulas $\xi = \alpha - 3/2$ and $\eta = \psi_0 - \arcsin(\sqrt{6}/4)$. In view of the above symmetry, to construct the boundaries of the stability and instability regions, it will suffice to find them in the first ($\xi \geq 0$, $\eta \geq 0$) and fourth ($\xi \geq 0$, $\eta \leq 0$) quadrants of the $e =$ const plane.

Omitting the details of a simple joint analysis of the biquadratic equations $b = 0$ and $d = 0$, we immediately give the result. We denote

$$z_1(k) = \frac{12(895k - 1268\sqrt{15}) + 99\,\mathrm{sgn}(5k + 3\sqrt{15})\sqrt{5(23\,495k^2 - 15\,126\sqrt{15}k + 83\,553)}}{128(5k + 3\sqrt{15})(5k - \sqrt{15})^2},$$

$$z_{2,3}(k) = \frac{3[23\,645k + 11\,203\sqrt{15} \mp 95\sqrt{(\sqrt{15} - k)(56\,315k + 13\,381\sqrt{15})}]}{160(\sqrt{15} - k)(15k + \sqrt{15})^2}$$

(the upper and lower signs in the last equality correspond to z_2 and z_3, respectively) and set $s_i(k) = \sqrt{z_i(k)}$ ($i = 1, 2, 3$). Here, s_1 is the root of the equation $d = 0$, while s_2 and s_3 are the roots of the equation $b = 0$ with $s_3 \geq s_2 > s_1 > 0$.

At $0 \leq k < k^* = \sqrt{15} \approx 3.873$, three regions of the surface that separates the stability and instability regions exist in the first quadrant ($\xi \geq 0, \eta \geq 0$); these can be specified parametrically by the equalities $\xi_i = es_i(k)$, $\eta_i = eks_i(k)$, and $i = 1, 2, 3$. If $k^* \leq k < \infty$, there exists only one region of the boundary surface specified by the equalities $\xi_1 = es_1(k)$, $\eta_1 = eks_1(k)$.

In the fourth quadrant ($\xi \geq 0$, $\eta \leq 0$), there exist one region of the boundary surface $\xi_1 = es_1(k)$, $\eta_1 = eks_1(k)$ for k satisfying the inequality $-\infty < k \leq k^{**} = -13\,381\sqrt{15}/56\,315 \approx -0.920$ and three regions $\xi_i = es_i(k)$, $\eta_i = eks_i(k)$, $i = 1, 2, 3$ for $k^{**} < k < 0$.

Analysis of the last two inequalities in (17) shows that if $0 \leq k < k^*$ (in the first quadrant) or $k^{**} < k < 0$ (in the fourth quadrant), then two instability regions defined by the inequalities $0 \leq \xi < \xi_1$ и $\xi_2 < \xi < \xi_3$ exist on the straight line $\eta = k\xi$. If, however, $k^* \leq k < \infty$ (in the first quadrant) or $-\infty < k \leq k^{**}$

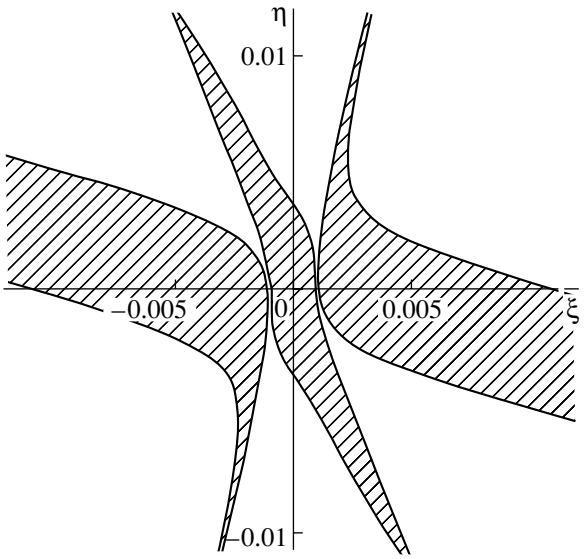

Fig. 2. Stability and instability regions in the $e = 0.002$ plane.

(in the fourth quadrant), then one instability region $0 \le \xi < \xi_1$ exists on the straight line $\eta = k\xi$.

Figure 2 shows the stability and instability regions constructed using the above formulas. We set the eccentricity equal to 0.002. The instability regions are hatched.

STABILITY AND INSTABILITY REGIONS IN TWO SPECIAL CASES

Consider the special cases where one of the parameters ψ_0 or α is fixed ($\psi_0 = \arcsin(\sqrt{6}/4)$ or $\alpha = 3/2$). In these special cases, the construction of the stability and instability regions is simplified greatly. In contrast to the previous section, where we constructed the boundary surfaces in the space of three parameters α, ψ_0, and e, here we need to construct the boundary curves in the planes of two parameters e, α or e, ψ_0. We constructed these curves using an algorithm from our previous paper (Markeev 2005b).

In the case of fixed ψ_0 ($\psi_0 = \arcsin(\sqrt{6}/4) \approx 0.659058$), three instability regions exist in the e, α plane near point $(0, 3/2)$ (Fig. 3). The numbers 1, 2, …, 6 in Fig. 3 mark the six boundaries $\alpha_j = \alpha_j(e)$, $j = 1, 2, \ldots, 6$ of these regions. Calculations show that the equations for these boundaries can be specified, to the third order in e, by the equalities

$$\alpha_1(e) = 1.5 - 5.266907e + 58.501637e^2 - 653.497628e^3,$$
$$\alpha_2(e) = 1.5 - 0.516907e + 0.284027e^2 + 2.266164e^3,$$
$$\alpha_3(e) = 1.5 - 0.476119e + 0.044143e^2 + 0.821735e^3,$$
$$\alpha_{i+3}(e) = \alpha_i(-e), \quad i = 1, 2, 3.$$

In the case of fixed α ($\alpha = 3/2$), one instability region exists in the e, ψ_0 plane near point $(0, \arcsin(\sqrt{6}/4))$ (Fig. 4). Its boundaries can be specified, to the third order in e (*7*, *8* in Fig. 4), by the equations

$$\alpha_7(e) = 0.659058 - 1.670926e + 3.971639e^2 - 23.007582e^3, \quad \alpha_8(e) = \alpha_7(-e).$$

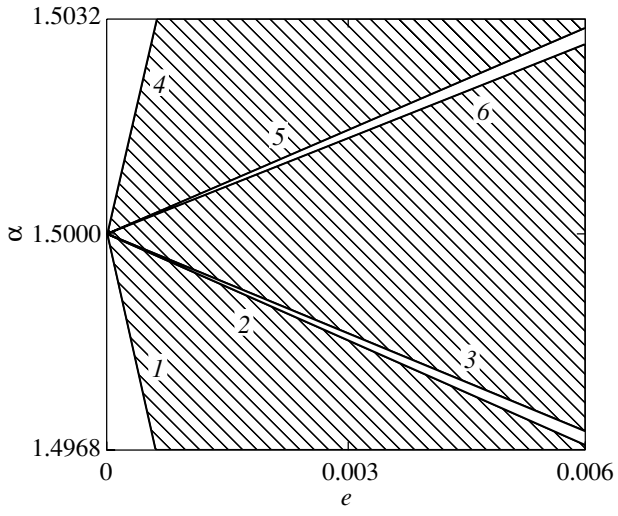

Fig. 3. Stability and instability regions at $\psi_0 = \psi_0^* = \arcsin\dfrac{\sqrt{6}}{4}$.

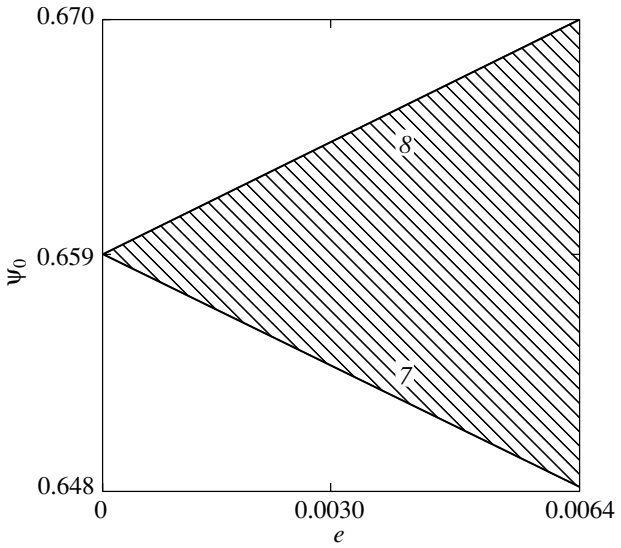

Fig. 4. Stability and instability regions at $\alpha = \alpha^* = \dfrac{3}{2}$.

The instability regions in Figs. 3 and 4 are hatched.

CONCLUSIONS

We analyzed the motion of a dynamically symmetric satellite, a rigid body, relative to the center of mass in an elliptical orbit. We found a periodic (in the orbital coordinate system) motion of the symmetry axis of the satellite, to the third order in eccentricity, that arises from the stationary position of the axis in a plane perpendicular to the radius vector of the center of mass in a circular orbit. We constructed the instability regions of this motion for parameters of the problem close or equal to their values corresponding to a multiple parametric resonance (when the frequencies ω_1 and ω_2 of the small oscillations of the symmetry axis in a circular orbit simultaneously obey the two resonance relations $2\omega_1 = 3$ and $2\omega_2 = 1$).

ACKNOWLEDGMENTS

This work was supported by the Russian Foundation for Basic Research (project no. 05-01-00386) and the Program of the President of the Russian Federation for Support of Leading Scientific Schools (project no. NSh-1477.2003.1).

REFERENCES

1. V. V. Beletskiĭ, *Motion of a Satellite Relative to the Center of Mass in a Gravitation Field* (Mosk. Gos. Univ., Moscow, 1975) [in Russian].
2. A. P. Markeev, Kosm. Issled. **5**, 530 (1967).
3. A. P. Markeev, *Libration Points in Celestial Mechanics and Cosmodynamics* (Nauka, Moscow, 1978) [in Russian].
4. A. P. Markeev, Pis'ma Astron. Zh. **31**, 388 (2005a) [Astron. Lett. **31**, 350 (2005a)].
5. A. P. Markeev, Dokl. Akad. Nauk **402** (1-3), 202 (2005b) [Dokl. Phys. **50**, 278 (2005b)].
6. V. A. Sarychev, Kosm. Issled. **3**, 667 (1965).
7. V. A. Sarychev, *Results of Science and Technology,* Vol. 11: *Problems of Orientation of Artificial Satellites* (VINITI, Moscow, 1978) [in Russian].
8. V. A. Yakubovich and V. M. Starzhinskiĭ, *Parametric Resonance in Linear Systems* (Nauka, Moscow, 1987) [in Russian].

Translated by A. Dambis

Astronomy Letters, Vol. 31, No. 9, 2005, pp. 634–644. Translated from Pis'ma v Astronomicheskiĭ Zhurnal, Vol. 31, No. 9, 2005, pp. 709–720.

Search for and Study of Nearly Periodic Orbits in the Plane Problem of Three Equal-Mass Bodies

A. I. Martynova[1] and V. V. Orlov[2*]

[1] *St. Petersburg Forestry Engineering Academy, Institutskiĭ per. 5, St. Petersburg, 194022 Russia*

[2] *Sobolev Astronomical Institute, St. Petersburg State University, Universitetskiĭ pr. 28, St. Petersburg, Peterhof, 198504 Russia*

Received March 14, 2005

Abstract—We analyze nearly periodic solutions in the plane problem of three equal-mass bodies by numerically simulating the dynamics of triple systems. We identify families of orbits in which all three points are on one straight line (syzygy) at the initial time. In this case, at fixed total energy of a triple system, the set of initial conditions is a bounded region in four-dimensional parameter space. We scan this region and identify sets of trajectories in which the coordinates and velocities of all bodies are close to their initial values at certain times (which are approximately multiples of the period). We classify the nearly periodic orbits by the structure of trajectory loops over one period. We have found the families of orbits generated by von Schubart's stable periodic orbit revealed in the rectilinear three-body problem. We have also found families of hierarchical, nearly periodic trajectories with prograde and retrograde motions. In the orbits with prograde motions, the trajectory loops of two close bodies form looplike structures. The trajectories with retrograde motions are characterized by leafed structures. Orbits with central and axial symmetries are identified among the families found. © *2005 Pleiades Publishing, Inc.*

Key words: *celestial mechanics, periodic orbits, three-body problem.*

INTRODUCTION

Periodic solutions play an important role in the dynamics of many systems encountered in studying various natural phenomena. In particular, according to the KAM theory, stable periodic orbits are surrounded by a nonzero-measure set of trajectories with finite motions (see, e.g., Contopoulos 2002). In this paper, we call these orbits nearly periodic. These orbits largely determine the phase portrait of a dynamical system. For example, the orbit by von Schubart (1956) in the rectilinear three-body problem (Hietarinta and Mikkola 1993) plays such a role. An exponential divergence of neighboring phase trajectories that generates stochastic motions (see, e.g., Lichtenberg and Lieberman 1982) can be observed in the vicinity of unstable periodic orbits.

Recently, several new families of periodic orbits have been found in the general plane three-body problem (see, e.g., Moore 1993; Simo 2002; Vanderbei 2003). The best-known family is the solution in the form of a figure eight where all three equal-mass bodies move one after another along the same closed curve of the corresponding shape (Chenciner and Montgomery 2000). This kind of periodic orbits was called choreography. The figure eight is the only known choreography in the problem of three equal-mass bodies the stability of which has been established.

Minimization of the action functional is occasionally used to find periodic solutions (see, e.g., Moore 1993; Vanderbei 2003). As a result, a periodic orbit is obtained as the solution of the optimization problem.

The figure-eight orbit has a zero angular momentum and is intermediate between the other two stable periodic orbits found by von Schubart (1956) and Broucke (1979) in the two extreme cases of the three-body problem, rectilinear and isosceles. Orlov *et al.* (2004) showed that these three orbits are connected by a kind of a bridge of long-lived, but breaking-up trajectories. These trajectories exhibit the properties of different periodic orbits at different times and can change these properties during their evolution; i.e., the phase trajectory "sticks" alternately to the neighborhood of a particular periodic orbit.

All three bodies in these three periodic orbits are sometimes on one straight line (the so-called syzygies take place). Searching for other families of periodic orbits with syzygies is of considerable interest. This is the goal of our study.

*E-mail: vor@astro.spbu.ru

1063-7737/05/3109-0634$26.00

THE TECHNIQUE

Consider the following method of specifying initial conditions. Let all three bodies be on one straight line at the initial time. Let us make this straight line coincident with the OX axis and place the coordinate origin at the center of mass of the triple system. Since we consider only two-dimensional motions, we assume that the bodies are always in the XOY plane; i.e., the bodies have zero coordinates and velocities in the Z direction.

Let us choose the following system of units: the gravitational constant is $G = 1$, the masses of the bodies are equal to unity, and the total energy of the triple system is $E = -1$. We take the maximum separation between the components $M_1M_3 = 1$ as the unit of length (see Fig. 1). Let the central body M_2 be closer to the extreme body M_3 and lie at a distance $\delta \geq 0$ from point O at the initial time. The quantity $\delta \in [0, 1/3)$ is a dimensionless parameter of the problem if it is expressed in terms of the separation $M_1M_3 = 1$. The coordinates of the bodies M_1 and M_3 are

$$x_1 = -\frac{1+\delta}{2}, \qquad (1)$$
$$x_3 = \frac{1-\delta}{2}.$$

Consider the magnitudes of the velocity vectors of the bodies (V_1, V_2, V_3) and the angles (φ_1, φ_2, φ_3) that the velocity vectors form with the OX axis. We will analyze the motions of the bodies in a fixed nonrotating coordinate system associated with the center of mass O of the triple system. The center-of-mass integrals would then hold:

$$V_1\cos\varphi_1 + V_2\cos\varphi_2 + V_3\cos\varphi_3 = 0, \qquad (2)$$
$$V_1\sin\varphi_1 + V_2\sin\varphi_2 + V_3\sin\varphi_3 = 0.$$

In addition, the total energy of the system would be conserved,

$$E = -1 = \frac{1}{2}(V_1^2 + V_2^2 + V_3^2) \qquad (3)$$
$$-1 - \frac{2}{1-3\delta} - \frac{2}{1+3\delta}.$$

Hence,

$$V_1^2 + V_2^2 + V_3^2 = \frac{8}{1-9\delta^2}. \qquad (4)$$

We find the magnitudes of the velocity vectors of all three bodies from Eqs. (2) and (4):

$$V_1 = A|\sin(\varphi_3 - \varphi_2)|, \qquad (5)$$
$$V_2 = A|\sin(\varphi_3 - \varphi_1)|,$$
$$V_3 = A|\sin(\varphi_2 - \varphi_1)|,$$

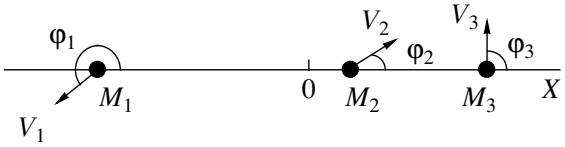

Fig. 1. Choice of initial conditions.

where

$$A = \frac{2\sqrt{2}}{\sqrt{1-9\delta^2}}[\sin^2(\varphi_2 - \varphi_1) \qquad (6)$$
$$+ \sin^2(\varphi_3 - \varphi_1) + \sin^2(\varphi_3 - \varphi_2)]^{-1/2}.$$

Imposing additional constraints on the total energy E (or the separation M_1M_3) causes the magnitudes of the velocity vectors of the bodies to be scaled. This bounds the set of possible solutions, since, in fact, we consider only a four-dimensional section (δ, φ_1, φ_2, φ_3) of the five-dimensional manifold of initial conditions.

To find nearly periodic solutions, we scan the sections $[0 \leq \delta < 1/3;\ 0^\circ \leq \varphi_1, \varphi_2, \varphi_3 < 360^\circ]$ at steps of $\Delta\delta = 0.001$ and $\Delta\varphi = 1^\circ$. To avoid double collisions, we do not consider the case

$$\sin(\varphi_i - \varphi_j) = 0 \qquad (7)$$

at $i \neq j$ ($i, j = 1, 2, 3$).

There are combinations of angles (φ_1, φ_2, φ_3) that yield symmetric trajectories, which can be used to check the calculations.

To find nearly periodic trajectories in the fixed coordinate system, we calculate the functional

$$\Phi = \frac{|\mathbf{r} - \mathbf{r}_0|}{|\mathbf{r}_0|} + \frac{|\dot{\mathbf{r}} - \dot{\mathbf{r}}_0|}{|\dot{\mathbf{r}}_0|}, \qquad (8)$$

where $\mathbf{r}$ and $\dot{\mathbf{r}}$ are the current values of the coordinate and velocity vectors for all three bodies; $\mathbf{r}_0$ and $\dot{\mathbf{r}}_0$ are their initial values. For each set of initial conditions (δ, φ_1, φ_2, φ_3), the calculations were continued for 100τ, where τ is the mean crossing time:

$$\tau = \frac{G(M_1 + M_2 + M_3)^{5/2}}{(2|E|)^{3/2}} = \frac{9\sqrt{3}}{2\sqrt{2}}. \qquad (9)$$

Here, M_i are the masses of the bodies. We chose trajectories in which the minimum of functional (8) was less than 0.1. One may expect the motions in these systems to be nearly periodic.

The calculations were performed using the TRIPLE code written by Sverre Aarseth (University of Cambridge, Great Britain). The code uses the integrator by Bulirsch and Stoer (1966) and the regularization of the equations of motion by a method developed by Aarseth and Zare (1974).

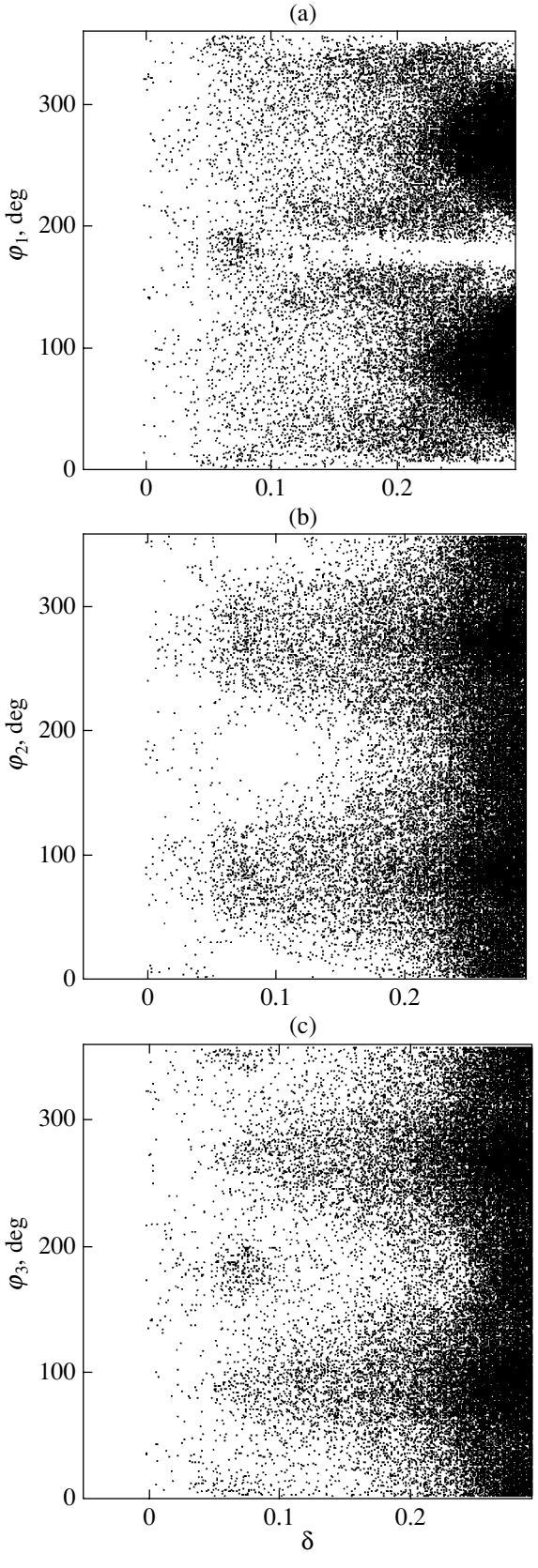

Fig. 2. Initial conditions for nearly periodic trajectories in the following sections: (a) δ, φ_1; (b) δ, φ_2; and (c) δ, φ_3.

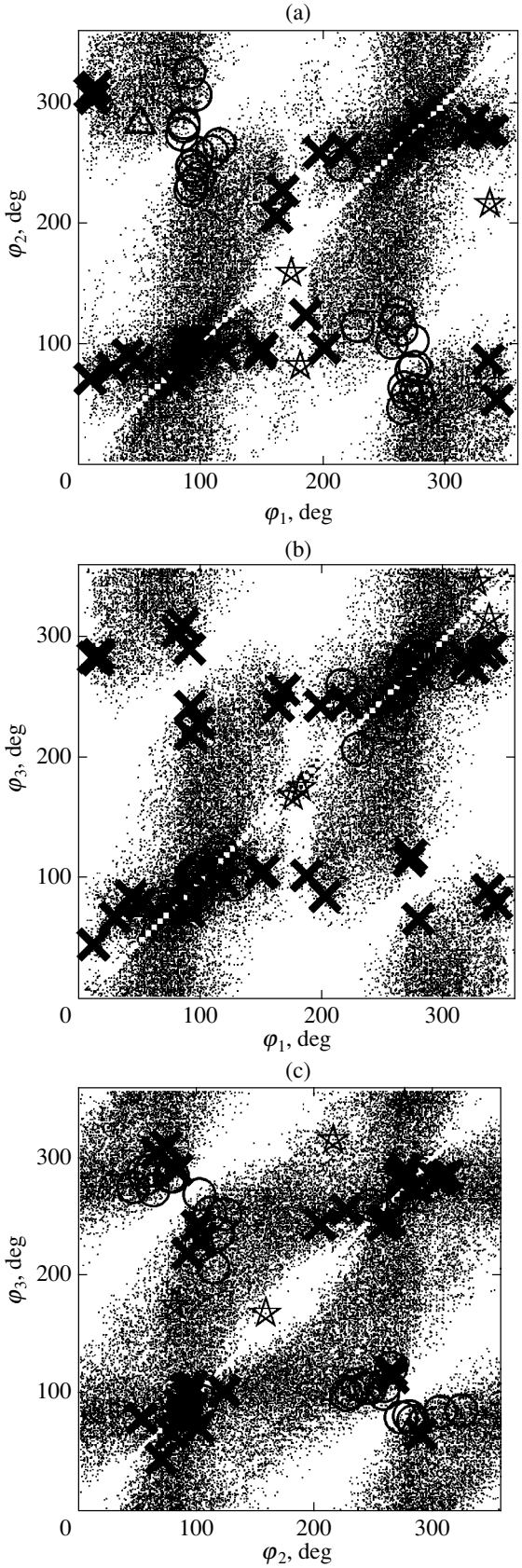

Fig. 3. (φ_i, φ_j) sections: the stars, circles, and crosses correspond to chainlike, leafed, and looplike orbits, respectively; the triangle denotes a ducati-type orbit.

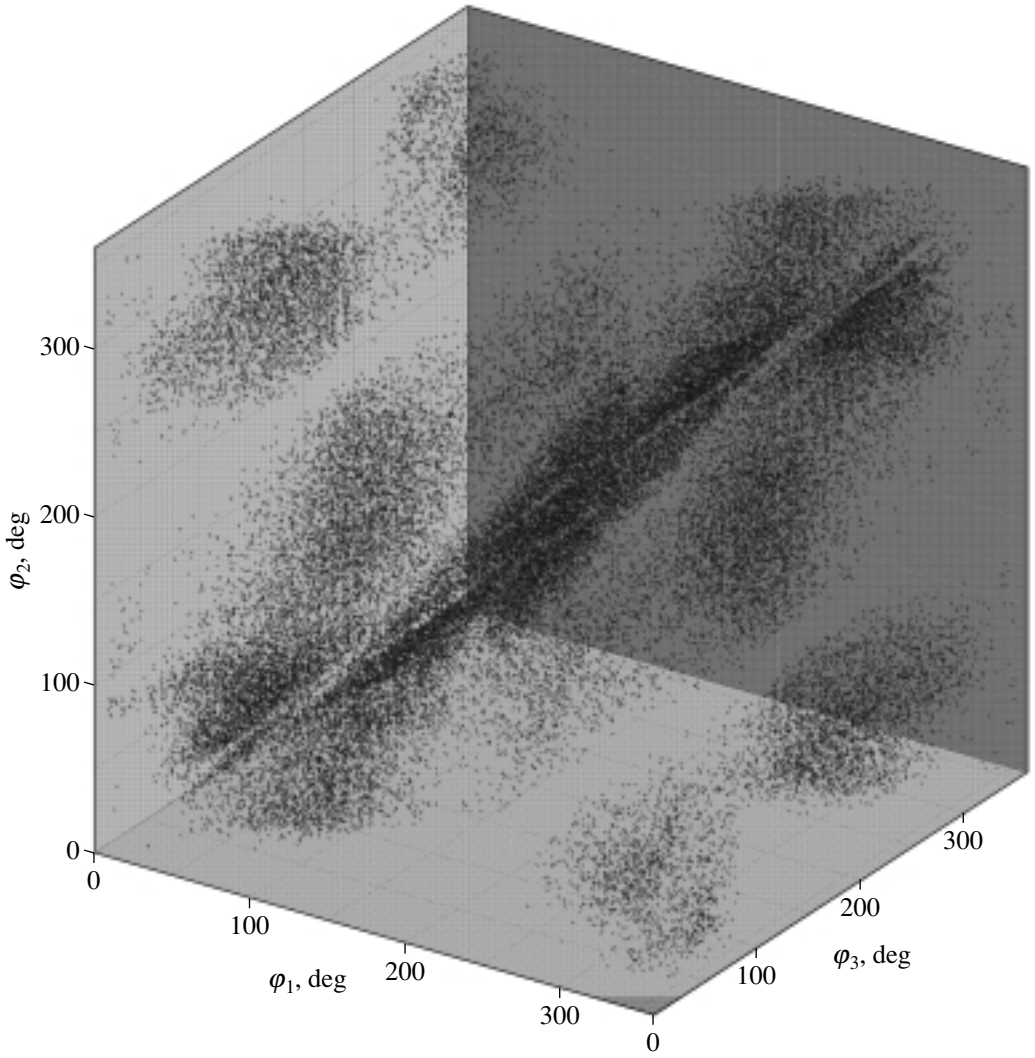

Fig. 4. Three-dimensional distribution of points in $(\varphi_1, \varphi_2, \varphi_3)$ space at $\delta \in [0, 0.29]$.

RESULTS AND DISCUSSION

The initial conditions for nearly periodic trajectories with $\min \Phi < 0.1$ can be represented on sections of four-dimensional $(\delta, \varphi_1, \varphi_2, \varphi_3)$ parameter space.

Figure 2 shows the (δ, φ_i) sections at $i = 1, 2, 3$. All figures are symmetric relative to the $\varphi_i = 180°$ straight lines. There are concentrations of points near $\varphi_i = 90°$ and $\varphi_i = 270°$. These sets are elongated along the δ axis and become denser as $\delta \to 1/3$. Small clusters near the points $(\delta, \varphi_i) = (0.075, 180°)$ are also observed in the (δ, φ_1) and (δ, φ_3) diagrams. Variously shaped zones of reduced concentration of points are observed along with their clusters. The boundaries of these zones can be both sharp and blurred.

Figure 3 shows the (φ_i, φ_j) sections at $i < j$. These distributions of points are symmetric relative to the bisectors $\varphi_i = \varphi_j$ rotated through 180°. There are no points on the bisector itself, because we do not consider equal angles, $\varphi_i = \varphi_j$. Note that the sets of points are roughly mirror-symmetric relative to the $\varphi_i = \varphi_j$ diagonal and the $\varphi_i = 360° - \varphi_j$ diagonal orthogonal to it. The (φ_1, φ_3) diagram contains three compact sets near the points $\varphi_1 = \varphi_3 = 0° = 180° = 360°$ (these do not show up on the other two sections). These sets correspond to small δ. Weak, elongated clusters of points along the $\varphi_1 = 180°$ and $\varphi_3 = 180°$ straight lines are seen in Figs. 3a and 3c. At small fixed δ, the clusters of points are isolated in the three-dimensional space of angles $(\varphi_1, \varphi_2, \varphi_3)$. The total three-dimensional section for $\delta \in [0, 0.29]$ shown in Fig. 4 illustrates this result. These clusters join as δ increases.

Consider the main types of nearly periodic orbits that we found by the scanning method described above. We chose only the orbits with relatively short periods $P < 10\tau$. These were separated into several

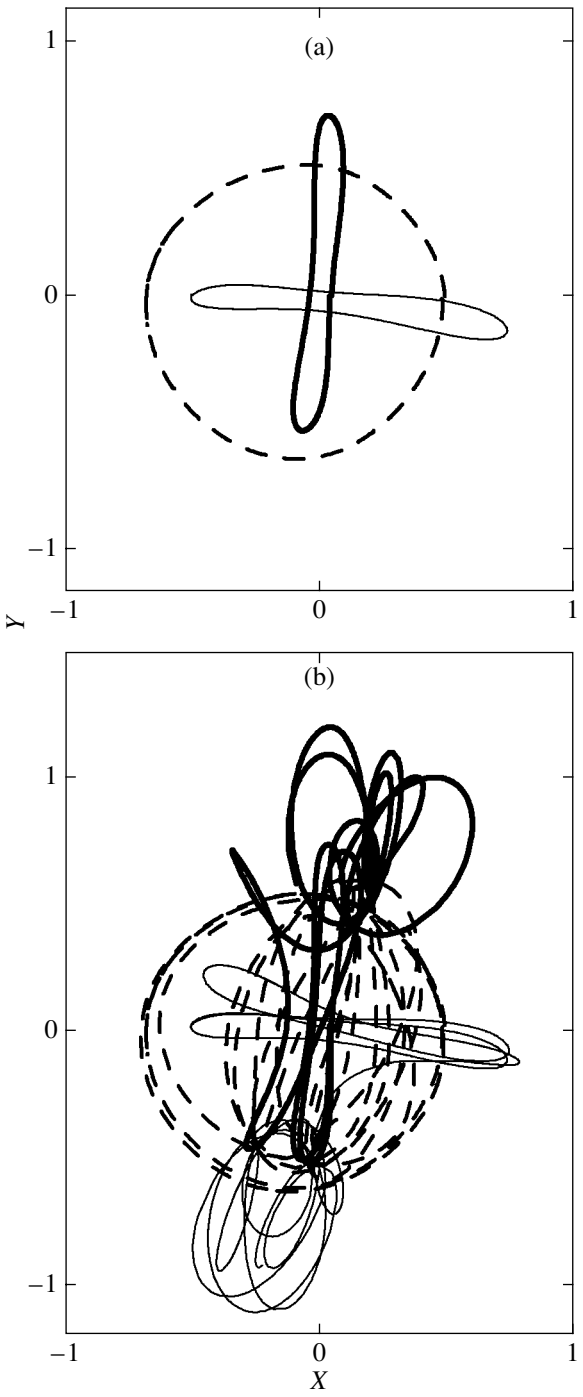

Fig. 5. (a) Ducati-type orbit with the initial conditions $\delta = 0.031$, $(\varphi_1, \varphi_2, \varphi_3) = (51^\circ, 286^\circ, 81^\circ)$; (b) evolution of the orbit during $t = 10\tau$.

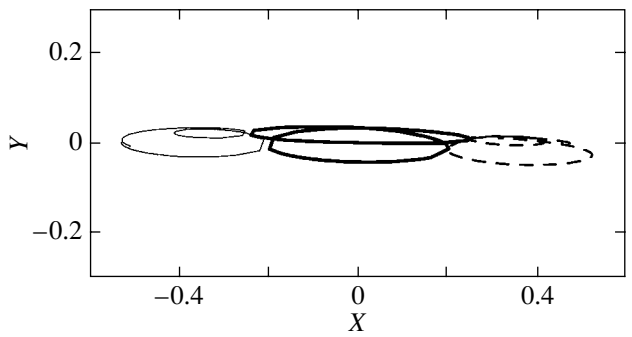

Fig. 6. Chainlike orbit with the initial conditions $\delta = 0.055$, $(\varphi_1, \varphi_2, \varphi_3) = (174^\circ, 159^\circ, 169^\circ)$.

families according to P. The shortest period for the orbits under consideration is $P \approx 1.3\tau$. A total of 26 families were identified. Some of the families are isolated, while others are joined in periods. The separations between the periods of neighboring families are different at $P < 3.5\tau$ and approximately equal, $\sim 0.3\tau$, at longer periods. The width of each family is also $\sim 0.3\tau$.

The table lists the main parameters of the identified families of nearly periodic orbits at $\delta \leq 0.23$. The following data are given in the table: the family number; the mean period of a given family $\bar{P}$ in units of the mean crossing time τ (9); the number of trajectories in the family with the periods that differ from the mean $\bar{P}$ by no more than 0.15τ; the values of (δ, φ_1, φ_2, φ_3) for individual trajectories—representatives of various types of orbits within a given family; the period P (in units of τ); the minima of the functional Φ (8) and the Lagrangian L for these orbits; and a brief description of the structure of trajectory loops. The Lagrangian

$$L = T - U, \tag{10}$$

where T and U are the kinetic and potential energies of the triple system, respectively, was calculated at the time the functional Φ reached its deepest minimum.

Basically, three types of structure can be identified: leafed, looplike, and chainlike. The leafed structures correspond to retrograde motions, where the inner and outer binaries rotate in the opposite directions. The looplike structures correspond to prograde motions, where these binaries rotate in the same direction. The chainlike trajectories are generated by a stable periodic orbit found by von Schubart (1956) in the rectilinear three-body problem. In these triple systems, one of the bodies (central body) undergoes successive encounters with each of the extreme bodies without any encounter between the latter.

In addition to the main types of structures, we observe certain peculiar orbits marked by asterisks in the first column of the table. The Lagrangian L of these systems is small compared to other systems from the same family with the same period $\bar{P}$. The peculiarities of these orbits will be discussed below.

The number of loops and leaves increases with period. Systems with different numbers of loops or leaves are observed for some of the families at the

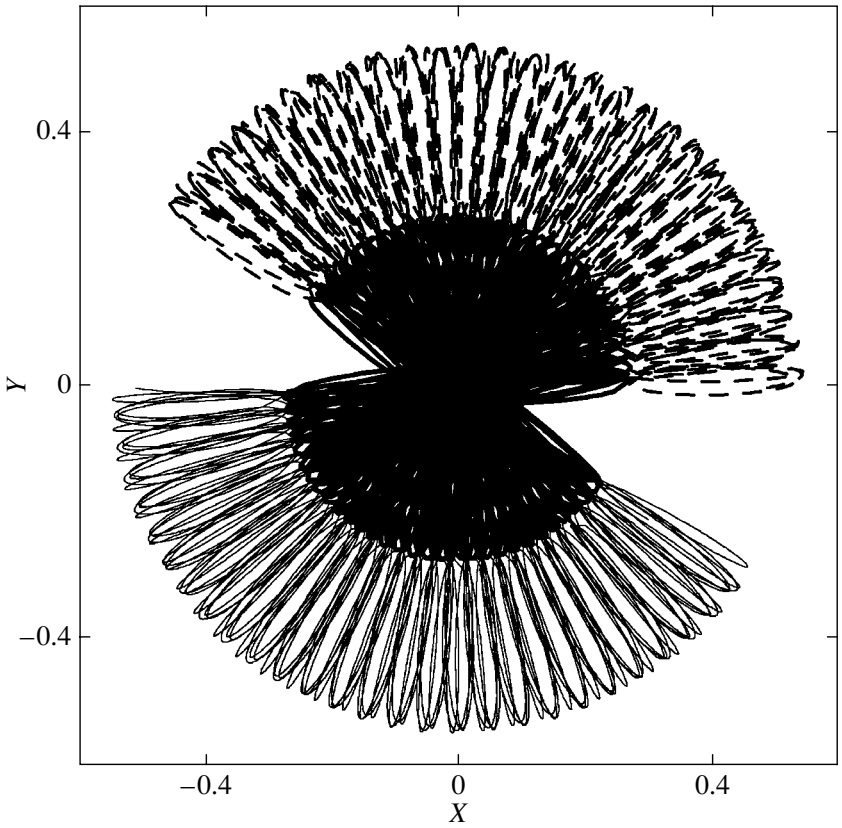

Fig. 7. Precession of a chainlike orbit during about 100 periods. The initial conditions are $\delta = 0.020$; $(\varphi_1, \varphi_2, \varphi_3) = (5^\circ, 45^\circ, 10^\circ)$.

same period. In general, within the same family of nearly periodic orbits, the Lagrangian L increases with increasing parameter δ (i.e., hierarchy of the system's initial configuration) at the time the functional Φ reaches its minimum. Note also that the situation where two of the three values $\varphi_i (i = 1, 2, 3)$ are close, while the third value differs significantly from these, is typical. At short periods, the number of orbits n with $\Phi < 0.1$ is relatively small. At $\bar{P} = 3.6$, the number n reaches its maximum probably through an increase in the number of chainlike orbits generated by von Schubart's orbit. As the period $\bar{P}$ increases further, n does not change greatly.

Let us consider examples of nearly periodic orbits. Figure 5a shows a ducati-type orbit (see, e.g., Moore 1993; Vanderbei 2003). The trajectories of the bodies form a crosslike structure: one of the bodies moves along a nearly circular curve, while the other two bodies move along elongated, mutually orthogonal closed curves. As the orbit evolves further, it becomes chainlike (Fig. 5b) in a time $\approx (3-4)\tau$ (about 3 periods).

Figure 6 shows an example of a chainlike orbit. The central body oscillates between the extreme bodies. The orbits of the bodies become alternately elongated and circular. As the orbit evolves further, it begins to smear and precess. An example of a precessing chainlike orbit is shown in Fig. 7.

An example of an eight-leaf orbit is shown in Fig. 8a. As the computational time increases, the structure exhibits libration and precession (Fig. 8b). As a result, an original fan-shaped pattern is formed inside the ring formed by the trajectory loops of the third body. With the passage of time, this pattern becomes symmetric about the center of mass of the triple system.

An example of a looplike orbit is shown in Fig. 9a. The trajectory loops of each of the bodies without precession become thicker with time (Fig. 9b).

Let us consider the locations of our identified trajectories (see the table) in the region of initial conditions. For this purpose, we plot the initial values of the parameters (φ_1, φ_2, φ_3) for these trajectories in Fig. 3. The stars, circles, and crosses correspond to chainlike, leafed, and looplike orbits, respectively. The triangle marks a ducati-type trajectory. The clusters

Parameters of the families of nearly periodic orbits

N	$\bar{P}, \tau$	n	δ	φ_1, deg	φ_2, deg	φ_3, deg	P, τ	Φ	L	Notes
1*	1.3	1	0.031	51	286	81	1.32	0.049	8.38	Ducati
2	1.8	8	0.055	174	159	169	1.80	0.043	5.76	Chain
			0.030	272	78	285	1.76	0.051	8.24	6 leaves
3	2.2	7	0.096	93	247	106	2.14	0.059	7.76	8 leaves
4	2.5	28	0.087	275	81	285	2.53	0.034	8.37	10 leaves
5	2.9	27	0.025	201	97	86	2.90	0.067	6.51	10 loops
			0.156	228	115	208	2.89	0.070	7.96	$(5+1)+(4+2)$ leaves, hierarchy
			0.137	276	62	290	2.88	0.047	8.67	12 leaves
6	3.2	67	0.073	342	54	80	3.24	0.014	6.74	12 loops
			0.055	256	101	226	3.25	0.068	8.21	14 leaves
			0.166	115	265	123	3.23	0.088	8.61	16 leaves
7	3.6	516	0.057	335	87	91	3.60	0.040	6.50	14 loops
			0.075	181	82	176	3.62	0.017	6.66	Chain
			0.145	86	283	78	3.59	0.022	8.98	16 leaves
8	3.9	133	0.114	14	312	286	3.94	0.016	7.05	16 loops
			0.170	95	243	106	3.93	0.021	9.13	18 leaves
9	4.3	167	0.106	13	303	282	4.28	0.017	6.98	20 loops
			0.126	167	227	257	4.28	0.016	7.25	18 loops
			0.173	264	112	254	4.27	0.025	9.29	20 leaves
10	4.6	186	0.127	186	124	103	4.61	0.022	7.06	20 loops
			0.197	97	258	101	4.60	0.023	9.92	22 leaves
			0.204	270	266	115	4.60	0.025	10.18	18 loops
11	5.0	192	0.140	332	276	286	4.94	0.005	7.11	22 loops
			0.221	91	324	87	4.93	0.021	10.80	24 leaves
12	5.3	226	0.152	332	275	287	5.27	0.012	7.28	24 loops
			0.163	85	273	81	5.27	0.020	9.56	26 leaves
			0.226	90	93	220	5.26	0.027	11.11	22 loops
13	5.6	259	0.146	317	274	280	5.60	0.008	7.24	26 loops
			0.210	93	231	102	5.60	0.013	10.54	28 leaves
14	5.9	222	0.147	10	308	284	5.93	0.009	7.54	28 loops
			0.171	118	93	98	5.92	0.012	7.60	30 loops
			0.179	296	276	270	5.92	0.019	7.72	28 leaves
			0.197	273	103	270	5.92	0.012	10.36	30 leaves
15	6.3	224	0.166	338	277	291	6.25	0.008	7.41	30 loops
			0.220	261	125	253	6.24	0.015	11.02	32 leaves
16	6.6	245	0.165	49	86	80	6.57	0.016	7.59	32 loops
			0.200	266	64	273	6.57	0.014	10.49	34 leaves

Table. (Contd.)

N	$\bar{P},\tau$	n	δ	φ_1, deg	φ_2, deg	φ_3, deg	P,τ	Φ	L	Notes
17	6.9	222	0.210	10	71	46	6.89	0.011	9.02	34 loops
			0.201	96	306	86	6.89	0.019	10.54	36 leaves
			0.229	97	104	230	6.89	0.019	11.78	32 loops
18	7.2	209	0.178	323	285	275	7.21	0.011	7.89	36 loops
			0.191	90	101	243	7.21	0.015	10.28	34 loops
			0.220	109	259	108	7.21	0.025	11.62	38 leaves
19	7.5	230	0.183	317	274	283	7.53	0.013	8.03	38 loops
			0.199	215	248	261	7.53	0.012	8.48	38 leaves
			0.217	278	56	289	7.53	0.015	11.29	40 leaves
20	7.9	196	0.186	28	80	68	7.85	0.010	8.15	40 loops
			0.211	86	280	82	7.84	0.014	11.12	42 leaves
			0.229	84	75	311	7.84	0.015	11.76	38 loops
21	8.2	201	0.178	150	97	107	8.17	0.008	7.99	42 loops
			0.221	79	67	305	8.16	0.021	11.32	40 loops
			0.232	92	227	100	8.16	0.010	12.02	44 leaves
22	8.5	177	0.188	48	92	105	8.48	0.011	8.28	44 loops
			0.192	269	58	283	8.48	0.020	10.44	46 leaves
			0.223	89	84	291	8.48	0.015	11.66	42 loops
23	8.8	183	0.163	41	91	86	8.80	0.012	7.74	46 loops
			0.186	197	258	244	8.80	0.008	8.24	48 loops
			0.202	278	290	67	8.79	0.018	10.65	44 loops
			0.218	265	47	276	8.79	0.016	11.39	48 leaves
24*	9.1	189	0.001	326	276	346	9.01	0.039	6.08	Chain, three compressed figures eight
			0.225	126	105	95	9.11	0.012	9.58	50 leaves
			0.232	89	102	73	9.10	0.010	9.79	48 loops
25	9.4	168	0.213	162	205	244	9.42	0.010	9.75	52 loops
			0.184	259	119	237	9.42	0.019	10.02	52 leaves
			0.224	272	265	120	9.42	0.009	11.76	48 loops
26	9.8	169	0.007	336	216	316	9.92	0.076	6.71	Chain
			0.226	218	262	247	9.73	0.010	9.74	54 loops
			0.225	98	237	109	9.73	0.011	11.74	54 leaves

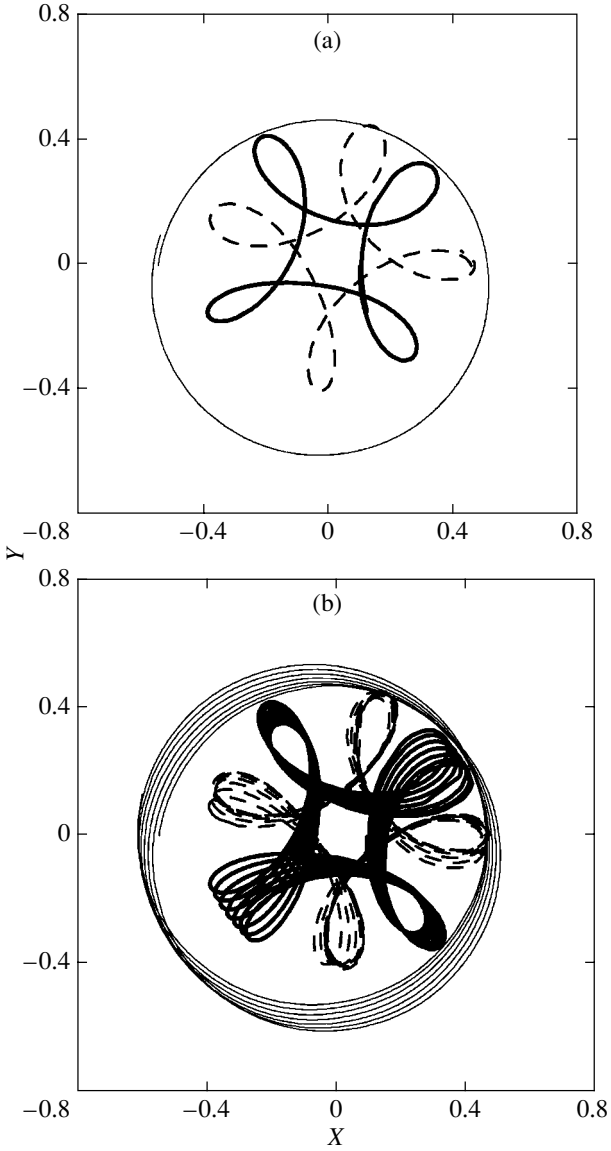

Fig. 8. (a) Eight-leaf orbit with the initial conditions $\delta = 0.096$; $(\varphi_1, \varphi_2, \varphi_3) = (93^\circ, 247^\circ, 106^\circ)$; (b) evolution of the orbit during $t = 15\tau$.

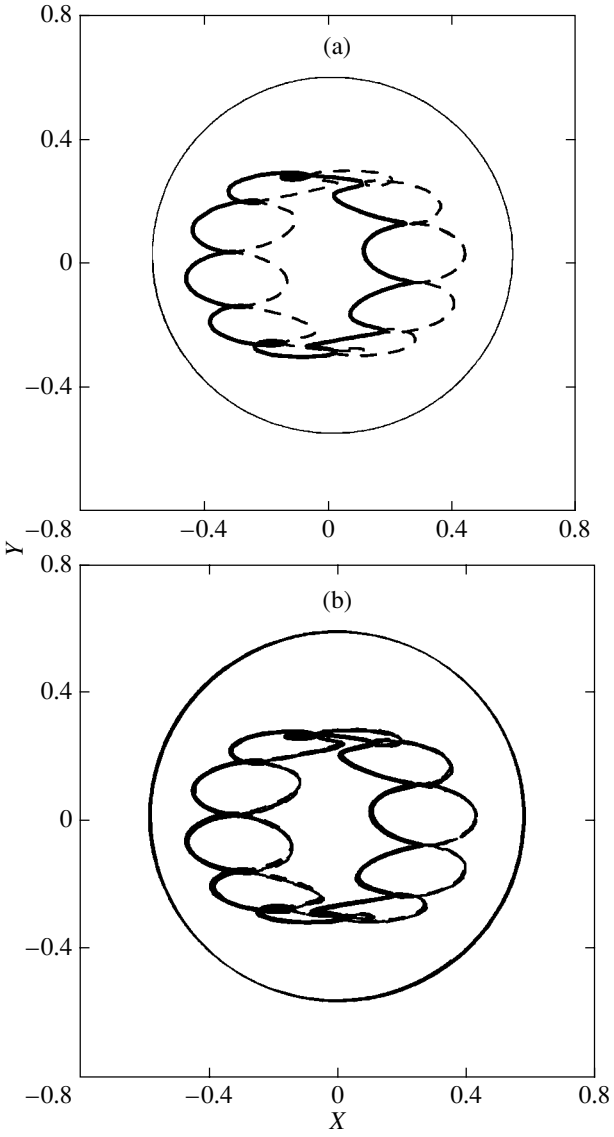

Fig. 9. (a) Looplike structure with the initial conditions $\delta = 0.127$; $(\varphi_1, \varphi_2, \varphi_3) = (186^\circ, 124^\circ, 103^\circ)$; (b) evolution of the orbit during $t = 20\tau$.

and filaments formed by these points are observed. These points concentrate toward the $\varphi_i = \varphi_j$, $\varphi_i + \varphi_j = 360^\circ$ $(i, j = 1, 2, 3; i \neq j)$ diagonals. In Figs. 3a and 3c, the groups of points corresponding to the initial conditions for orbits with looplike structures concentrate toward the $\varphi_1 = \varphi_2$ and $\varphi_2 = \varphi_3$ diagonals. For orbits with leafed structures, the points are located mostly near the $\varphi_1 + \varphi_2 = 360^\circ$ and $\varphi_2 + \varphi_3 = 360^\circ$ diagonals. In Fig. 3b, the points of initial conditions for both types of structures are located mostly near the $\varphi_1 = \varphi_3$ diagonal. Some of the initial conditions for von Schubart's chainlike orbits (and only these) are near the centers of the squares ($\varphi_i \approx 180^\circ$, $i = 1, 2, 3$).

The trajectories presented above (see the table and Figs. 5–9) were analyzed during one period. As the computational time increases, the periodic pattern is blurred by the precession and/or libration of orbits relative to the equilibrium orbit. Depending on how close the initial conditions are to the exact periodic solution and on the stability of this solution, the following changes in the pattern of motion can be observed: (1) thickening of the regions filled with the orbits of the bodies and the formation of ribbon structures (Fig. 10a); (2) libration of the trajectories of the bodies (Fig. 10b); and (3) precession of the orbits (Fig. 10c). By precession and libration we mean, respectively, the systematic rotation of the orbit around the center of mass of the triple system and

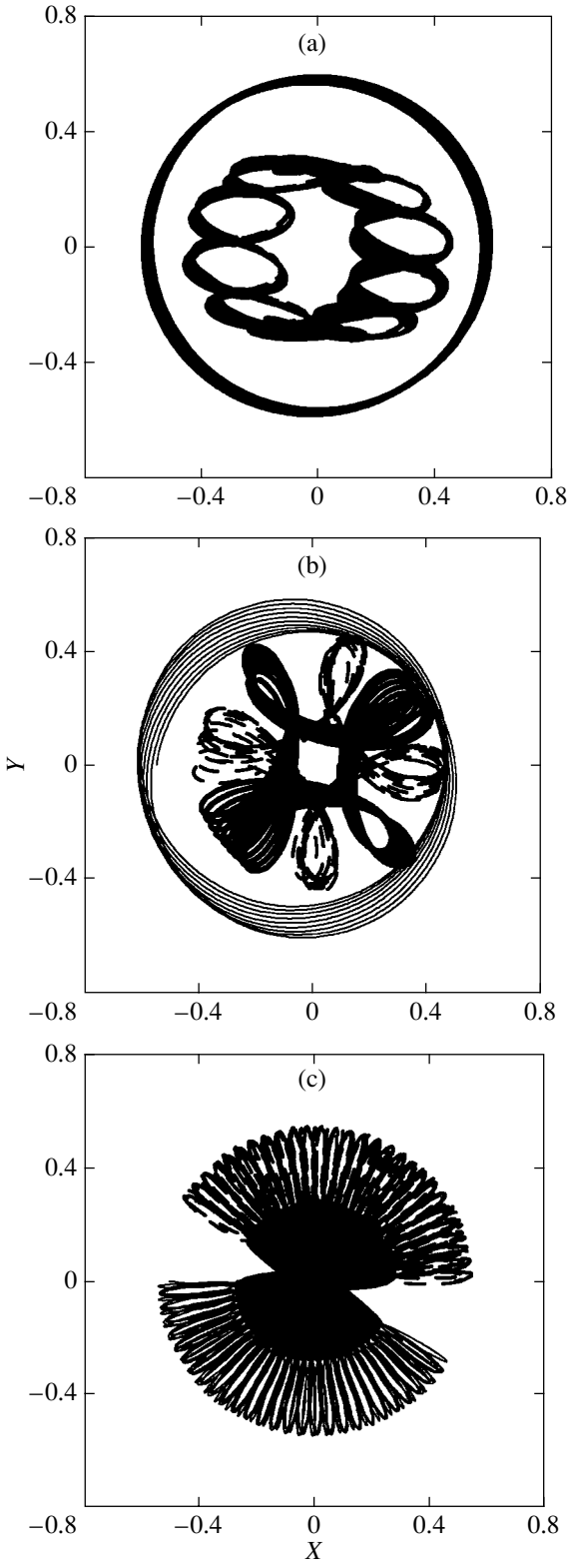

Fig. 10. Change in the pattern of motion with time: (a) ribbon structure (the initial conditions are $\delta = 0.127$; $(\varphi_1, \varphi_2, \varphi_3) = (186^\circ, 124^\circ, 103^\circ)$); (b) libration ($\delta = 0.096$; $(\varphi_1, \varphi_2, \varphi_3) = (93^\circ, 247^\circ, 106^\circ)$); (c) precession ($\delta = 0.020$; $(\varphi_1, \varphi_2, \varphi_3) = (5^\circ, 45^\circ, 10^\circ)$).

the oscillations of the trajectory loops within certain limits. A combination of these evolutionary scenarios (e.g., the combination of libration and precession) is possible. In those cases where the periodic orbit is unstable or the initial conditions are far from being periodic, the ejections of bodies begin after a certain time, and the evolution of the triple system eventually ends with its breakup, the escape of one of the bodies in a hyperbolic orbit.

Two types of symmetry are observed in the nearly periodic orbits we found: axial (Fig. 6) and central (Figs. 8 and 9). There are both nonhierarchical systems (Fig. 6) and hierarchical systems (in these systems, the center of mass of the close pair is displaced relative to the center of mass of the triple) among the trajectories with axial symmetry.

CONCLUSIONS

We analyzed the families of nearly periodic orbits in the general plane problem of three equal-mass bodies in a fixed coordinate system. We considered a four-dimensional section of the space of initial conditions at fixed total energy of the triple system, $E = -1$. We restricted our analysis to orbits with syzygies, where all three bodies are on one straight line at the initial time.

We identified three main types of nearly periodic orbits:

(1) Chainlike orbits generated by von Schubart's stable orbit (von Schubart 1956) (Fig. 6).

(2) Leafed orbits for the retrograde motions of the inner and outer binary subsystems (Fig. 8).

(3) Looplike orbits for the prograde motions of these binaries (Fig. 9).

In general, the leafed and looplike structures are inside the oval region that is bounded by the ring filled with the trajectory loops of the third distant body. The orbital period, the Lagrangian at the time the functional Φ (8) reaches its deepest minimum, the number of loops (leaves), and the complexity of the orbital structure, on average, increase with parameter δ, i.e., with the hierarchy of the initial configuration.

The following questions are of considerable interest:

(1) Studying the dependences of the functional Φ (8) on the initial conditions (δ; φ_1, φ_2, φ_3) as well as the period P on these parameters and the functional.

(2) Investigating the topology of orbits in velocity space.

(3) Analyzing the structures (including the clusters and filaments found) on various sections of the space of initial conditions as a function of the number of leaves and loops and as a function of the size and shape of chainlike orbits;

(4) Localizing the exact periodic orbits when the total energy of the triple system (the fifth parameter) is varied.

(5) Determining the stability or instability of the periodic orbits found depending on the geometry of the trajectory loops.

(6) Analyzing the various evolutionary scenarios (precession, libration, ribbon structure, etc.).

(7) Investigating the changes in the structure of orbits when going to three-dimensional physical space.

(8) Studying other types of periodic orbits, including those in rotating coordinate systems.

Note that the trajectory loops of the components of the inner pair can form the winding of a cylinder in the three-dimensional case. One may expect the orbits of the components of this binary in projection onto a certain plane when rotating the cylinder axis to be topologically identical to the trajectories obtained in the two-dimensional case.

In addition, other families of periodic orbits, including choreographies, can also manifest themselves when varying the total energy (see, e.g., Simo 2002).

Apart from the case of equal masses, considering nearly periodic orbits in triple systems with components of different masses, including those in the extreme cases where one or two masses approach zero, is also of interest. Such problems can be of great importance for both stellar dynamics and celestial mechanics.

ACKNOWLEDGMENTS

Orlov thanks the Foundation for Support of Leading Scientific Schools (project no. 1078.2003.02), the Russian Foundation for Basic Research (project no. 02-02-17516), and the *Universities of Russia* Program of the Federal Agency for Education of the Russian Federation (project no. UR.02.01.301) for support of this study. We are grateful to L.L. Sokolov and the referees for several valuable remarks.

REFERENCES

1. S. J. Aarseth and K. Zare, Celest. Mech. **10**, 185 (1974).
2. R. Broucke, Astron. Astrophys. **73**, 303 (1979).
3. R. Bulirsch and J. Stoer, Numer. Math. **8**, 1 (1966).
4. A. Chenciner and R. Montgomery, Ann. Math. **52**, 881 (2000).
5. C. Contopoulos, *Order and Chaos in Dynamical Astronomy* (Springer-Verlag, New York, 2002).
6. J. Hietarinta and S. Mikkola, Chaos **3**, 183 (1993).
7. A. J. Lichtenberg and M. A. Lieberman, *Regular and Stochastic Motion* (Springer-Verlag, New York, 1982; Mir, Moscow, 1984).
8. C. Moore, Phys. Rev. Lett. **70**, 3675 (1993).
9. V. V. Orlov, A. V. Petrova, A. V. Rubinov, and A. I. Martynova, Pis'ma Astron. Zh. **30**, 393 (2004) [Astron. Lett. **30**, 349 (2004)].
10. K. Simo, *Present-Day Problems of Chaos and Nonlinearity* (Inst. Komp. Islled., Izhevsk, 2002), p. 252 [in Russian].
11. R. J. Vanderbei, astro-ph/0303153 (2003).
12. J. von Schubart, Astron. Nachr. **283**, 17 (1956).

Translated by V. Astakhov